Design and Experimental Study of a Sabatier Reactor for Conversion of CO_2 and Biogas into Renewable Natural Gas

by

Yichen Zhuang

A thesis
presented to the University of Waterloo
in fulfillment of the
thesis requirement for the degree of
Doctor of Philosophy
in
Chemical Engineering

Waterloo, Ontario, Canada, 2022

Examining Committee Membership

The following served on the Examining Committee for this thesis. The decision of the Examining Committee is by majority vote.

External Examiner	Josephine Hill Professor
Supervisor(s)	David Simakov Associate Professor
Internal Member	Aiping Yu Professor
Internal Member	Eric Croiset Professor
Internal-external Member	Yuri Leonenko Associate Professor

Author's Declaration

I hereby declare that I am the sole author of this thesis. This is a true copy of the thesis, including any required final revisions, as accepted by my examiners.

I understand that my thesis may be made electronically available to the public.

Abstract

Biogas is a product of anaerobic fermentation which is rich in CO_2. Upgrade of biogas is commercially achieved by separating CO_2 and impurities to improve its quality. As an alternative, the CO_2 contained in biogas can be directly converted into CH_4 via the thermocatalytic Sabatier reaction without separation, using H_2 generated by water electrolysis (utilizing renewable or surplus, low carbon footprint electricity). One of the major elements of this technology is the configuration of the Sabatier reactor. For industrial applications, it is beneficial to eliminate the energy-intensive CO_2 separation step, converting biogas to RNG directly.

This study aimed to demonstrate the feasibility of converting CO_2 and anaerobic fermentation streams (such as biogas and landfill gas) into renewable natural gas (RNG) in an autonomous Sabatier reactor. The highly exothermic nature of the Sabatier reaction brings challenges to the design and operation of Sabatier reactors, especially the issues of thermal management. A completely autothermal operation of the N_2-cooled, stainless-steel reactor, using a Ni/Al_2O_3 catalyst has been demonstrated. The effects of feed temperature, space velocity and cooling rate were investigated using three prototypes with different sizes and configurations. The maximum CO_2 conversion of 93.5%, with 100% selectivity to CH_4 generation, was achieved in a 10″-length reactor, over 120 h of a continuous, stable operation with a pure CO_2 feed (at 2,400 L/(kg h), without any reactor heating or feed preheating. The same reactor also delivered 91% CO_2 conversion with 100% CH_4 selectivity using a synthetic biogas feed (without H_2S and VOCs) for 100 hours of stable operation. Experimental data, including outlet

concentrations and temperature distribution, were collected using an automated system and carefully analyzed. Kinetic parameters in a Sabatier-RWGS model were estimated and the final prototype reactor was modeled in COMSOL. A critical analysis of the collected data is presented, and future perspectives are discussed.

Acknowledgements

First and foremost, I want to thank my supervisor Professor David Simakov for providing me the opportunity to work on this research project and for his support, insight, guidance, as well as patience during my graduate studies. I've learned a lot from him in the past 6 years. My sincere thanks go to my committee members, Prof. Eric Croiset, Prof. Aiping Yu, and Prof. Yuri Leonenko, for their time, interest, and helpful comments. I would also like to thank Prof. Josephine Hill for kindly serving as my external committee member and for her suggestions and comments on this thesis.

This work would not have been possible without the help and advice from Robert Currie, Sogol Tabar, Guanjie Sun, Yue Yu, Muhammad Waqas Iqbal and Edris Madadian. I also received plenty of suggestions from department technical staff Bert Habicher.

Lastly, I would like to thank my families who have provided me with unwavering support and motivation throughout my studies. To my aunts Zhuang Li, Zhuang Min and my uncles, Qiu Zongqi and Zhang Minghui, who generously gave me helping hands when I was facing the sudden change in the family two years after I started my PhD.

I would also like to acknowledge the funding support from the Natural Science and Engineering Research Council (NSERC) of Canada through the Discovery Grant and Research Tools & Instruments program and from the Canada Foundation for Innovation (CFI) through the John R. Evans Leaders Fund (JELF) program.

Dedication

This thesis is dedicated to my mom and dad, Zhang Ruiqi and Zhuang Lintong, who always support and believe in me during my life, no matter how many mistakes I made.

Table of Contents

List of Figures

List of Tables

Nomenclature

C_i	molar concentration of species *i*, mol/m^3
C_p	heat capacity, J/(mol K)
D_{ae}	effective axial diffusion coefficient, m^2/s
D_{re}	effective radial diffusion coefficient, m^2/s
D_m	gas molecular diffusity, m^2/s
d_p	particle diameter, m
$E_{a,j}$	activation energy of reaction *j*, kJ/mol
f_1	CO_2 conversion to CO
f_2	CO_2 conversion to CH_4
$F_{c,out}$	total outlet molar flow rate of carbon-containing species, mol/min
$F_{H_2,f}$	feed molar flow rate of H_2, mol/min
$F_{CO_2,f}$	feed molar flow rate of CO_2, mol/min
$F_{CO,out}$	outlet molar flow rate of CO, mol/min
$F_{CH_4,out}$	outlet molar flow rate of CH_4, mol/min
$F_{t,out}$	total outlet molar flow rate, mol/min
ΔH_i	adsorption enthalpy of species *i*, kJ/mol
ΔH_{SR}	reaction enthalpy of Sabatier reaction, kJ/mol
h	heat transfer coefficient, J/(m^2 s K)
k_{ae}	effective axial thermal conductivity, J/(m s K)
k_{re}	effective radial thermal conductivity, J/(m s K)
k_{ins}	thermal conductivity of insulation layer, J/(m s K)

k_j	rate constant of reaction *j*
K_i	adsorption constant of species *i*
$K_{eq,j}$	equilibrium constant of reaction *j*
p_i	partial pressure of gaseous species *i*, bar
Q_f	volumetric feed flow rate, L/min
Q_c	coolant flow rate, L/min
r	reactor radius, m
R_j	rate of a reaction *j*, mol/(kg s)
R_g	gas constant, kJ/(mol K)
r_p	Particle radius, m
S_{CH_4}	CH_4 selectivity
t	time, s
T	reactor temperature, K
T_a	ambient temperature, °C
T_e	effluent temperature, °C
T_f	feed temperature, °C
T_{in}	reactor inlet temperature, °C
T_{out}	reactor outlet temperature, °C
T_c	coolant temperature, °C
T_w	reactor wall temperature, °C
U_w	overall heat transfer coefficient, J/(m^2 s K)
v	fluid velocity, m/s

V	reactor volume, m^3
X_{CO_2}	CO_2 conversion
y_i	mole fraction of species *i*
z	reactor length coordinate, m

Greek letters

α	H_2-to-CO_2 ratio
α_i	stoichiometric coefficient of species *i*
β	CH_4 content in the feed
γ	CH_4-to-CO_2 ratio
ε	catalyst bed porosity
τ_{bed}	tortuosity of the bed
λ	thermal conductivity, J/(m s K)
μ	viscosity, Pa s
ρ_g	gas molar density, mol/m^3
ρ_s	solid density, kg/m^3
$(\rho C_p)_{eff}$	effective heat capacity, $J/(m^3 K)$

Subscripts

eff	effective
f	feed
g	gas
HE	heat exchange

HL	heat loss
ins	insulation
s	solid
SR	Sabatier

Abbreviations

AC	activated carbon
BAL	balance
CB	carbon balance
CC	cocurrent flow
CNC	countercurrent flow
CCS	carbon capture and storage
CCU	carbon capture and utilization
GHSV	gas hourly space velocity, L/(kg h)
RNG	renewable natural gas
SYN	synthetic
VOC	volatile organic compound

Chapter 1
Introduction

1.1 Problem statement

Global warming has been having an increasing effect on the climate and everyday life. As Figure 1 shows, CO_2 and CH_4 contributed the majority of the total greenhouse gas (GHGs) emissions over the past five decades. According to Environment Canada, in 2019 Ontario contributed 163 Mt CO_2 equivalent GHG emissions. Among the 163 Mt GHG emissions, 85% are CO_2, 8% are CH_4, with 4% N_2O and 3% hydrofluorocarbons [1]. Since the industrial revolution, the extensive use of fossil fuels caused accelerating rates of CO_2 pollution. As atmospheric CO_2 levels have continued to climb in recent years, the need to significantly reduce anthropogenic CO_2 emissions has become more urgent [2]. CH_4 is another greenhouse gas 25 times more potent than CO_2 in terms of the global warming potential [3]. Anaerobic digestion products such as biogas and landfill gas contain 50-70% CH_4 and 25-45% CO_2, both being GHGs [4-6]. Both biogas and landfill gas are not of fossil origin, since they are produced via anaerobic fermentation process and do not have carbon added to the atmosphere. In 2015, around 56 billion cubic meters of biogas were produced globally [7], which are produced mainly from animal manure and slurries, agricultural waste, municipal waste and energy crops [8-10]. In 2019, the agriculture and waste treatment sector took ~11% of the total GHG emissions in Ontario, and a large portion of emissions from these sectors are in the form of biogas, Figure 2.

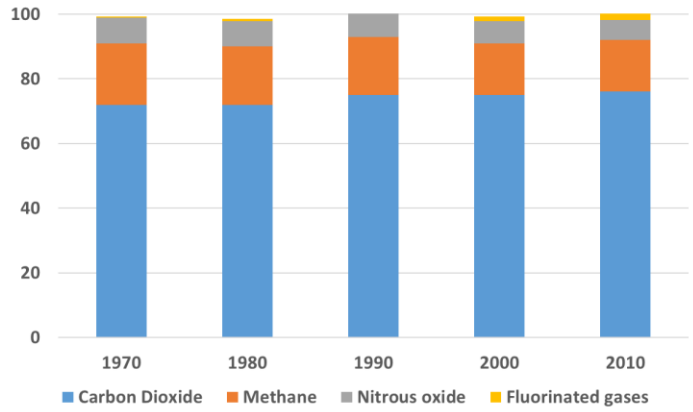

Figure 1. Global greenhouse gas emission by gas [11].

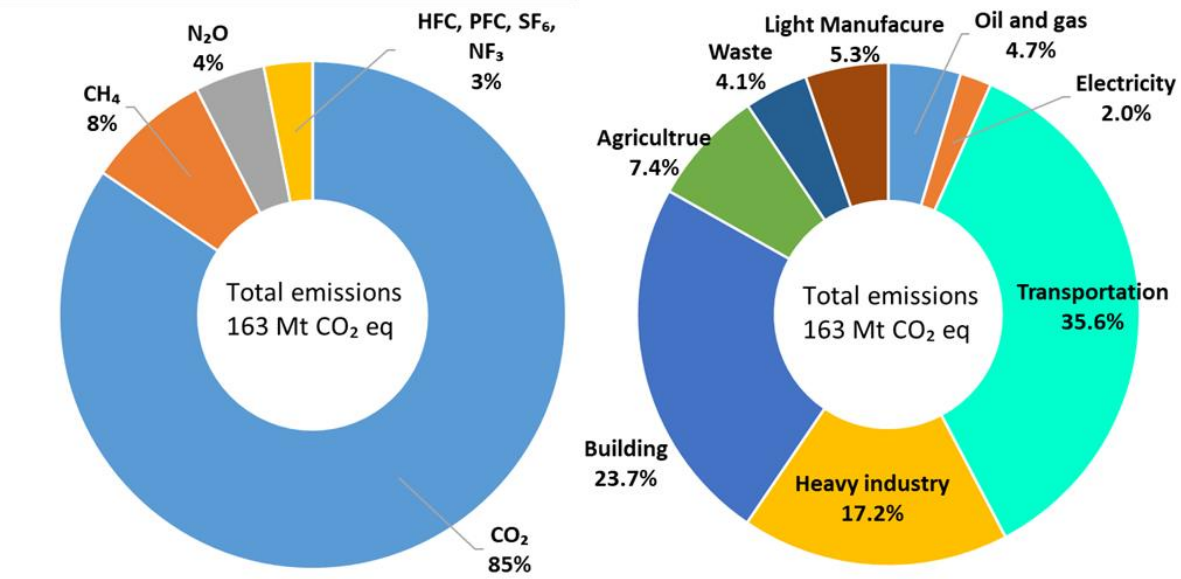

Figure 2. GHG emission composition and sources in Ontario (2019) [1].

Despite having relatively low calorific value, biogas is a versatile renewable energy source because of the variety of digestion processes and ease of storage [12, 13]. Raw biogas is commonly used directly for cooking, heating and lighting via combustion [14]. After cleaning and separation, biogas can also be used in internal combustion engines, turbines and fuel cells

[15]. Currently in Canada biogas is mostly used for electricity generation, which is about half of the biogas being utilized. The rest of the biogas is used for heating and upgraded into RNG [16]. A surprising 41% of biogas was flared since there was no use for those gases and raw biogas contains impurities like H_2S. RNG upgrade of biogas is commercially achieved via separation through amine scrubbing, pressure swing adsorption and membrane separation. However due to the high capital and operating cost of such upgrade units the viability of industrial scale biogas utilization is often limited. Biogas can also be upgraded into biofuels and chemicals via biological or chemical processes while this approach still faces several technological challenges.

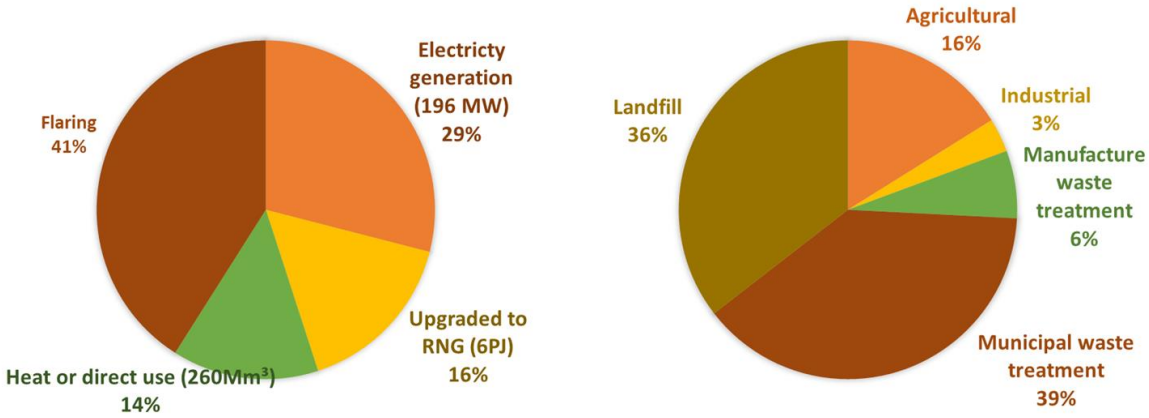

Figure 3. Biogas end use and producers in Canada (2020) [16].

Roughly 40% of total CO_2 emissions are from fossil fuel power plants and coal power plant is the main contributor [17]. The CO_2 content in the flue gas can be removed via pre-combustion, post-combustion and oxyfuel combustion capture [18]. Captured CO_2 is compressed and sent to storage, and can later be used for enhanced oil recovery [19].

Alternatively, CO_2 sequestration could be followed by CO_2 conversion into synthetic fuels and chemicals. Converting CO_2 into useful chemicals is of particular interest as this approach allows for CO_2 recycling and the introduction of renewable energy into the chemical industry production chain [20-22]. There are several optional pathways to synthesize fuels and chemicals using CO_2 as a carbon source, including photo and electro-chemical reduction, biological conversion, and thermocatalytic hydrogenation [23]. The implementation of the photo and electro-chemical CO_2 reduction routes has significant potential but is limited by the low CO_2 solubility in water and transport limitations [23-25]. The cost of cultivating and maintaining biomass growth systems remains a prohibiting factor for the implementation of large-scale biofuel production [23].

As an alternative to the abovementioned options, the thermocatalytic conversion of CO_2 can be seen as a viable option due to its technical feasibility, considering its similarity to some well-established industrial processes [23, 26]. The reaction pathways of producing synthetic fuels and chemicals from carbon dioxide are shown in Figure 4. The source of hydrogen can be versatile and cheaper sources can help reduce the overall production cost from CO_2 hydrogenation. Gasification of biomass and coal, or water electrolysis powered by renewable electricity are suitable hydrogen sources. The total electricity generation in Ontario in 2020 is 151 TWh, and ~33% are from renewable sources which could be potentially utilized, Figure 5. From the thermocatalytic conversion of CO_2 with hydrogenation, syngas can be obtained via either RWGS reaction or methane dry reforming (MDR). Syngas can also be produced with CH_4 and water via methane steam reforming (MSR). Syngas is a useful chemical feedstock that can be further converted into chemicals and fuels like methanol and higher hydrocarbons

via the Fischer-Tropsch process, providing flexibility in types of product and high efficiency [27, 28]. Another important pathway of CO_2 and H_2 is generating Renewable Natural Gas (RNG) via Sabatier reaction, and the RNG has the potential to substitute a portion of existing natural gas consumption. Converting CO_2 into CH_4 has also been shown to be the easier pathway for CO_2 valorization from a thermodynamic perspective [29] and has better energy storage capacity when compared to methanol-based processes [30]. However both reactor design and catalyst selection for such pathway still faces significant technological challenges.

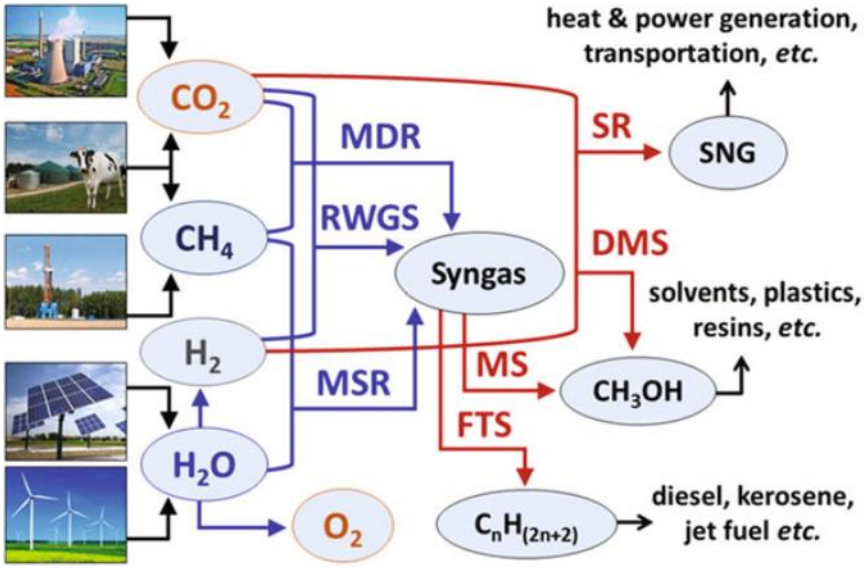

Figure 4. Reaction pathways of producing synthetic fuels and chemicals from CO_2 [23].

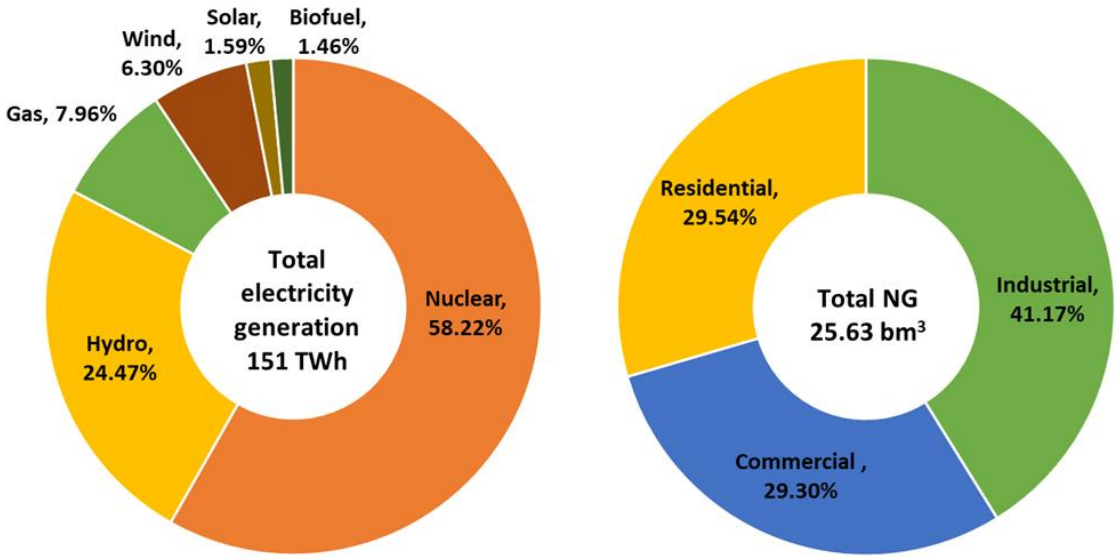

Figure 5. Electricity generation and natural gas consumption in Ontario (2020) [31].

1.2 Project objective

Main Goal

The main goal of this project is to build a proof-of-concept lab-scale standalone Sabatier reactor that can be used for both CO_2 methanation and direct biogas upgrade, as well as investigating the effect of operating parameters, such as space velocity and coolant flow rate over the reactor performance.

The specific research objectives are:

1. Investigate the catalytic performance of the selected catalyst using both pure CO_2 feed and biogas.

2. Construct the first packed bed tubular reactor with a small catalytic bed without active cooling using a furnace for preheating. Conduct experiments on both pure CO_2 feed and synthetic biogas feed and examine the reactor performance.
3. Construct a second reactor with increased dimensions as well as a cooling tube inside the reactor for heat removal. Conduct performance tests on both pure CO_2 feed and synthetic biogas and verify the possibility of standalone operation.
4. Scale up the reactor and add an individual heating element to the reactor to construct the proof-of-concept Sabatier reactor. Investigate the effect of operating conditions on reactor performance. Verify the possibility of standalone operation and long-term stability.
5. Find a suitable kinetic model of the Sabatier-RWGS reaction system from the literature and estimate model parameters based upon experimental data.
6. Model the proof-of-concept Sabatier reactor (Reactor 3) in COMSOL.

1.3 Thesis layout

This thesis consists of two research papers with similar structures and some additional modeling work. The first manuscript studied the operating parameters and catalytic performance of three prototype reactors with different sizes and configurations using pure CO_2 as a feedstock, as well as investigating the possibility of the autothermic operation of a Sabatier reactor. The second manuscript focused on the viability of direct biogas upgrade using Sabatier reactors and replaced the pure CO_2 feed with synthetic biogas in the three prototype reactors. Effects of operating conditions and long-term stability with such feed were also investigated.

Chapter 2 briefly review previous literature on CO_2 methanation and direct biogas upgrade through Sabatier reactor, including commercial and developing processing technologies, catalysts and reactor designs. Chapter 3 presents the experimental methodology and results on three prototype Sabatier reactors with pure CO_2 feed. As mentioned above this chapter is based on results from the first manuscript. Chapter 4 presents the experimental methodology and results of direct biogas upgrade with the same reactors. This chapter is based on results from the second manuscript. Chapter 5 shows a kinetic model of the Sabatier-RWGS reaction system and a COMSOL model based on one of the prototypes, and also presents simulation results and compared them to experimental data. Chapter 6 includes a summary of the results, conclusions, recommendations, and future work of this research.

Chapter 2
Literature review

As atmospheric CO_2 levels continue to climb, the need to significantly reduce anthropogenic CO_2 emissions becomes more urgent [2]. Among alternative solutions are CO_2 sequestration by carbon capture and storage (CCS) and carbon capture and utilization (CCU) via CO_2 conversion into synthetic fuels and chemicals via electrocatalytic, thermocatalytic, photocatalytic and biological pathways [23]. Producing synthetic fuels by CO_2 hydrogenation is of particular interest as this approach allows for CO_2 recycling while introducing renewable energy into the industry (via renewable H_2 generation) [20-22]. While comparing different pathways, photocatalytic conversion and electrocatalytic reduction have significant potential but are limited by the low CO_2 solubility in water and transport limitations [24, 25]. For biological CO_2 conversion, large-scale implementation for synthetic fuels production remains unlikely due to the significant cost of cultivating and maintaining biomass growth systems [23].

Thermocatalytic conversion of CO_2 offers the benefits of fast reaction rates and high conversion efficiencies allowing for compact, high throughput operation [23]. Producing synthetic CH_4 via the thermocatalytic conversion of CO_2 involves the Sabatier reaction, Eq (1), which is accompanied by reverse water gas shift (RWGS) and CO methanation, Eqs (2, 3). When using renewable (or low-carbon footprint) electricity to generate H_2 via water electrolysis, the resulting synthetic CH_4 can be considered as renewable natural gas (RNG).

$$CO_2 + 4H_2 \rightleftarrows CH_4 + 2H_2O \qquad \Delta H^{\circ}_{298} = -164.9\ \text{kJ/mol} \tag{1}$$

$$CO_2 + H_2 \rightleftarrows CO + H_2O \qquad \Delta H^{\circ}_{298} = +41.2\ \text{kJ/mol} \qquad (2)$$

$$CO + 3H_2 \rightleftarrows CH_4 + H_2O \qquad \Delta H^{\circ}_{298} = -206.1\ \text{kJ/mol} \qquad (3)$$

Sabatier reaction, as known as CO_2 methanation reaction, is a highly exothermic reaction. For 1 m^3/h CH_4 production rate (STP), 1.8 and 2.3 kWh heat can be released from CO_2 and CO methanation respectively [32]. As shown in Figure 6, the thermodynamic equilibrium of CO_2 methanation favors high pressure and low temperature, while it is hard for these exothermic reactions to reach equilibrium conversions at low temperature [33]. Running under high temperatures could cause sintering of the catalyst, which further leads to the loss of structural strength and catalyst deactivation [34]. High CO concentration can cause the formation of carbonyl and gum, which will also result in catalyst deactivation [34].

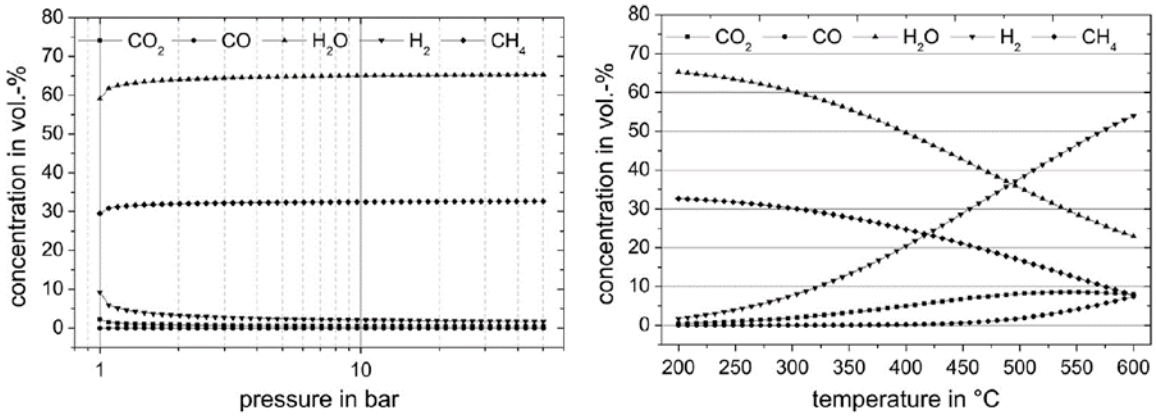

Figure 6. Equilibrium concentration of CO_2 methanation as a function of pressure (at temperature=300 °C) and temperature (at pressure =1 bar). Feed composition H_2:CO_2=4 [32].

Biogas, though being commonly used in heat and power generation, is also a common CO_2-rich mixture. The utilization of biogas from anaerobic fermentation as a substitute feedstock to fossil natural gas (NG) also has the potential to reduce CO_2 emissions significantly [23]. Such substitute natural gas obtained from non-fossil feedstocks is typically referred to as renewable natural gas (RNG) [23]. The emitted CO_2 as a result of the utilization of RNG combustion is of biological origin thus does not add carbon to the atmosphere. Biogas typically consists of 50-70% CH_4 and 25-45% CO_2, with some impurities including N_2, O_2 and H_2O, as well as a trace amount of hydrogen sulfide (H_2S), dust particles and volatile organic compounds (VOCs) including siloxanes and halogenated compounds [4, 5]. The production of the biogas is affected by the biodegradable organic matter content in the raw material, carbon to nitrogen ratio of the raw feed stock as well as temperature and pH of the anaerobic digester [35].

Despite the huge potential of biogas, its utilization as an alternative feedstock still has several technological challenges [36-38]. The existence of a significant portion of non-combustible CO_2 and N_2 drastically decreases the energy density, making it only suitable for applications like steam boilers that don't require high-grade fuel with large calorific value [39, 40]. For example, biogas with 60% CH_4 content and natural gas has a calorific value of 23 MJ/m^3 and 39 MJ/m^3 respectively [41]. During the compression of biogas for storage and transportation, CO_2 may form dry ice under high pressure, resulting in clogging issues of valves and small tubes [42]. Also, biogas contains trace amounts of contaminants and VOCs with some of them being hazardous to the environment and processing equipment.

Commercially available biogas upgrade technologies utilize adsorption, absorption, cryogenic and membrane separation to upgrade biogas to high-quality biomethane based on physical or chemical separation of CO_2 followed by removal of additional impurities including water vapor, H_2S and siloxanes [43]. Depending on the composition of the biogas, a significant portion of N_2 and O_2 can be removed via pressure swing adsorption (PSA) on molecular sieves or membrane separation [44-46]. Despite the decent performance, high operation costs and large capital investment associated with the abovementioned technologies limit the economic viability of biogas utilization on an industrial scale. New upgrade technologies such as biological methods are still under development. One of the biggest challenges of biological methanation is that it's hard for the water and gas phase to have sufficient contact due to the low solubility of hydrogen in water [47].

An alternative way is direct methanation of biogas, which involves the thermocatalytic conversion of CO_2. Producing synthetic CH_4 via the thermocatalytic conversion of CO_2 involves the Sabatier reaction, Eq. 1, which is accompanied by reverse water gas shift (RWGS) and CO methanation, Eqs. (2, 3). When using renewable (or low-carbon footprint) electricity to generate H_2 via water electrolysis, the resulting synthetic CH_4 can be considered as renewable natural gas (RNG). Thermocatalytic conversion of CO_2 offers the benefits of fast reaction rates and high conversion efficiencies allowing for compact, high throughput operation [23]. Also, direct CO_2 methanation via the Sabatier reaction can eliminate the huge capital and operating cost of CO_2 separation.

The process of biogas direct upgrading is conceptually shown in Figure 7. H_2 required for CO_2 methanation can be obtained from water electrolysis powered by renewable or (low

carbon footprint) surplus electricity since the electrolysis consumes most of the electricity among all processes [48]. Several different gas cleanings solutions have been suggested and tested in recent years, such as adsorption on activated carbon and other solid sorbents under ambient temperature to remove impurities such as H_2S, VOCs and siloxanes [48]. After the cleaning step, pretreated biogas is fed to the Sabatier reactor, e.g., packed bed [49, 50]. A pipeline grade RNG is obtained from the reactor outlet after water condensation and further product upgrading (removal of N_2 and unreacted CO_2 and H_2) if required. Electrolysis, as well as all cleaning, condensation and upgrading stages, are commercially available and the economic viability of the concept presented in Figure 7 was recently assessed [51]. However, reactor design and catalyst still present significant technological challenges [49, 50], mainly due to the significant heat of reaction from the reactor, which leads to sintering of catalyst as well as conversion limitation due to the thermodynamic equilibrium [48].

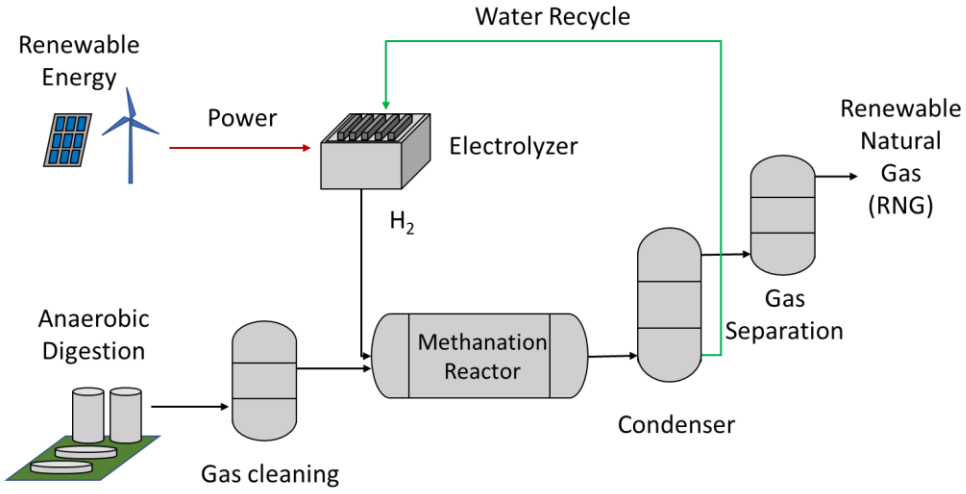

Figure 7. A conceptual diagram of the direct upgrade of biogas or landfill gas into renewable natural gas (RNG).

Over the years, many catalytic formulations have been suggested for CO_2 methanation, including supported noble metals and Ni-based formulations. Though Ni is not the most active metal for methanation, its performance is reasonably sufficient given its low cost [52], e.g., CO_2 conversion of 81% and CH_4 selectivity of 96% were reported for 20 wt% Ni/Al_2O_3 catalyst at 400°C and 55,000 h^{-1} [26]. It has been found that the addition of Yb_2O_3 can significantly improve the Ni dispersion of Ni/Al_2O_3 catalyst thus improving catalyst stability, which is one of the major concerns for Ni-based catalysts [53]. Another disadvantage of Ni-based catalysts is significant CO formation at higher temperatures. CO was confirmed as a reaction intermediate for Ni-catalyzed methanation reactions [54]. Noble metals such as Ru, Ir, Rh, Os, Pt and Pd generally have high catalytic activity and excellent resistance against coking [55]. Ru is known as a good CO_2 methanation catalyst. Pre-reduced 3 wt% Ru/Al_2O_3 catalyst was reported to have 93% CO_2 conversion and 100% selectivity to CH_4 at 325 °C [26]. The main disadvantage in the use of platinum group metals as catalysts is apparently their high cost. A recent study showed that under optimal conditions, a commercial Ni catalyst has catalytic performance similar to that of Ru (e.g., 91% CO_2 conversion with 100% CH_4 selectivity) also showing excellent stability [51].

With respect to the Sabatier reactor design, excess heat removal poses a significant challenge due to the highly exothermic nature of the Sabatier reaction. Subsequent reactor overheating will cause catalyst deactivation by coking and sintering [49, 56] and eventually lead to serious safety risks. Optimal reactor designs are required to mitigate these challenges. Various reactor configurations, including fixed bed, fluidized bed and microreactors have been suggested for the Sabatier reaction. A fixed bed reactor with active cooling (heat exchanger

type reactor) is one of the most common designs, with the catalyst being packed within either the tube or the shell side. This design is relatively simple but requires proper thermal management and could potentially suffer from a high pressure drop [57].

Figure 8 shows a tubular packed bed reactor design of the Sabatier reactor. This design adopted a heat exchanger type packed bed reactor cooled by multiple internal cooling tubes. To maintain a relatively low reactor temperature, molten salt was used as the coolant for this Sabatier reactor design. Model results indicated that the heat removal is efficient thus CH_4 production could be maximized and catalyst deactivation could be further suppressed [49].

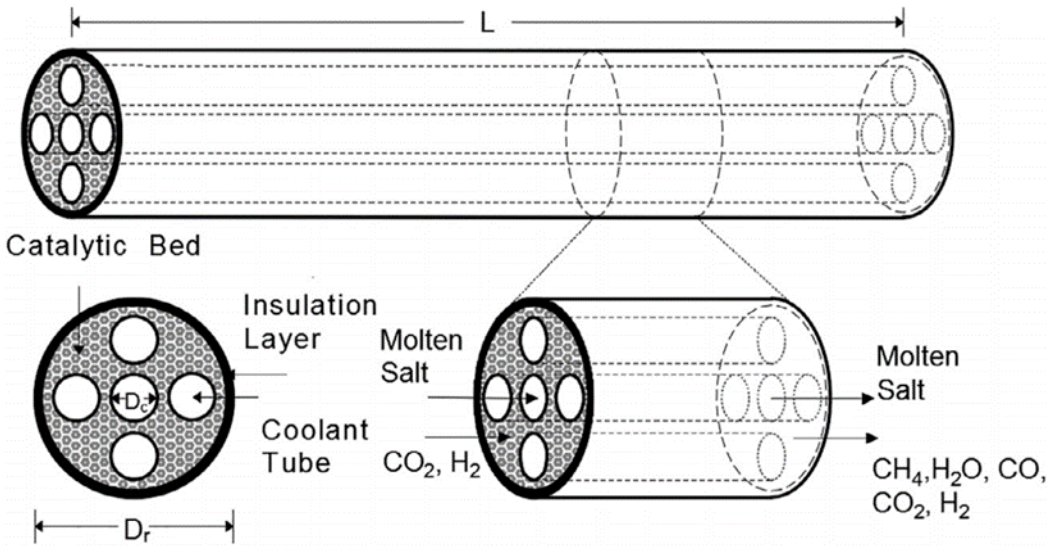

Figure 8. Sabatier reactor design with molten salt cooling [49].

One of the commercial power-to-gas projects, EU's Helmeth project (Integrated High-Temperature Electrolysis and Methanation for Effective Power to Gas Conversion) developed a methanation module that outputs 1-5 m^3/h RNG achieving 97% CH_4 and 2% H_2 in their final output composition. This module utilizes two reactors in series operating at 30 bars to produce

pipeline-quality RNG and operates at an isothermal condition for efficient heat removal, as shown in Figure 9. Boiling water is used as cooling medium and condensation stages are introduced between the reactors to maximize CH_4 yield by removing water production. [58]

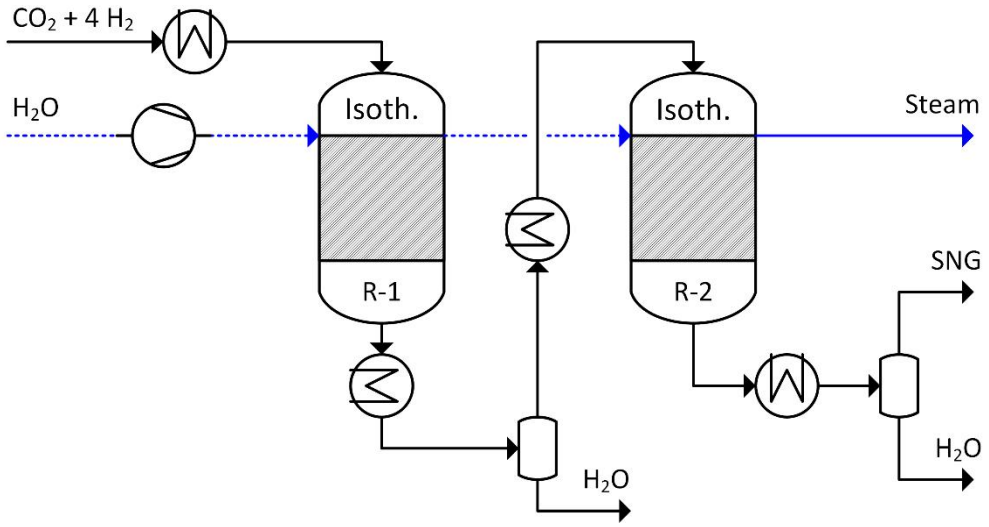

Figure 9. Schematic of methanation module with two reactors in series.

Another industrial-scale technology was developed by EtoGas, Figure 10. A 6.3 MW Power to gas plant was built in Germany. The plant consists of power electronics with rectifiers, water treatment system, hydrogen production (alkaline pressurized electrolysis), CO_2 feed gas treatment, methanation reactor, cooling system and ancillary systems. This methanation reactor also runs under isothermal conditions at around 350°C [59]. A CO_2 methanation system based on two actively cooled fixed bed reactors with interstage water condensation has been developed. The overall methanation efficiency was estimated at 75-80% and hot spots above 650°C were identified, probably due to the insufficient cooling [57].

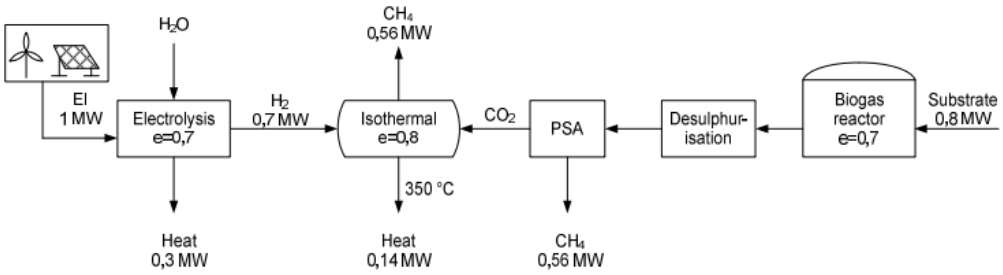

Figure 10. Process diagram of ETOGAS technology [60].

Several experimental reactor designs aimed to achieve isothermal reactor conditions have been suggested. These alternative configurations include a heat-exchanger type packed-bed reactor with cooling tube bundles [61], a structured microchannel reactor [62], and a honeycomb design [63]. While it is easier to design an isothermal methanation reactor, the finished reactor is more expensive due to the complicated deposition of the metallic structure and the difficulty of replacing the deactivated catalyst. This catalyst replacement is especially hard for microchannel or honeycomb reactors.

Another common design is an adiabatic fixed bed reactor. This design usually utilizes inter-stage cooling and gas recirculation to efficiently manage the reactor temperature. However, this approach requires multiple reactors with multiple heat exchangers, making the process integration quite difficult and resulting in high capital and operating costs [50, 64]. Commercial processes conventionally utilize this design, including systems from Air Liquide, Haldor Topsøe, and Johnson Matthey [64].

Fluidized beds generally offer excellent mass transfer efficiency and hydrodynamic characteristics [64], as shown in Figure 11 and Figure 12 [65-67]. Since 1952, the process design of fluidized bed reactors has been investigated and considered the superior methanation

reactor design. From 1975 to 1986 a pilot methanation plant was built by Thyssengas and the University of Karlsruhe [68]. In this pilot plant illustrated in Figure 12, a single fluidized-bed reactor was used, instead of using multiple adiabatic packed-bed reactors. Some studies found that fluidized bed reactors have less carbon deposition on the catalyst surface than in fixed bed reactors and also better tolerance for sulfur compounds in the feed [65, 69]. However, fluidized bed reactors suffer from attrition and entrainment of the catalyst due to high mechanical stress between the catalyst particles and the reactor wall [70, 71]. Another disadvantage is that fluidized beds can only be operated in a narrow range of operating conditions dictated by the fluidization velocity. Also, the capital cost for fluidized bed reactors is generally higher as compared to fixed bed designs [65].

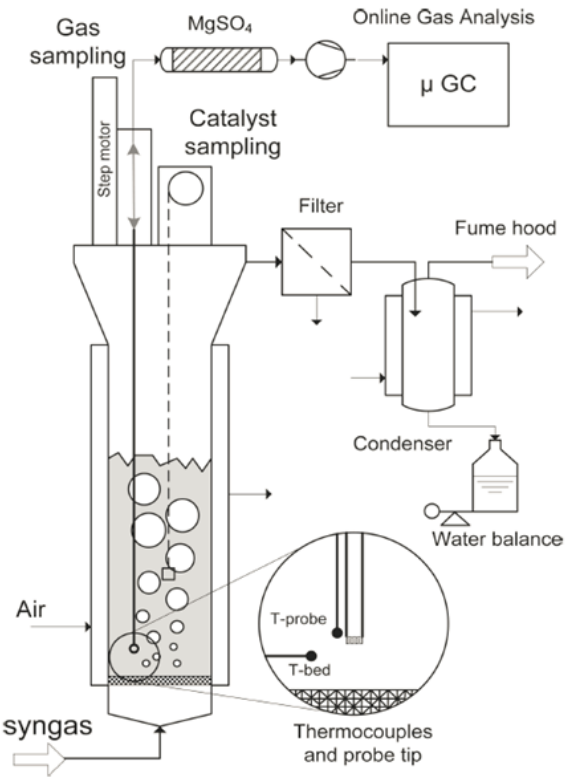

Figure 11. An experimental system comprising a fluidized-bed methanation reactor [65].

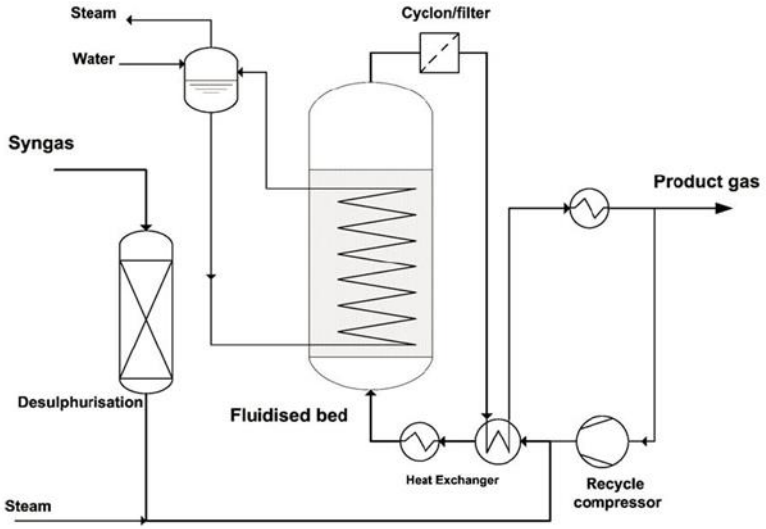

Figure 12. A flow diagram of the methanation process based on a fluidized bed reactor [66].

Microreactors, including microchannel- and microlith-based reactors, often have a smaller capacity but offer a compact design, excellent heat management and high efficiency. Typically, a supported catalyst (e.g., Ru, Rd) is coated on the surface of the microchannel wall or honeycomb microlith substrate [62, 72-74]. CO_2 conversion of 96% with 100% CH_4 selectivity was reported in a microlith Sabatier reactor at 360 °C under 1 atm, with a CO_2 utilization capacity calculated as 4 kg CO_2/day and stable operation for over 1,000 h [73]. Similar results (91% CO_2 conversion for over 900 h) were reported in a microchannel reactor [74]. In another study, 99% CO_2 conversion was reported at 300 °C using an oil-cooled microchannel reactor [62]. It was also indicated in this study that proper control of temperature distribution is a crucial factor for optimizing reactor performance. Junaedi et al. reported a 24 mL lightweight Microlith reactor achieved 88% CO_2 conversion with excellent stability [72]. This type of reactor design was suggested mostly for extraterrestrial explorations (Lunar and Martian missions) for air revitalization and propellant generation [72]. For large-scale applications, such as RNG generation, the compact design of such reactors imposes a limit on their production capacity. In addition, catalyst replacement is very difficult and expensive due to the complicated internal structure [62, 74].

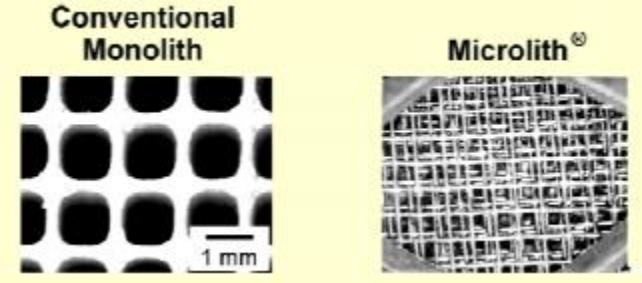

Figure 13. Characteristics of conventional, long honeycomb monolith and Microlith substrates of a Microlith-based Sabatier reactor designed for NASA to use in low-earth orbit and long-term extraterrestrial missions [72].

Three-phase slurry bubble reactors (Figure 14) and plasma-catalytic reactors have also been reported [64, 75-77]. CO_2 conversion of 90% was attained in a three-phase methanation reactor at 275 °C and 10 bar [77]. The limitations of this reactor design are the gas-to-liquid mass transfer resistance and the decomposition and evaporation of the heat transfer liquid. Götze et al. [78] suggested combining the three-phase design with a honeycomb methanation reactor, as illustrated in Figure 15. The three-phase methanation reactor can be operated nearly isothermally in this design. Due to the tolerance to reactor load variations in the three-phase methanation reactor, the system can be operated under both steady-state and dynamic conditions. Plasma-catalytic reactors can achieve good energy efficiencies and 75% CO_2 conversion was reported in one study at 182 °C [75].

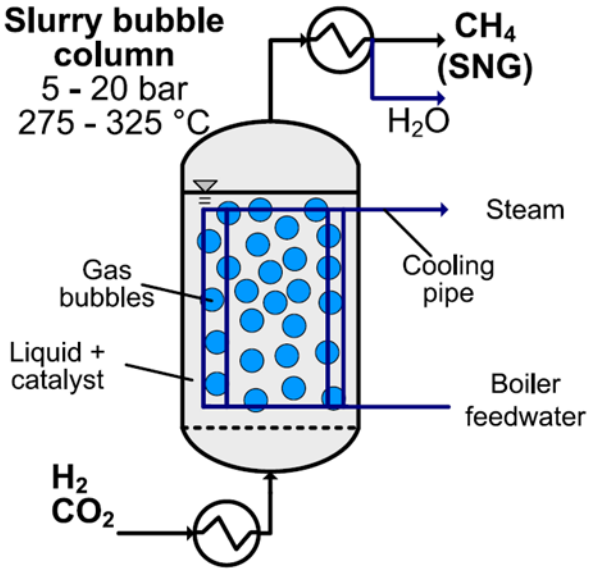

Figure 14. Three-phase CO_2 methanation reactor [76].

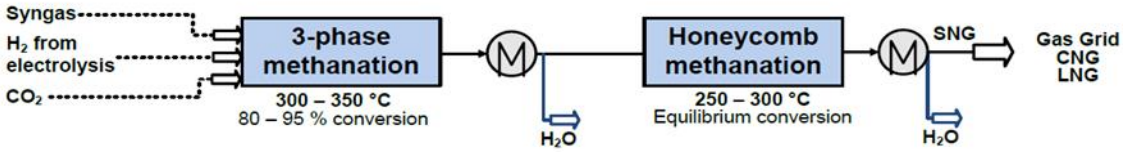

Figure 15. The hybrid three-phase/honeycomb reactor methanation system [78].

Several studies have reviewed and investigated the viability of the direct catalytic methanation of biogas and some of the authors reported experimental data on direct catalytic methanation systems. Witte et al. modeled several processes, including bubbling fluidized bed and cooled fixed bed as main upgrade reactor [48]. Model results show that both reactor types demonstrated similar chemical performance, while fixed bed reactor required about three times more catalyst compared to bubbling fluidized bed reactor. Under 45 bars CH_4 content increased from 22% to 85% after the main fixed bed reactor. With proper energy integration, the efficiencies from electricity to methane can be as high as 59%. The biomethane product

generated from the complete process meets the requirement of pipeline injection (>96% CH_4). A pilot plant in Zurich achieved 1100 hours of regular operation with 96% methane yield, utilizing a bubbling fluidized bed reactor and pretreated biogas sample [79]. Pretreated biogas was mixed with H_2 and preheated to 360 °C before feeding into the reactor inlet. A small amount of steam was also mixed with the feed stream to prevent coking formation. The product gas had 88 vol% CH_4, 11 vol% H_2 and 1 vol% CO_2. Moderate deactivation caused by organic sulfur compounds and coking was observed. Another study on direct biogas upgrade adopted a multi-tube packed bed methanation reactor with tube shell heat exchanger design and operated for 1000 hours without complications under the favorable conditions [80]. Gas concentrations at the reactor outlet were measured to be 99% CH_4, 0.7% H_2 and 0.2% CO_2 under 20 bars and H_2: CO_2=4, with synthetic biogas of 60% CH_4 and 40% CO_2. Pressurized water (65 bars) was utilized as the coolant for the reactor and the feed stream was preheated prior to entering the reactor [80].

In the study reported herein, a simple tube-and-shell design was adopted in order to investigate the possibility of the autothermal operation of a Sabatier reactor, i.e., standalone operation without any feed preheating or reactor heating. The reactor was made from stainless steel tubing using standard (Swagelok) connectors and a commercial Ni/Al_2O_3 catalyst. Three prototypes were investigated with different sizes and configurations. It was demonstrated that, after the initial feed preheating for ignition, the reactor can be continuously operated as a standalone autothermal unit, achieving 93% CO_2 conversion and 100% selectivity to CH_4 generation using a synthetic biogas feed. The same reactor also delivered 91% CO_2 conversion with 100% CH_4 selectivity using a synthetic biogas feed (without H_2S and VOCs) for 100

hours of stable operation. Experimental data, including outlet concentrations and temperature distribution, were collected using an automated system and carefully analyzed. Kinetic parameters in a Sabatier-RWGS model were estimated and the final prototype reactor was modeled in COMSOL. An analysis of the collected data is presented, and future perspectives are discussed.

Chapter 3
CO_2 methanation

3.1 Experimental

3.1.1 Reactor assembly and flow system

A small kinetic reactor built from a 1/4″ stainless steel union tee (Swagelok) was used for isothermal catalyst testing (see Fig. S2 in *Appendix B*). Three autothermal prototypes (denoted as Reactor 1, 2 and 3) were assembled scaling up gradually from 0.25″ to 0.5″ and 1″ OD (outer diameter). A commercial reforming catalyst (12 wt% Ni/Al_2O_3, BASF, supplied by Research Catalysts, Inc. USA) was used in all reactors. Catalyst pellets were crushed and sieved to 0.275-0.425 mm for the kinetic reactor and Reactors 1 and 2 and to 0.7-1 mm pellets for Reactor 3. Reactors 1, 2 and 3 (Figure 16) were designed to be operated without external heating with the reactor temperature maintained by the heat released from the Sabatier reaction. Feed preheating was only used for initial ignition and to investigate the effect of the feed temperature.

All details are provided in *Appendix B* (see Figs S3-5). Briefly, Reactor 1 was a small packed bed built from a short piece of 0.25″ stainless steel tubing with 1.4 g of catalyst loaded inside. A furnace was used for feed preheating and no active cooling was used given the small reactor size.

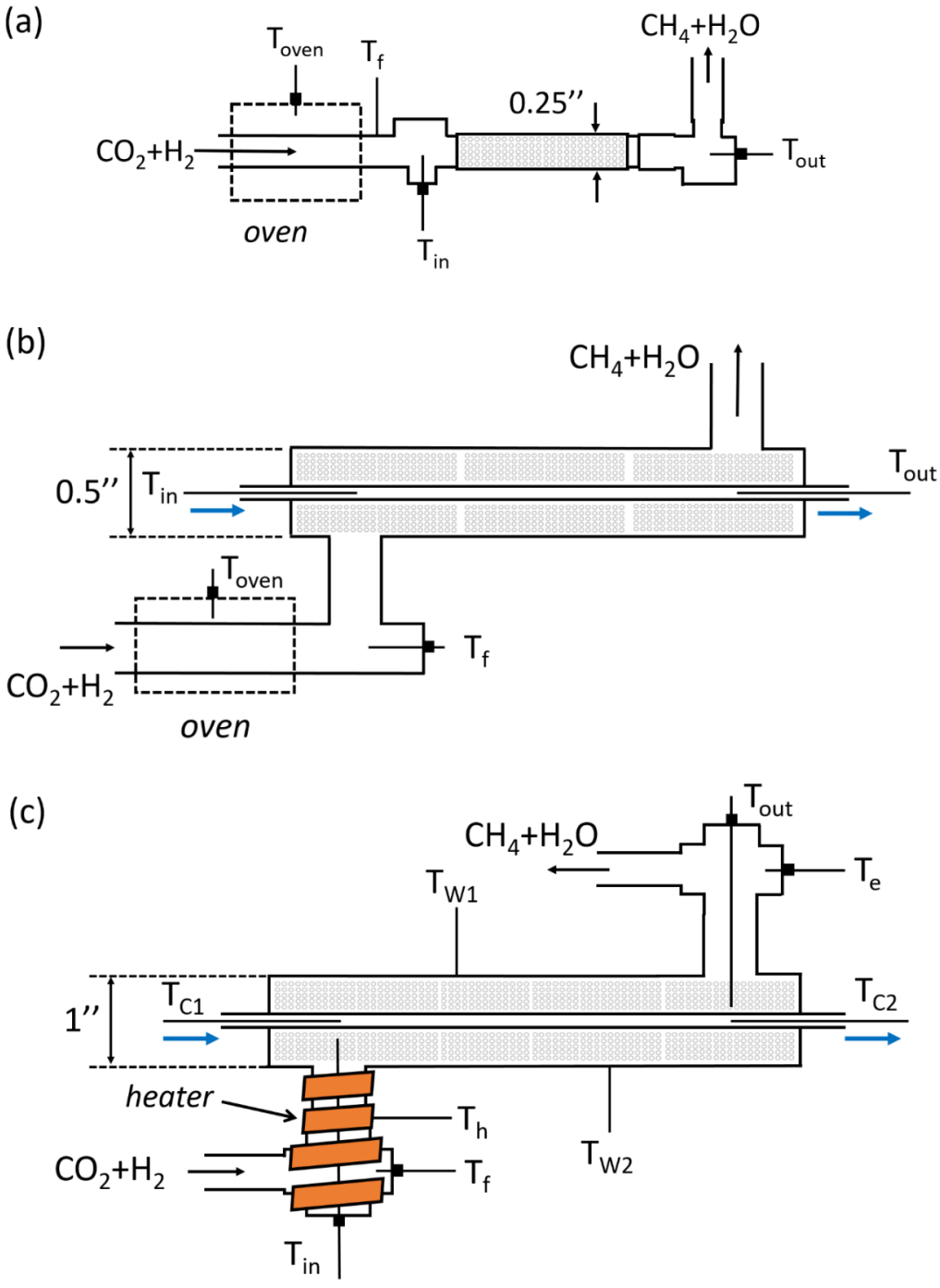

Figure 16. Schematic diagrams of Reactors 1 (a), 2 (b) and 3 (c) showing the direction of flow and locations of thermocouples.

Reactor 2 was made from a 4″ long 1/2″ OD stainless steel tube, with a piece of 1/4″ OD tube placed inside (tube-and-shell) to provide active cooling. 7.2 g of catalyst was packed inside the shell side and multiple thermocouples were used to monitor the reactor temperature. 63 g of catalyst was loaded inside the shell side of Reactor 3 made from 1″ OD stainless steel tube and additional fittings connected to the reactor body. The cooling tube OD was 1/4″. All reactors were tested using an automated flow system (see Fig. S1 in *Appendix A*). All details are provided in *Appendix A*. Briefly, the system comprises mass flow controllers, a temperature-programmable furnace, a back pressure regulator, pressure transducers, water and humidity traps, an infrared gas analyzer for exhaust gas analysis.

Table 1. Dimensions of the three prototype reactors.

	Reactor 1	Reactor 2	Reactor 3
Outer diameter, in	0.25	0.5	1
Active bed length, in	3.5	5	9
Catalyst loading, g	1.4	7.2	63

3.1.2 Catalytic performance evaluation

A kinetic reactor (Fig. S2) was used for isothermal reaction tests. In each experiment, a fresh catalyst was first reduced at 450 °C under a flow of H_2 (200 mL/min) for 1 h. After that, the reaction mixture was introduced and the temperature was reduced stepwise. At each step, the reaction was conducted for 2 h to insure that a steady-state was attained. Concentrations of CO_2, CH_4 and CO were continuously monitored using an automated flow system (see *Appendix*

A). Gas hourly space velocity (GHSV) and feed composition are defined by Eqs (4, 5). Overall CO_2 conversion and CH_4 selectivity are calculated by Eq. (7). Carbon balance is calculated by Eq. (8) (see *Appendix D* for derivation). In all experiments carbon balance was continuously calculated and monitored. Deviations did not exceed 5%, i.e., the carbon balance was in the CB = 0.95-1.05 range.

$$GHSV = \frac{Q_f}{W_c} \tag{4}$$

$$\alpha = \frac{F_{H_2,f}}{F_{CO_2,f}} \tag{5}$$

$$\begin{aligned} f_1 &= \frac{F_{CO,out}}{F_{CO_2,f}} = \frac{y_{CO}}{(y_{CO} + y_{CO_2} + y_{CH_4})} \\ f_2 &= \frac{F_{CH_4,gen}}{F_{CO_2,f}} = \frac{y_{CH_4}}{(y_{CO} + y_{CO_2} + y_{CH_4})} \end{aligned} \tag{6}$$

$$\begin{aligned} X_{CO_2} &= f_1 + f_2 \\ S_{CH_4} &= \frac{f_2}{f_1 + f_2} \end{aligned} \tag{7}$$

$$CB = \frac{F_{C,out}}{F_{C,f}} = (y_{CO_2} + y_{CO} + y_{CH_4})(1 + \alpha - f_1 - 4f_2) \tag{8}$$

The experimental errors in the reaction tests are divided into two categories: systematic errors and random errors. Systematic errors in reaction tests are errors caused by the instrumentation, including calibration of mass flow controllers, calibration of IR analyzer, measurements of temperature, pressure and weight. Random errors are unpredictable errors

caused by the environment and can affect the precision of the measurement. The relative standard deviation of the calibration of mass flow controllers and IR analyzer were found to be ±1.50% and ±6.6% respectively calculated from repeated measurements at different set points. The uncertainty in the experiment is illustrated by error bars calculated from three repeated tests (Figure 17).

3.1.3 Reactor ignition

The procedure for reactor ignition includes three steps: pre-heating and catalyst reduction, reaction ignition and switch to a predetermined set of operating conditions. The catalytic bed has to be preheated to 320-350 °C prior to ignition. An electric oven or a heating tape (see *Appendix B*) was used for initial preheating and reduction using a 10% H_2/N_2 mixture. When the ignition temperature was reached, the 10% H_2/N_2 mixture was changed to a CO_2/H_2 mixture with a 1:4 ratio ($\alpha = 4$). After CH_4 was detected in the exhaust gas by the IR analyzer, indicating the onset of ignition, the oven (heating tape) was turned off.

3.1.4 Reactor performance evaluation

After the initial ignition and stabilization of temperatures, the reactor performance was evaluated as a function of feed temperature, space velocity, pressure and coolant flow rate. Space velocity and feed ratio are defined by Eqs (4, 5). Conversion, selectivity and carbon balance are calculated by Eqs. (6-8). Temperatures and concentrations (CO_2, CH_4 and CO) were continuously monitored and recorded using an automated flow system (*Appendix A*).

3.2 Results and discussion

3.2.1 Performance of Ni/Al_2O_3 catalyst

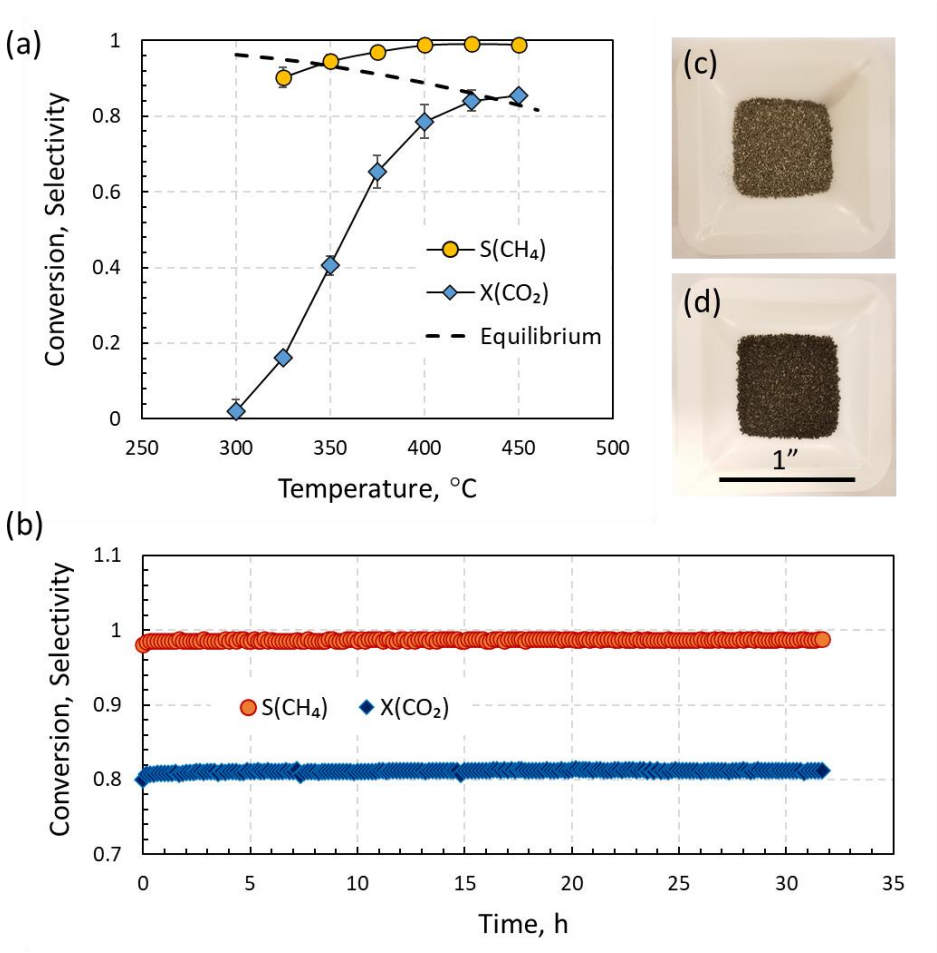

Figure 17. Ni/Al_2O_3 performance in the kinetic reactor as a function of temperature (a) and stability test (b), equilibrium conversion shown in dashed line [32]. *Parameters:* P = 3 bar, H_2:CO_2 = 4, GHSV = 30,000 L/(kg h) (a), GHSV = 100,000 L/(kg h) and T = 400 °C (b). Pictures of fresh and spent (after stability test) catalyst are shown in (c) and (d), respectively, test conducted in kinetic reactor.

Catalyst performance in terms of conversion and selectivity as a function of temperature is shown in Figure 17a. CO_2 conversion started to increase dramatically from 300 °C, and

gradually stabilize around 85% after reaching 425 °C, which is almost equal to the equilibrium conversion. Under the particular conditions of this test, the optimal temperature range is 400-450 °C, where the CO_2 conversion is above 80% and the nearly complete selectivity to CH_4 formation was achieved. The stability test is shown in Figure 17b. Both conversion and selectivity remain stable. Pictures of the fresh and spent catalysts are shown in Figure 17c,d. The color change is due to the catalyst reduction (metallic Ni has a darker color than Ni oxide). After verifying the catalytic performance of the Ni/Al_2O_3 catalyst, three reactor prototypes were tested, gradually increasing the reactor size and catalyst amount (see *Appendix B* for detailed description and pictures of the prototypes).

3.2.2 Reactor performance investigation

3.2.2.1 Reactor 1

Reactor ignition is shown in Figure 18. During the first 5 h, the reactor was heated and the catalyst was reduced using the oven-preheated 10% H_2/N_2 mixture. Note that the temperatures stabilize after ca. 2 h, but an additional 3 h was given for efficient catalyst reduction. Ignition takes place immediately after changing the reduction mixture to the reaction mixture at ca. 5 h, as evident from the sharp rise of the temperatures and appearance of CH_4 and CO signals. Both inlet and outlet reactor temperatures increase simultaneously, while the outlet temperature jump is much more significant. This observation probably indicates that the ignition occurs closer to the reactor outlet. Note that the length of the catalytic bed in Reactor 1 is 9 cm (see *Appendix B* for reactor configuration details). The fact that there is a small jump in the feed temperature (a thermocouple was in contact with the inlet tube wall, see the

schematic in Figure 18) indicates that there is a significant axial conductivity against the direction of the flow.

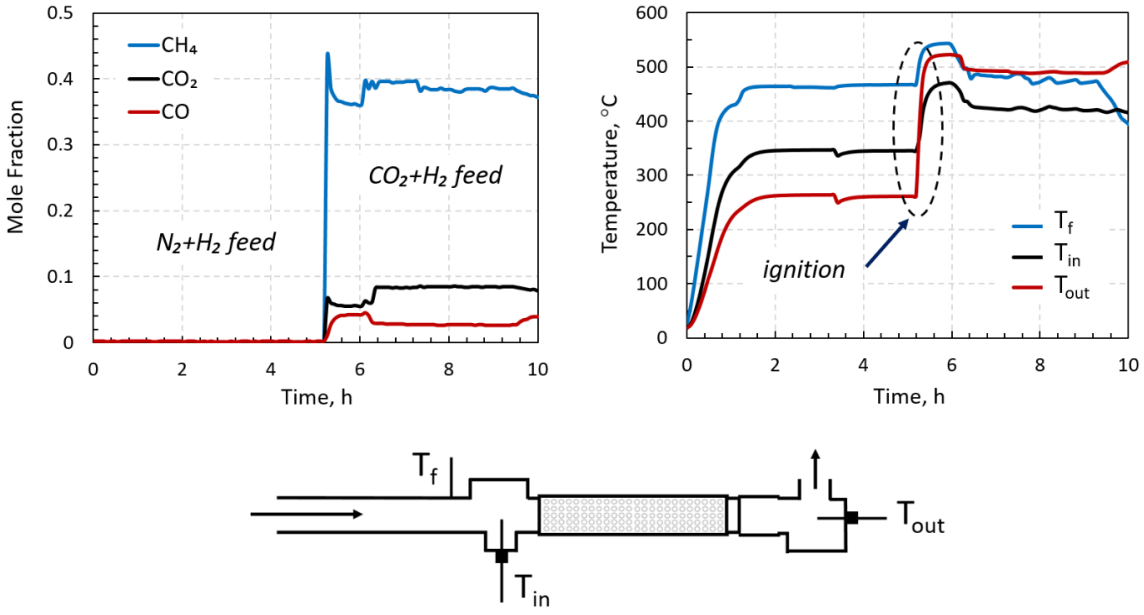

Figure 18. Mole fractions in the reactor outlet (off gas) and reactor temperature profiles during the reactor ignition. *Parameters*: P = 1 bar, H_2:CO_2 = 4, GHSV = 35,000 L/(kg h).

After ignition, the feed temperature was reduced to 100 °C, the pressure was increased to 7 bar (high pressure is favorable for Sabatier reaction) and the reactor was left until stabilization of temperatures and outlet mole fractions. After that, the feed temperature was gradually increased to 400 °C, while ensuring steady-state stabilization at each step. The results are shown in Figure 19a,b. No significant effect on conversion and selectivity was found. The selectivity to CH_4 generation remained nearly 100% and the CO_2 conversion dropped slightly from 92% to 90%, Figure 19a. It is interesting that for T_f = 100 °C when the inlet/outlet reactor temperatures are ca. 270-275 °C, the conversion is 92%, which is not expected for such low

temperatures. A possible explanation is that a hot spot was located in the middle of the reactor. Therefore, axial temperature gradients are very significant even for such a small catalytic bed (0.25″ OD, 3.5″ L, 1.4 g catalyst).

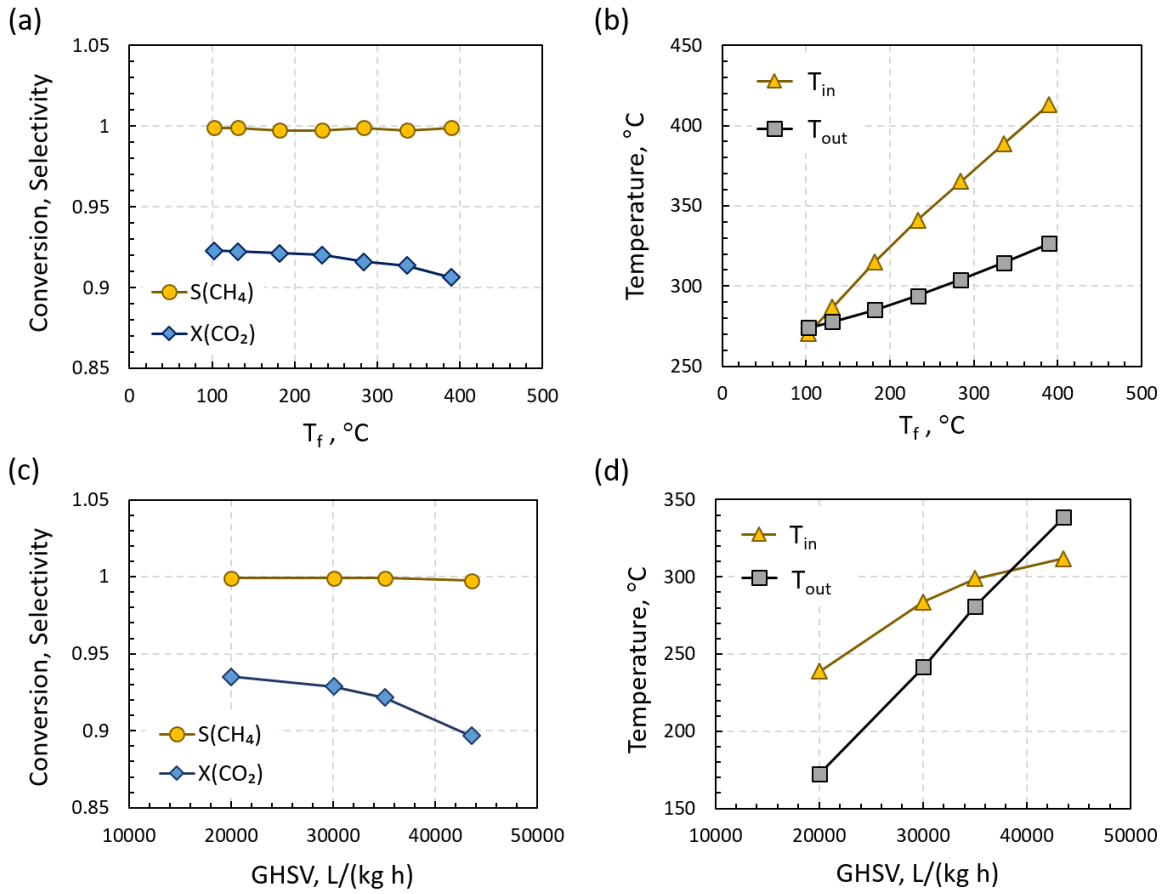

Figure 19. Effect of feed temperature and space velocity on the reactor performance and temperatures. *Parameters*: P = 7 bar, H_2:CO_2 = 4, GHSV = 35,000 L/(kg h) (a, b), T_f = 120 °C (c, d).

Interestingly, the increase in both the inlet and outlet temperatures was very substantial, with the inlet temperature being significantly higher, Figure 19b. Another interesting observation is that, while there was virtually no difference between the inlet and outlet reactor

temperatures at T_f = 100 °C and this difference increases with increasing feed temperature. The effect of space velocity (for T_f = 120 °C) is shown in Figure 19c,d. Although the reactor temperatures increase very significantly with increasing space velocity (due to a higher rate of heat generation), the change in conversion is rather minor. Probably the most important observation from this set of experiments is that the 90-93% conversion and ca. 100% selectivity is maintained in the 20,000-45,000 L/(kg h) and T_f = 100-400 °C range when the axial temperature gradient varies very significantly. These findings emphasize the importance of investigations of spatially distributed reactors, even at a laboratory scale.

3.2.2.2 Reactor 2

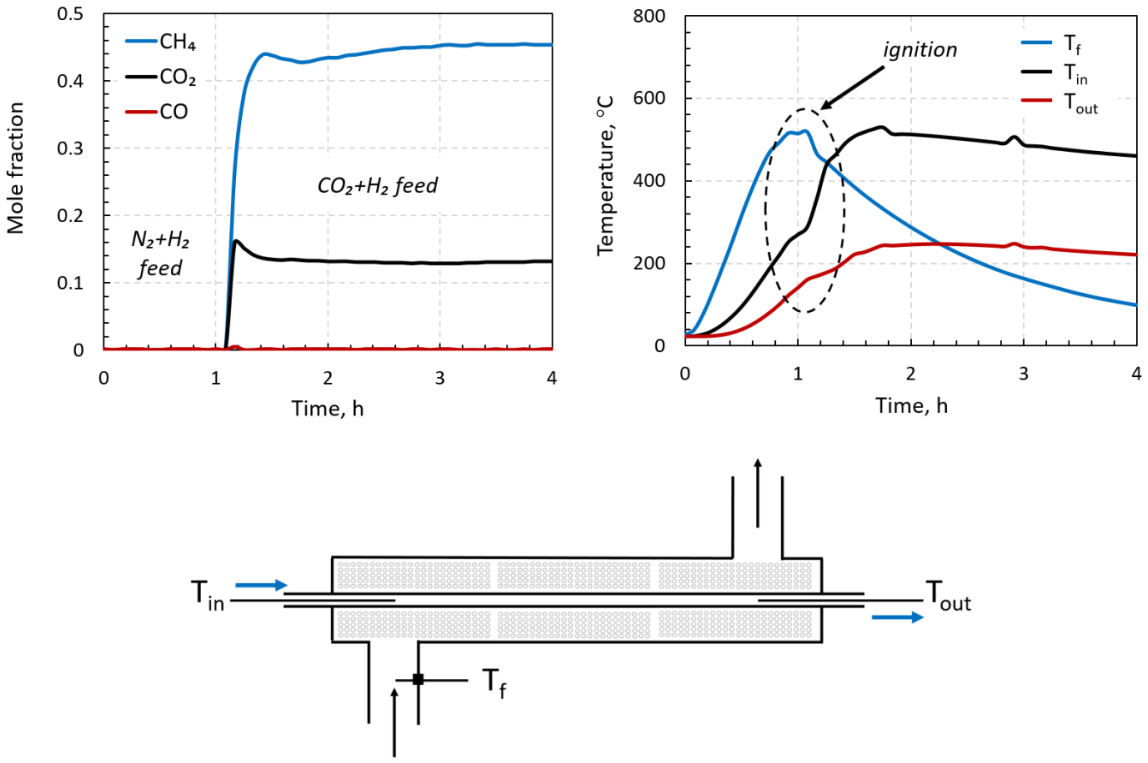

Figure 20. Reactor temperatures and outlet mole fractions during Reactor 2 ignition. *Parameters*: GHSV = 16,000 L/(kg h), H_2:CO_2 = 4, P = 1 bar, Q_c = 0 L/min.

The ignition process of Reactor 2 looks quite different from that of Reactor 1, which can be attributed to the larger size of this reactor (0.5″ OD, 5″ L, 7.2 g of catalyst). The reaction mixture was introduced when the inlet temperature reached ca. 280 °C immediately resulting in reactor ignition as evident from the appearance of CH_4 signal. Only a very small, nearly negligible signal of CO was detected, as opposed to Reactor 1 ignition. Upon ignition, the inlet temperature increased from 280 °C to ca. 520 °C, while the outlet temperature went up by only ca. 100 °C. The feed preheating oven was turned off after ignition until the feed temperature gradually decreased to room temperature, Figure 20.

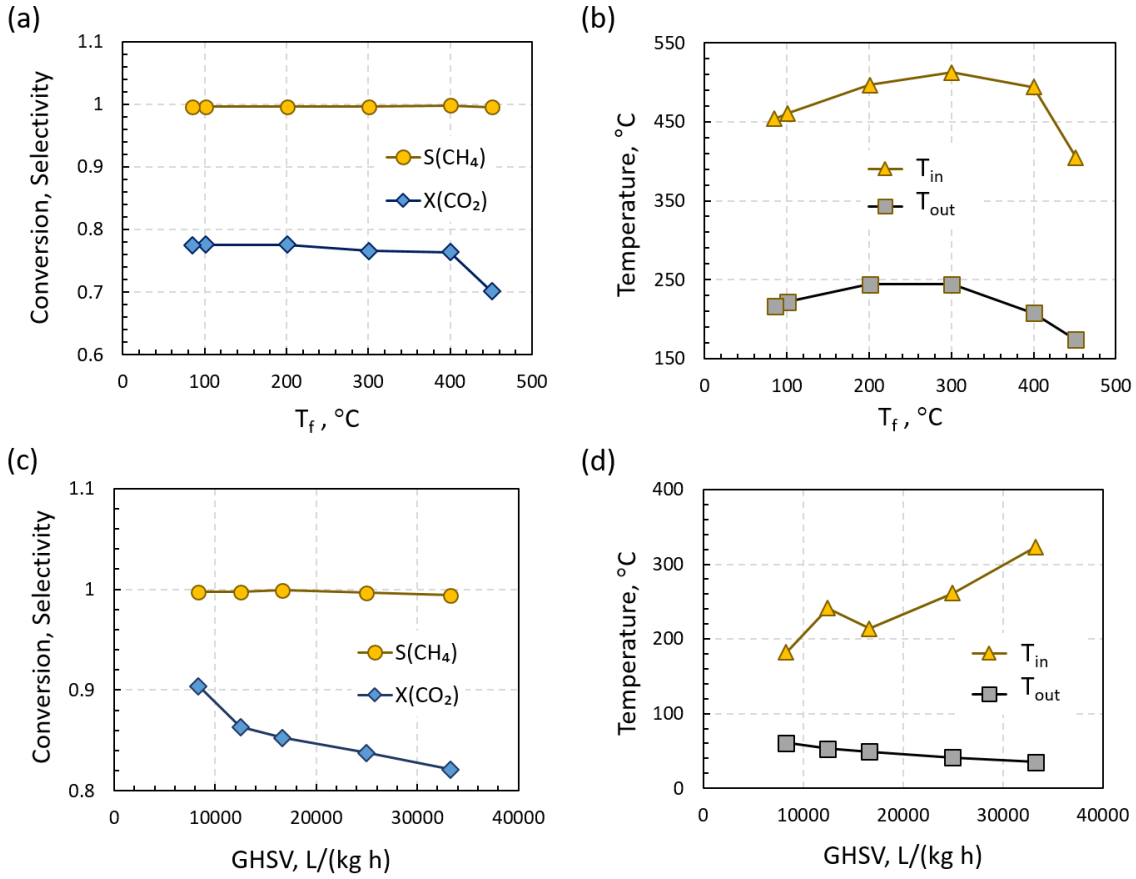

Figure 21. Reactor performance as a function of feed temperature and space velocity. *Parameters*: H_2:CO_2 = 4, Q_c = 0.8 L/min (countercurrent flow); GHSV = 16,000 L/(kg h), P = 3 bar (a, b); P = 7 bar, no feed preheating, countercurrent cooling (c, d).

The effects of feed temperature and space velocity are shown in Figure 21. During these experiments, the cooling was set in the countercurrent configuration with a cooling rate of 0.8 L/min. The selectivity to CH_4 generation was maintained at 100% under all conditions. With the increase of feed temperature in the 100-400 °C range, the conversion was 78% with a minor drop to 70% at 450 °C, Figure 21a. The reactor temperatures did not change very significantly, although a certain trend with a maximum at T_f = 200-300 °C can be seen. The inlet temperature

was significantly higher. The lower conversion was attributed to a lower reactor pressure, which was subsequently increased to 7 bar (similar to Reactor 1).

The effect of space velocity was investigated at 7 bar and T_f = 20 °C, Figure 21c,d. There is ca. 10% conversion drop in the 8,000-33,000 L/(kg h) range, with the maximum CO_2 conversion of 91% obtained at the lowest space velocity (expected), Figure 21c. The selectivity to CH_4 production was 100% in the entire range. With the increase of space velocity, the reactor inlet temperature increased significantly (from 180 to 320 °C), while the outlet temperature remained at 40-50 °C, Figure 21d.

The effect of reactor pressure is shown in Figure 22a,b. As expected, the CO_2 conversion gradually increases (from 77% to 85%) as the reactor pressure is increased from 1 to 7 bar. No CO formation was observed. There is also a small decline in the outlet temperature, which is also significantly lower than the inlet reactor temperature. Since the inlet temperature was only ca. 210 °C and 77-85% conversion cannot be achieved for such a low temperature, it can be concluded a hot spot formed between the inlet and outlet. This observation emphasizes the importance of the axial temperature gradients.

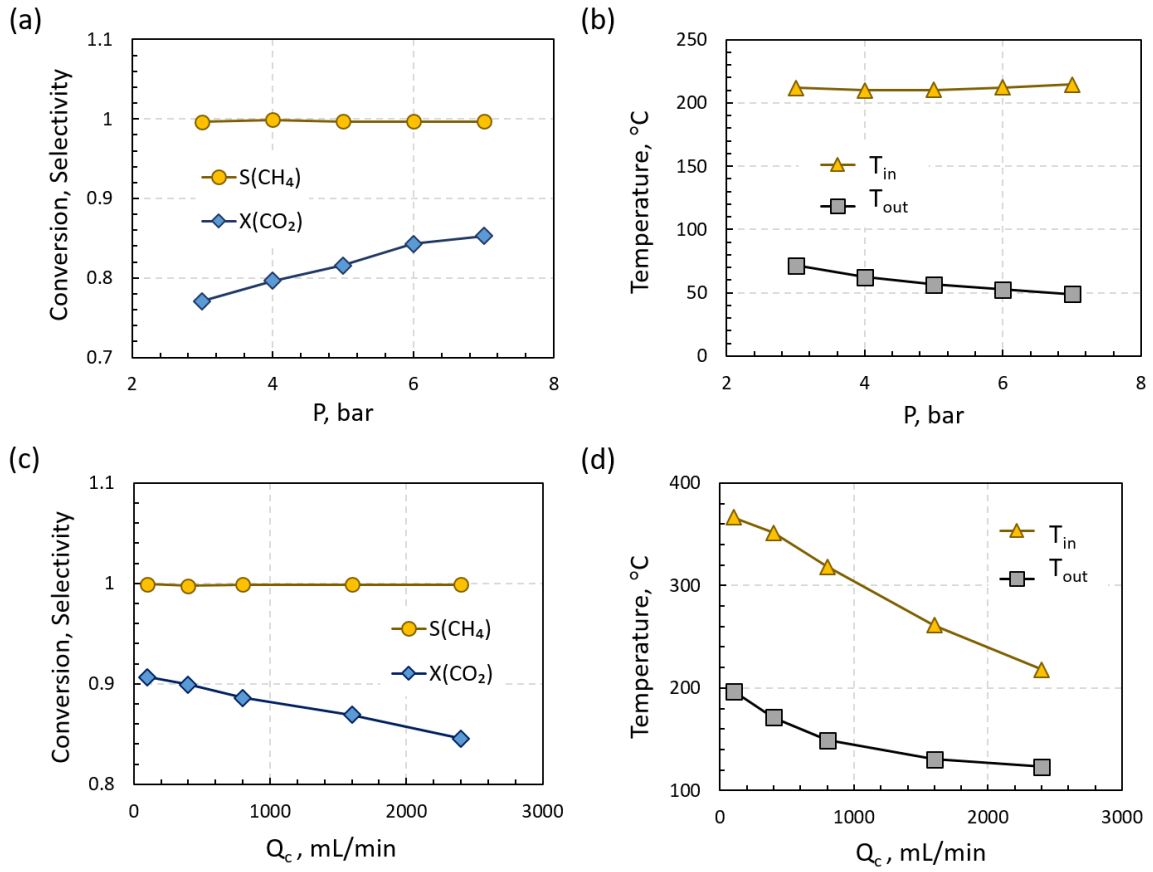

Figure 22. Reactor performance as a function of pressure and cooling flow rate. *Parameters*: T_f = 20 °C, H_2:CO_2 = 4; Q_c = 0.8 L/min (countercurrent flow), GHSV = 16,000 L/(kg h) (a, b); P = 3 bar, GHSV = 8,000 L/(kg h) (c, d).

The effect of the cooling rate is shown in Figure 22c,d. The efficiency of cooling is evident from Figure 22d. As the cooling rate increases in the 0-2.5 L/min range, the inlet temperature drops from 370 °C to 220 °C and there is a decline in the outlet temperature as well. However, the effect of cooling on the conversion is rather minor, Figure 22c.

3.2.2.3 Reactor 3

For Reactor 3, which comprised 63 g of catalyst (1″ OD, 9″ L catalyst bed), additional thermocouples were installed, including the two thermocouples in contact with the external reactor wall (see Fig. S5 and *Appendix B* for details). Reactor ignition is shown in Figure 23. Note that the reduction time was increased due to a relatively large amount of catalyst as compared to the other two prototypes. The onset of ignition is clearly observable from the appearance of the CH_4 signal and a sharp increase of the reactor inlet temperature (T_{in}) and corresponding cooling compartment temperature (T_{C1}).

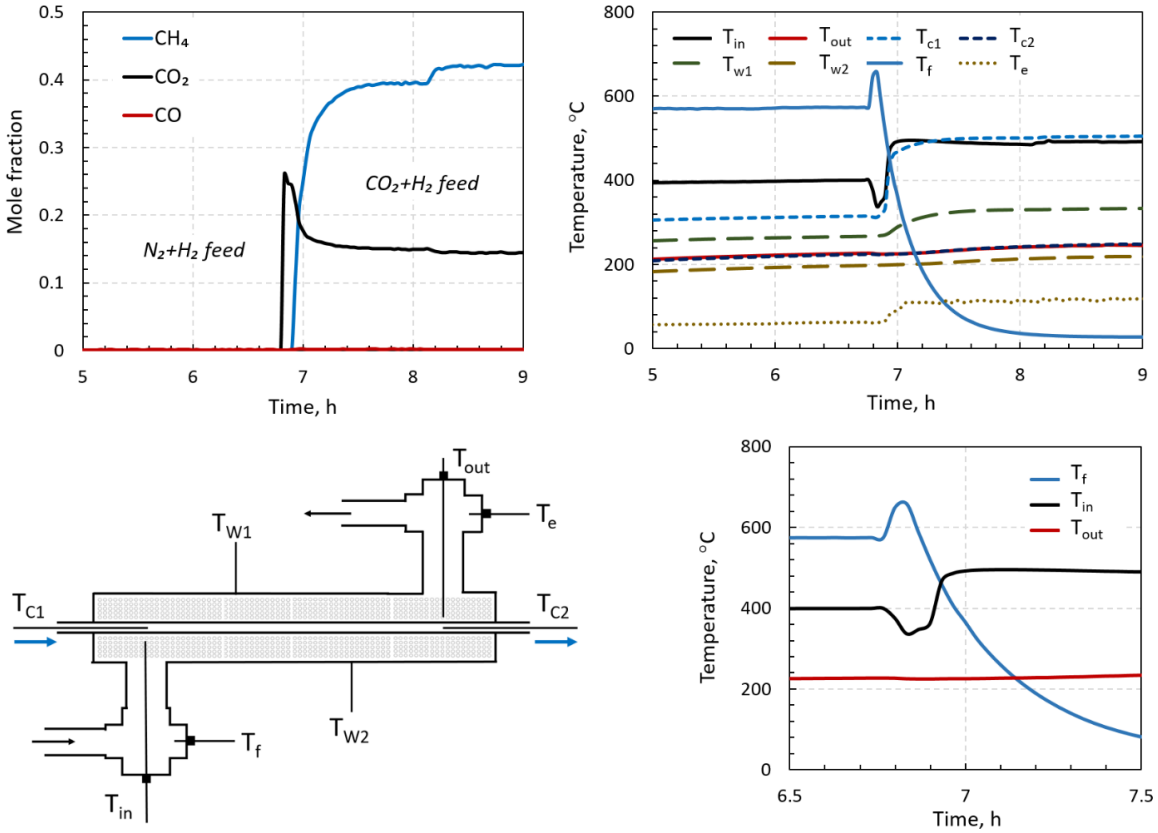

Figure 23. Reactor temperatures and outlet composition during Reactor 3 ignition. *Parameters*: H_2:CO_2 = 4, P = 1 bar, GHSV = 2,000 L/(kg h), Q_c = 0 L/min.

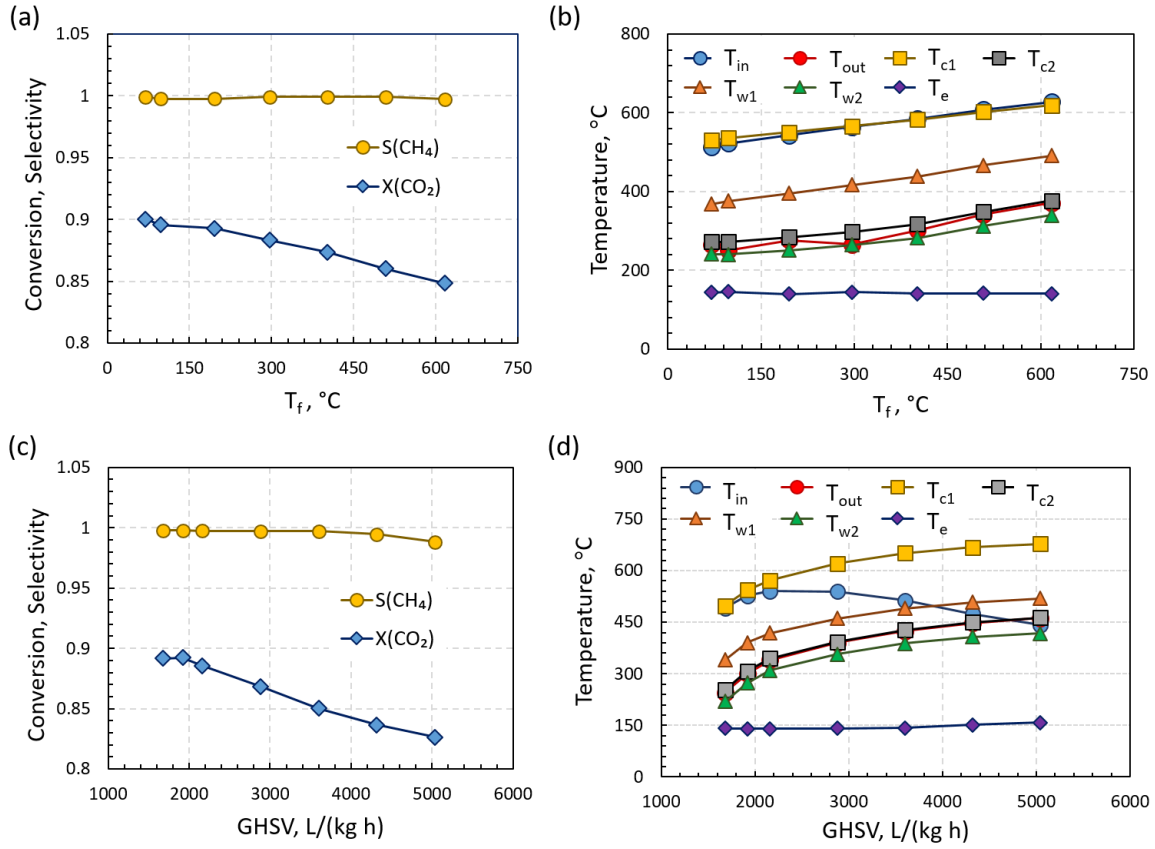

Figure 24. Reactor 3 performance as a function of feed temperature and space velocity. *Parameters*: P = 11 bar, H_2:CO_2 = 4, Q_c = 0.8 L/min (cocurrent flow); GHSV = 2,000 L/(kg h) (a, b); no feed preheating (c,d).

The effects of feed temperature and space velocity are shown in Figure 24. Increasing the feed temperature results in a nearly linear increase of all temperatures except for the effluent temperature (T_e) and a 5% drop in conversion, Figure 24a,b. Increasing the space velocity has a similar effect, Figure 24c,d, but the increase in reactor temperatures is not linear. Such behavior is expected, as reaction heat generation is a non-linear process as opposed to feed preheating, which is linear. The inlet temperature (T_{in}) starts to decrease at a certain space velocity, Figure 24d, indicating that at this point the cooling effect of the inlet stream is more

significant than the heat generation effect. Except for GHSV = 5,000 L/(kg h), the selectivity to CH_4 formation was nearly complete and the CO_2 conversion remained in the 82-90% range in this set of experiments. As it can be seen from Figure 24b, the inlet/outlet reactor temperatures (T_{in} and T_{out}) are virtually identical to the corresponding coolant temperatures (T_{C1} and T_{C2}). On the other hand, for increasing space velocity the difference between T_{in} and T_{C1} becomes significant, Figure 24d. Values of the wall temperatures (T_{W1} and T_{W2}) clearly show that there is a downstream-declining axial temperature gradient, which can be attributed to the heat losses, which are significant even for a relatively thick insulation layer used (Fig. S5).

The effects of the cooling rate and direction are presented in Figure 25 which compares cocurrent (CC) and countercurrent (CNC) configurations in a range of cooling flow rates. Note that the reactor was operated completely autothermally in this set of experiments, with no feed preheating (except for initial ignition). Inlet reactor temperatures (T_{in} and T_{C1}) do not depend significantly on the cooling direction, indicating that the inlet reactor temperature is mainly determined by the heat release from the Sabatier reaction. As the cooling rate increases, both inlet temperatures (T_{in} and T_{C1}) decline. Note that T_{C1} was substantially higher than T_{in}, due to a relatively high space velocity used in this set of experiments. As opposed to the reactor inlet, the outlet reactor temperatures (T_{out} and T_{C2}) differ quite significantly, depending on the operation mode. As expected, the outlet temperatures for the cocurrent cooling mode are significantly higher than those for the countercurrent cooling.

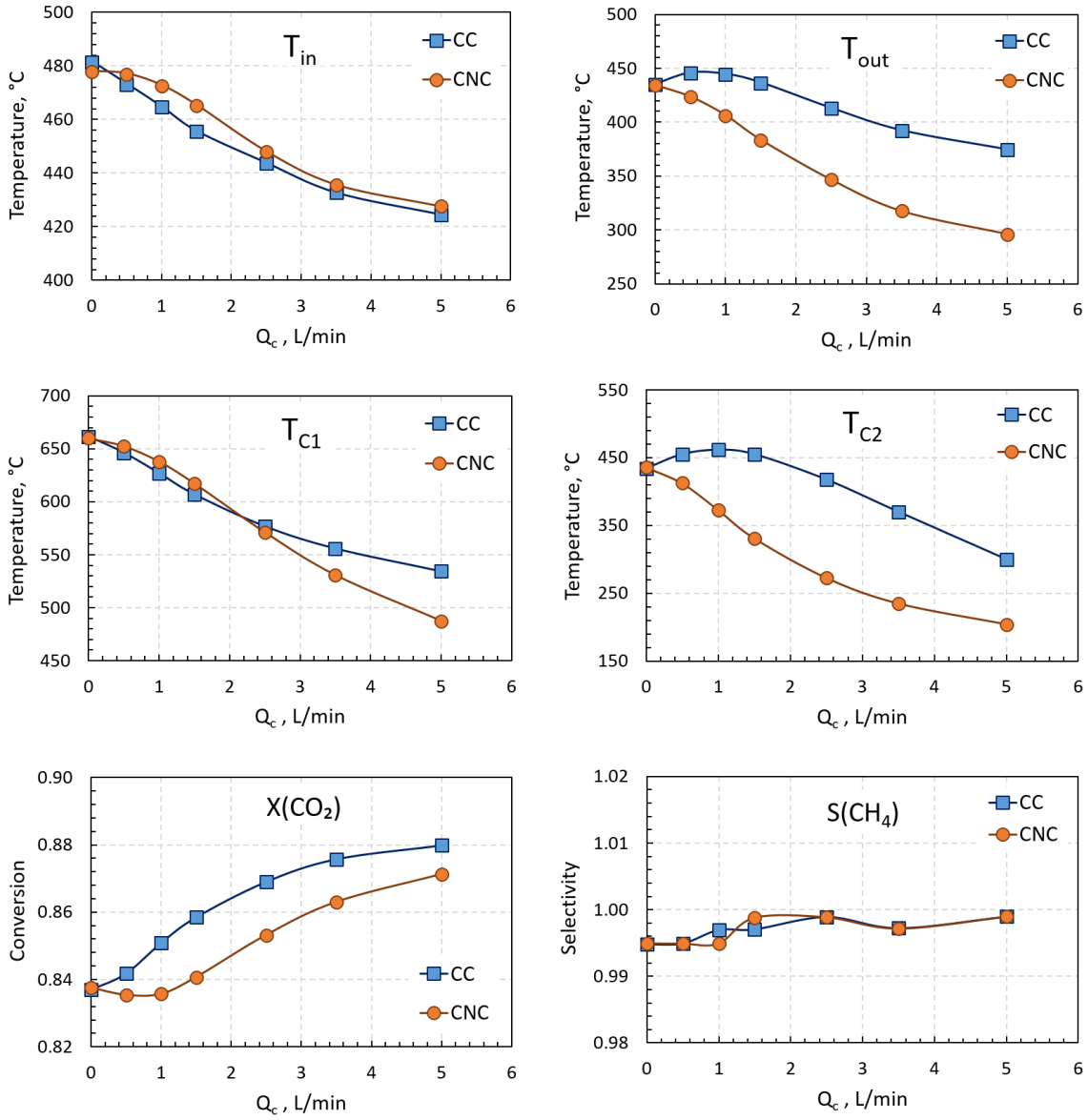

Figure 25. Effects of the cooling rate and direction (CC – cocurrent flow; CNC – countercurrent flow) on the reactor temperatures and reactor performance (in terms of conversion and selectivity). *Parameters*: P = 11 bar, H_2:CO_2 = 4, GHSV = 4,300 L/(kg h), no feed preheating.

Regarding the reactor performance, the CH_4 selectivity was nearly 100% under all conditions for this set of experiments, with a minor improvement from 99.5% to ca. 100% for

increasing cooling rates. There is ca. 2% CO_2 conversion improvement for the cocurrent operation mode. It is interesting that, although quite significant temperature changes were observed at the reactor outlet, the cooling mode did not affect CO_2 conversion to a significant extent. Similar to the previous observations for Reactors 1 and 2, the reactor performance is quite robust with respect to significant variations in the reactor temperature distribution.

3.2.2.4 Stability

Stability is an important aspect of catalytic performance often overlooked in laboratory studies. It is of particular importance to investigate the catalyst stability in a spatially distributed reactor with axial temperature gradients. From a practical standpoint, reactor stability is clearly of crucial importance and poor reactor stability will increase maintenance and operating costs significantly (e.g., for catalyst replacement).

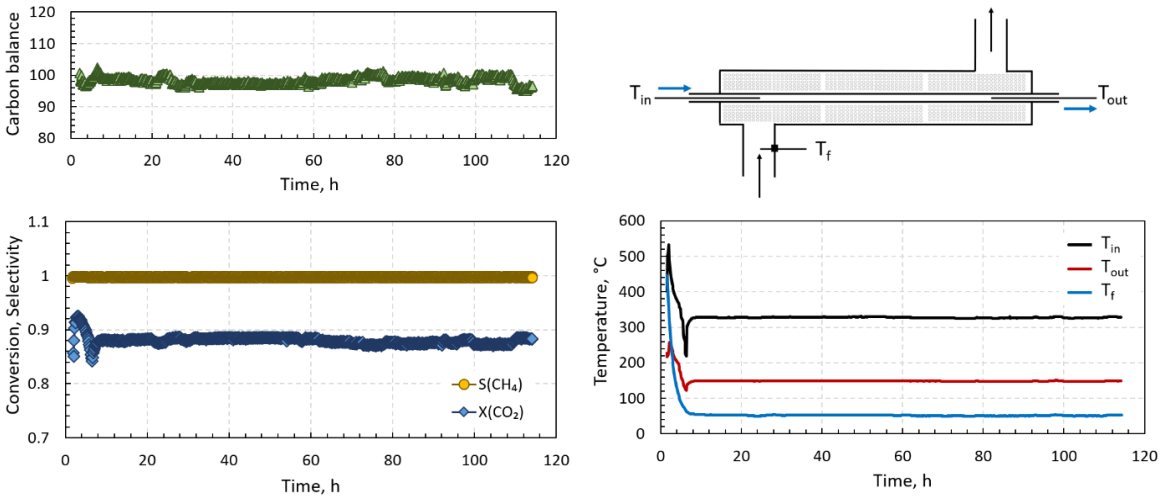

Figure 26. Reactor 2 stability test, showing the carbon balance, conversion, selectivity and reactor temperatures. *Parameters*: H_2:CO_2 = 4, GHSV = 2,400 L/(kg h), P = 7 bar, Q_c = 0.4 L/min (countercurrent flow), no feed preheating (after ignition).

Figure 26 shows the stability test for Reactor 2. After initial ignition, the reactor was operated autothermally, i.e., with no feed preheating. CO_2 conversion of 89% was achieved with 100% selectivity to CH_4 generation. Carbon balance was ca. 100% throughout the experiment (118 h). The reactor inlet and outlet temperatures were stable.

Figure 27 shows the stability test for Reactor 3. Similar to Reactor 2, the reactor was operated completely autothermally, i.e., with no feed preheating (after initial ignition). CO_2 conversion of 93.5% was achieved with 100% selectivity to CH_4 generation. Carbon balance was ca. 100% throughout the duration of the experiment (120 h). All reactor temperatures were stable. The inlet reactor temperature (T_{in}) stabilized at ca. 510 °C, with a slightly lower corresponding coolant temperature (T_{C1}) of ca. 495 °C. The wall temperatures (T_{W1} and T_{W2}) stabilized at 360 °C and 280 °C, respectively, indicating significant heat losses through the reactor wall. The outlet reactor temperature (T_{out}) was 305 °C, with a slightly higher corresponding coolant temperature (T_{C2}) of 320 °C. The effluent temperature (T_e) stabilized at 160 °C, pointing again to significant heat losses. Another 400-hour long-term stability result is shown in Fig. S16 (see *Appendix E*). This stability test consists of 9 pieces of short-term (ranges from 20 to 100 hours each test) stability results collected after multiple ignition-shutdown cycles. The reactor was still stable over a total of 400 hour period.

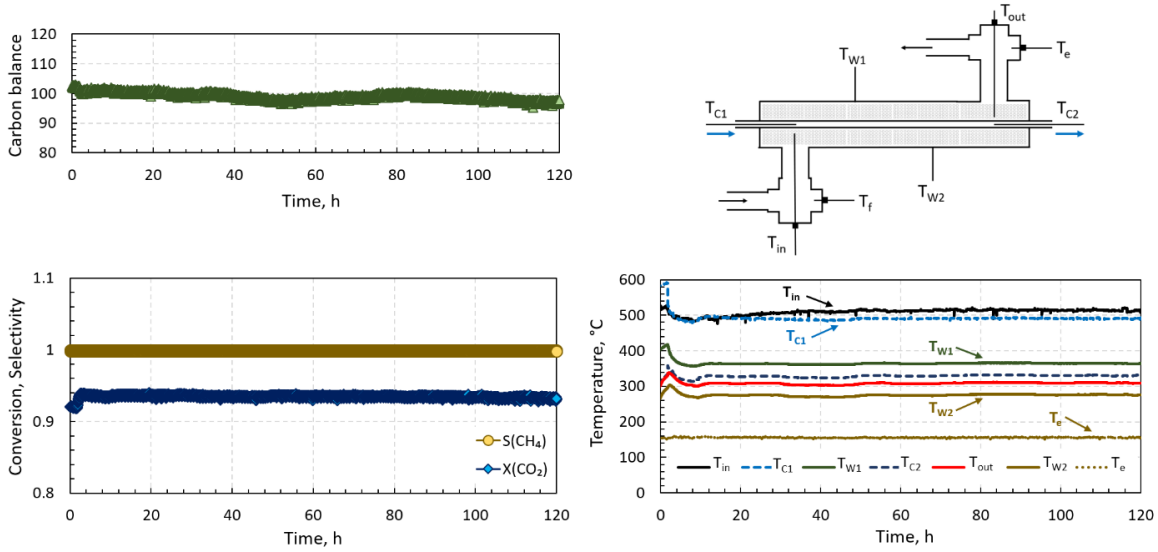

Figure 27. Reactor 3 stability test, showing the carbon balance, conversion, selectivity and reactor temperatures. *Parameters*: H_2:CO_2 = 4, GHSV = 2,400 L/(kg h), P = 14 bar, Q_c = 2 L/min (cocurrent flow), no feed preheating (after ignition).

Chapter 4
Direct biogas upgrade

4.1 Experimental

4.1.1 Reactor assembly and flow system

A commercial reforming catalyst (12 wt% Ni/Al_2O_3, BASF, supplied by Research Catalysts, Inc. USA) was used in all reactors since the performance and stability have been well demonstrated by previous work in this project. 0.8 g catalyst was loaded into a piece of 2″ long 1/4″ OD stainless steel tube (see Fig. S6 in *Appendix C*) for catalyst testing with raw biogas samples (raw biogas samples supplied by industrial partners, IGRS). Three autothermal prototypes (denoted as Reactor 1, 2 and 3) were assembled scaling up gradually from 0.25″ to 0.5″ and 1″ OD (outer diameter), the sizes shown in Table 1. Catalyst pellets were crushed and sieved to 0.275-0.425 mm for the small reactor and Reactors 1 and 2 and to 0.7-1 mm pellets for Reactor 3. Reactors 1, 2 and 3 (Figure 28) were designed to be operated without external heating with the reactor temperature maintained by the heat released from the Sabatier reaction. Feed preheating was only used for initial ignition and to investigate the effect of the feed temperature. The three autothermal prototypes are the same reactor utilized in Chapter 3, with minor modifications on the outside, i.e., thermal insulation and placement of thermocouples.

All details are provided in *Appendix C* (see Figs S7-9). Briefly, Reactor 1 was a small packed bed built from a short piece of 0.25″ stainless steel tubing with 1.4 g of catalyst loaded inside. A furnace was used for feed preheating and no active cooling was used given the small reactor size.

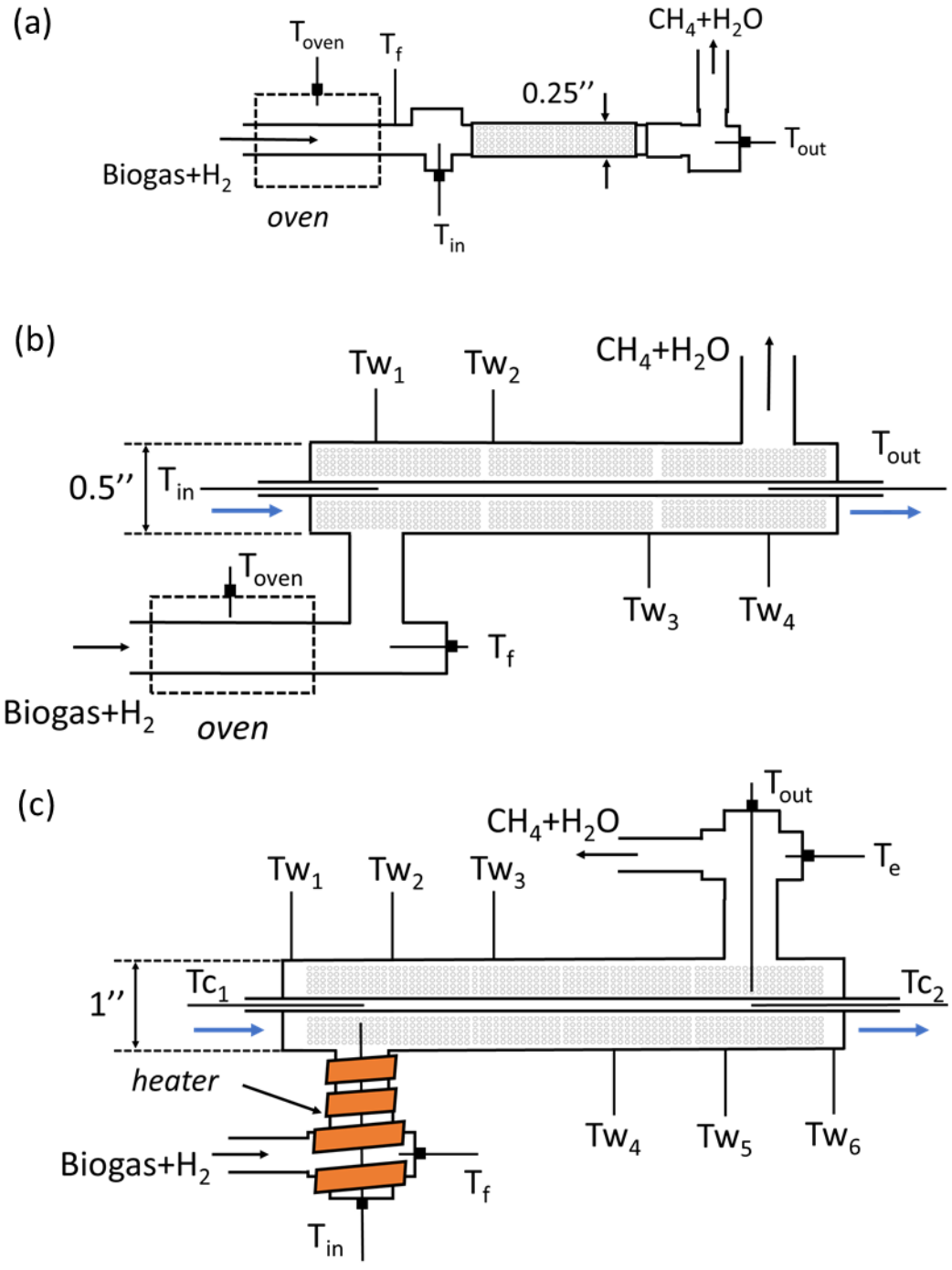

Figure 28. Schematic diagrams of Reactors 1 (a), 2 (b) and 3 (c) showing the direction of flow and locations of thermocouples.

Reactor 2 was made from a 4″ long 1/2″ OD stainless steel tube, with a piece of 1/4″ OD tube placed inside (tube-and-shell) to provide active cooling. 7.2 g of was packed inside the shell side and multiple thermocouples were used to monitor the reactor temperature. 63 g of catalyst was loaded inside the shell side of Reactor 3 made from 1″ OD stainless steel tube and additional fittings connected to the reactor body. The cooling tube OD was 1/4″. All reactors were tested using an automated flow system (see Fig. S1 in *Appendix A*). All details are provided in *Appendix A*. Briefly, the system comprises mass flow controllers, a temperature-programmable furnace, a back pressure regulator, pressure transducers, water and humidity traps and an infrared gas analyzer and a microGC for off-gas analysis.

4.1.2 Raw biogas upgrade performance study

Raw biogas upgrade tests were conducted in a 2″ long 1/4″ OD stainless steel tube packed bed reactor (Fig. S6). In each experiment, a fresh batch of catalyst was first reduced at 450 °C under a flow of H_2 (200 mL/min) for 1 h. After initial reduction, the H_2-biogas mixture was introduced to the reactor, and the temperature was reduced stepwise. In one of the stability tests, lab-prepared synthetic biogas was fed instead of raw biogas to evaluate the possibility of studying the catalytic performance without the need for a real sample, since the raw biogas samples contain poisonous H_2S content and are difficult to transport. The compositions of raw and synthetic biogas are shown in Table 2 and Table 3. At each step, the reaction was conducted for 2 h to ensure that a steady state was attained. Concentrations of CO_2, CH_4 and CO were continuously monitored using an automated flow system (see *Appendix A*). Gas hourly space velocity (GHSV) and feed composition are defined by Eqs (9, 10). CO_2

conversion and CH_4 selectivity are calculated by Eqs. (11, 12). Carbon balance is calculated by Eq. (13) (see *Appendix D* for derivation).

Table 2. Raw biogas specifications (provided by industrial partners, IGRS).

CH_4	CO_2	N_2	O_2	H_2O	H_2S	VOC
42% vol.	29% vol.	23% vol.	4% vol.	2% vol.	600 ppm	3000 ppm

Table 3. Synthetic biogas composition.

Synthetic biogas type	CH_4	CO_2	N_2	O_2
Air balance	42.9% vol.	29.8% vol.	21.6% vol.	5.7% vol.
N_2 balance	42.9% vol.	29.8% vol.	27.3% vol.	

$$GHSV = \frac{Q_f}{W_c} \tag{9}$$

$$\begin{aligned} \alpha &= \frac{F_{H_2,f}}{F_{CO_2,f}} \\ \beta &= \frac{F_{CH_4,f}}{F_{CH_4,f} + F_{CO_2,f}} \equiv \frac{F_{CH_4,f}}{F_{C,f}} \\ \gamma &= \frac{F_{CH_4,f}}{F_{CO_2,f}} \end{aligned} \tag{10}$$

$$f_1 = \frac{y_{CO}}{(1-\beta)(y_{CO} + y_{CO_2} + y_{CH_4})} \equiv \frac{F_{CO,out}}{F_{CO_2,f}}$$
$$f_2 = \frac{y_{CH_4} - \beta(y_{CO} + y_{CO_2} + y_{CH_4})}{(1-\beta)(y_{CO} + y_{CO_2} + y_{CH_4})} \equiv \frac{F_{CH_4,gen}}{F_{CO_2,f}} \quad (11)$$

$$X_{CO_2} = f_1 + f_2$$
$$S_{CH_4} = \frac{f_2}{f_1 + f_2} \quad (12)$$

$$CB = \frac{F_{C,out}}{F_{C,f}} = (y_{CO_2} + y_{CO} + y_{CH_4})(1 + \alpha - f_1 - 4f_2 + \gamma)(1-\beta) \quad (13)$$

4.1.3 Reactor ignition

The reactor ignition procedure is the same as described in 3.1.3. The procedure for reactor ignition includes three steps: pre-heating and catalyst reduction, reaction ignition and switch to a predetermined set of operating conditions. The catalytic bed has to be preheated to 320-350 °C before ignition. An electric oven or a heating tape (see *Appendix C*) were used for initial preheating and reduction using a 10% H_2/N_2 mixture. When the ignition temperature was reached, the 10% H_2/N_2 mixture was changed to a CO_2/H_2 mixture with a 1:4 ratio (α = 4). After CH_4 was detected in the off-gas by the IR analyzer, indicating the onset of ignition, the oven (heating tape) was turned off.

4.1.4 Reactor performance evaluation

After the initial ignition and stabilization of temperatures, the pure CO_2 feed is switched to the synthetic biogas feed. The reactor performance was evaluated as a function of feed temperature, space velocity, coolant flow rate. Space velocity and feed ratio are defined by Eqs (9, 10). Conversion, selectivity and carbon balance are calculated by Eqs. (11-13).

Temperatures and concentrations (CO_2, CH_4 and CO) were continuously monitored and recorded using an automated flow system (*Appendix A*). Carbon balance was continuously calculated and monitored in all experiments.

4.2 Results and discussion

4.2.1 Raw biogas upgrade performance of Ni/Al_2O_3 catalyst

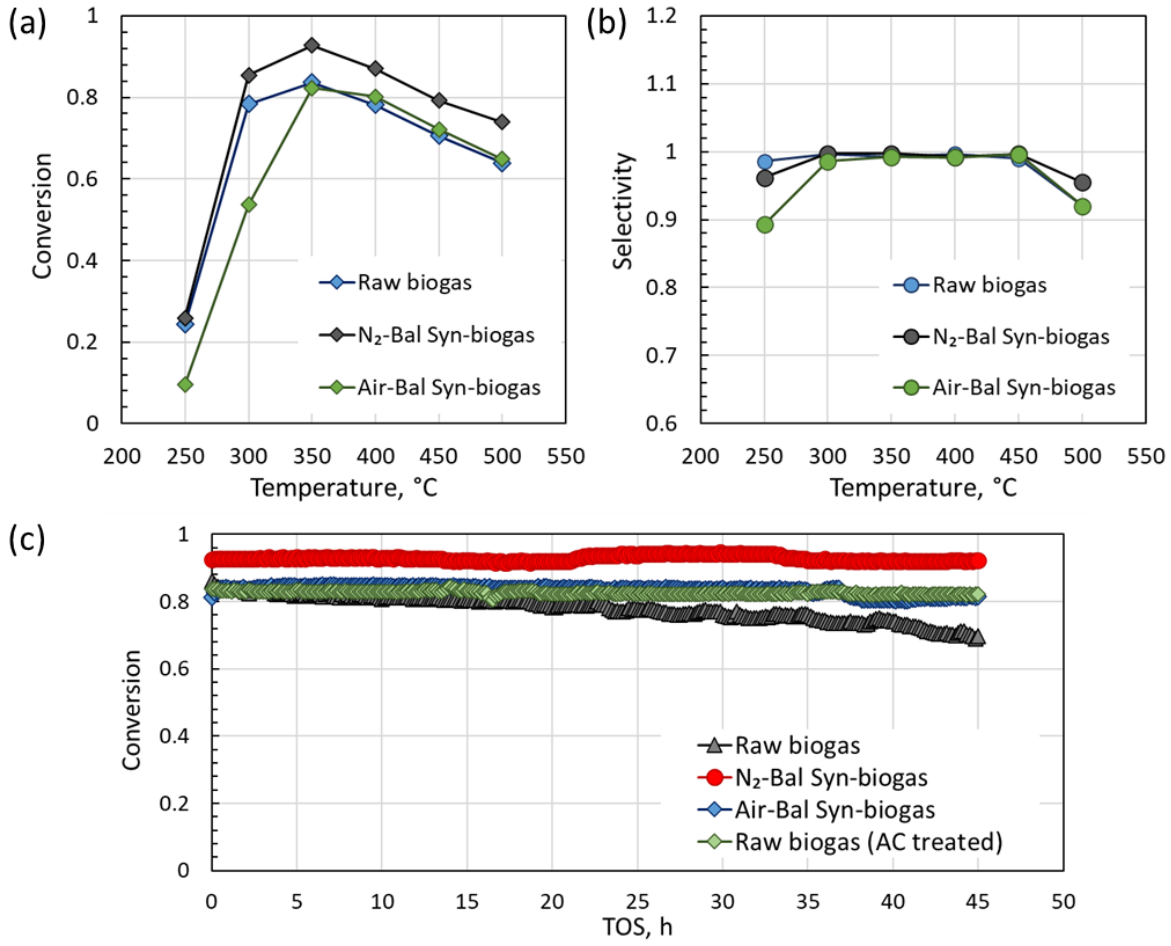

Figure 29. Ni/Al_2O_3 performance as a function of temperature (a, b) and stability test (c) using both raw and synthetic biogas as feed (Bal – balance, Syn – synthetic, AC treated – activated carbon treated). *Parameters:* GHSV=3,000 L/(kg h) (a, b), T=350°C (c), H_2:CO_2=4, P= 1 bar.

The catalytic performance in terms of conversion and selectivity as a function of temperature is shown in Figure 29a,b. Regardless of the feed, CO_2 conversion started to increase rapidly from 250 °C and reached the peak at 350 °C, then gradually went down from ~85% to 70%. Commercial Ni catalyst was able to deliver at least 80% CO_2 conversion between 300-400 °C while maintaining complete selectivity to CH_4. Overall N_2 balance synthetic biogas was found to have the highest CO_2 conversion among all mixtures, while raw biogas and air balance biogas shared very similar conversion curves slightly below N_2 balance synthetic biogas. N_2 balance synthetic biogas feed also showed the highest conversion at 93% in the stability tests, followed by raw biogas and air balance synthetic biogas, Figure 29c. CO_2 conversion gradually decreased from 84% to 69% due to catalyst poisoning caused by sulfur compounds in raw biogas. A column filled with activated carbon pellets was used to address this issue and significant deactivation was no longer observed after flowing raw biogas through the column before entering the reactor, Figure 29c. Due to the limitation of storage, transportation and supply pressure of the raw biogas, future investigation of the reactor performance required a substitute mixture sharing similar properties and composition as purified biogas. Figure 29c again demonstrated the similarities between air balance synthetic biogas and activated carbon treated biogas. It is concluded that air balance synthetic biogas can be used as a treated biogas substitute without affecting results significantly, thus all later prototype reactor testing utilized air balance synthetic biogas feed (see *Appendix C* for detailed description and pictures of the prototypes).

4.2.2 Reactor performance for direct biogas upgrade

4.2.2.1 Reactor 1

The ignition procedure was identical to the procedure described in 3.1.3. Reactor ignition is shown in. During the first 5 h, the reactor was heated and the catalyst was reduced using the oven-preheated 10% H_2/N_2 mixture. Note that the temperatures stabilize after ca. 2 h, but an additional 3 h was given for efficient catalyst reduction. Ignition takes place immediately after changing the reduction mixture to the reaction mixture at ca. 5 h, as evident from the sharp rise of the temperatures and appearance of CH_4 and CO signals. Both inlet and outlet reactor temperatures increase simultaneously, while the outlet temperature jump is much more significant. This observation probably indicates that the ignition occurs closer to the reactor outlet. Note that the length of the catalytic bed in Reactor 1 is 9 cm (see *Appendix C* for reactor configuration details). The fact that there is a small jump in the feed temperature (a thermocouple was in contact with the inlet tube wall, see the schematic in Figure 30) indicates that there is a significant axial conductivity against the direction of the flow.

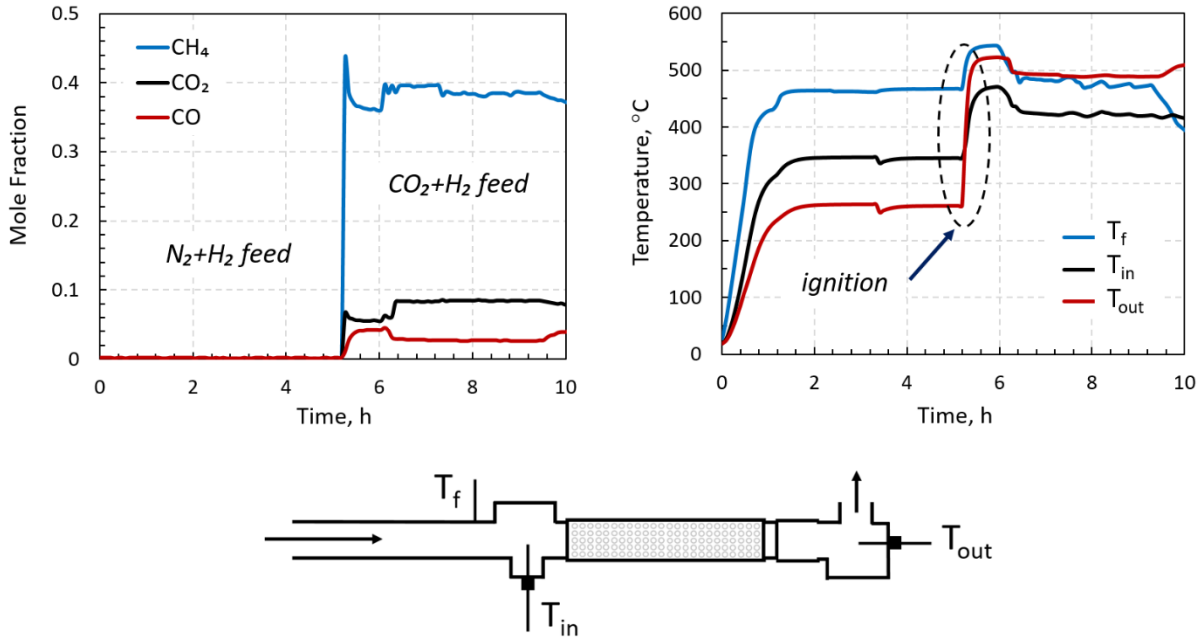

Figure 30. Mole fractions in the reactor outlet (off gas) and reactor temperature profiles during the reactor ignition. *Parameters*: P = 1 bar, H_2:CO_2 = 4, GHSV = 35,000 L/(kg h).

The preheat temperature was gradually reduced to room temperature at a step of 100 °C after the ignition, to examine the effect of feed temperature. It is shown that feed temperature had little effect over CO_2 conversion, Figure 31a, despite over 450 °C difference. Due to the additional CH_4 and N_2 content in the synthetic biogas, the space velocity had to be significantly increased, in order to generate enough heat to prevent reaction extinction. CO_2 conversion first increased from 56% to 62%, then gradually went down to 58% until the feed was no longer preheated, while CH_4 selectivity fluctuated between 65-80%, likely due to the short residence time. It is interesting that with inlet temperature dropped from 400 °C to 140 °C, the temperature at the reactor outlet maintained around 500 °C, Figure 31b. It could be explained

by a possible formation of a hotspot at the center of the reactor where the reaction rate was faster, causing the reactor to have a significant axial temperature gradient.

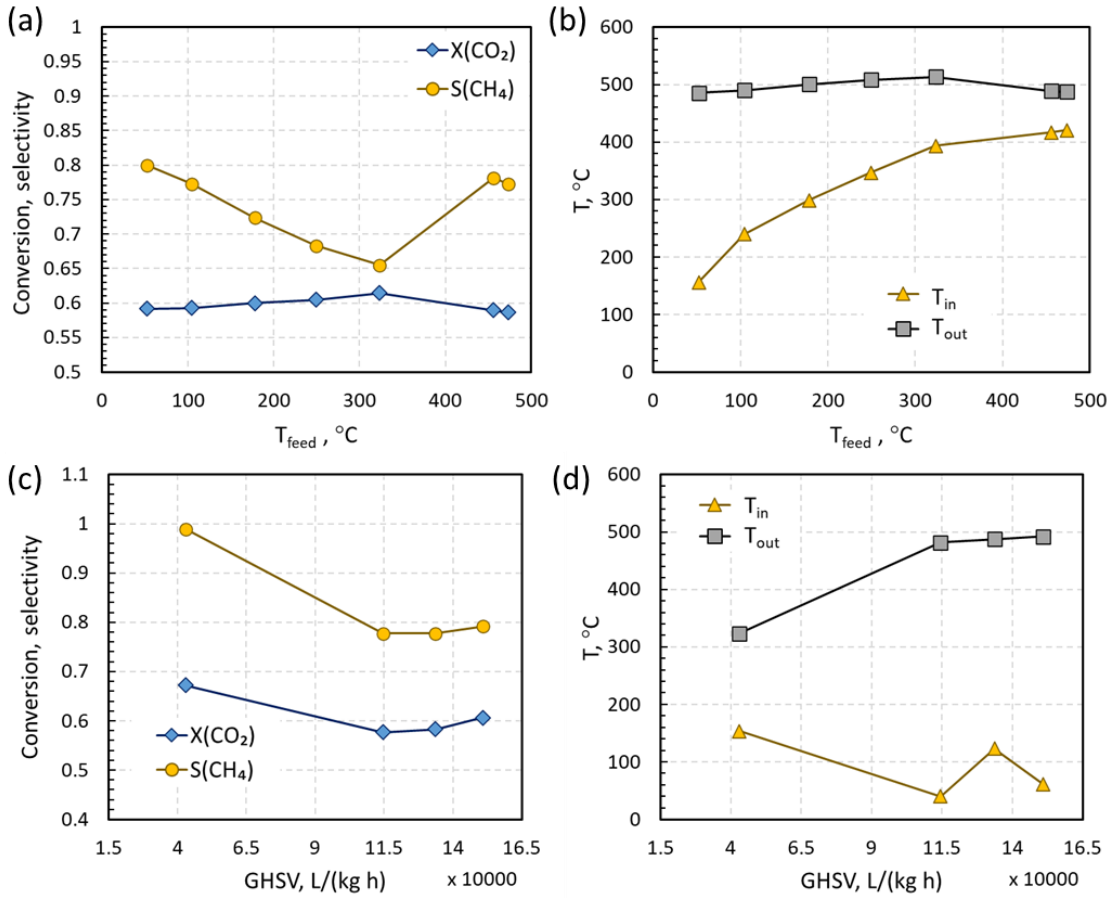

Figure 31. Effect of feed temperature and space velocity on the reactor performance and temperatures. *Parameters*: P = 1 bar, H_2:CO_2 = 4, CH_4:CO_2 = 1.43, GHSV = 133,000 L/(kg h) (a, b), T_f = 30 °C (c, d), air balance synthetic biogas feed.

Figure 31c and Figure 31d show the effect of space velocity with the synthetic biogas feed. It is expected that both CO_2 conversion and CH_4 selectivity went up slightly as the space velocity decreased, while the temperature gap between reactor inlet and outlet temperature slowly reduced from ~450 °C to 150 °C. This finding indicates the reaction might take place

mainly in a different part of the reactor, compared to the pure CO_2 feed mentioned in Chapter 3, Figure 19d. Maximum CO_2 conversion of 68% was achieved at the lowest tested space velocity 40,000 L/(kg h), which is notably lower than the conversion with pure CO_2 feed. Given the small capacity of Reactor 1, it is more important to achieve an autothermal operation with the reactor and to gain insights for future investigation.

4.2.2.2 Reactor 2

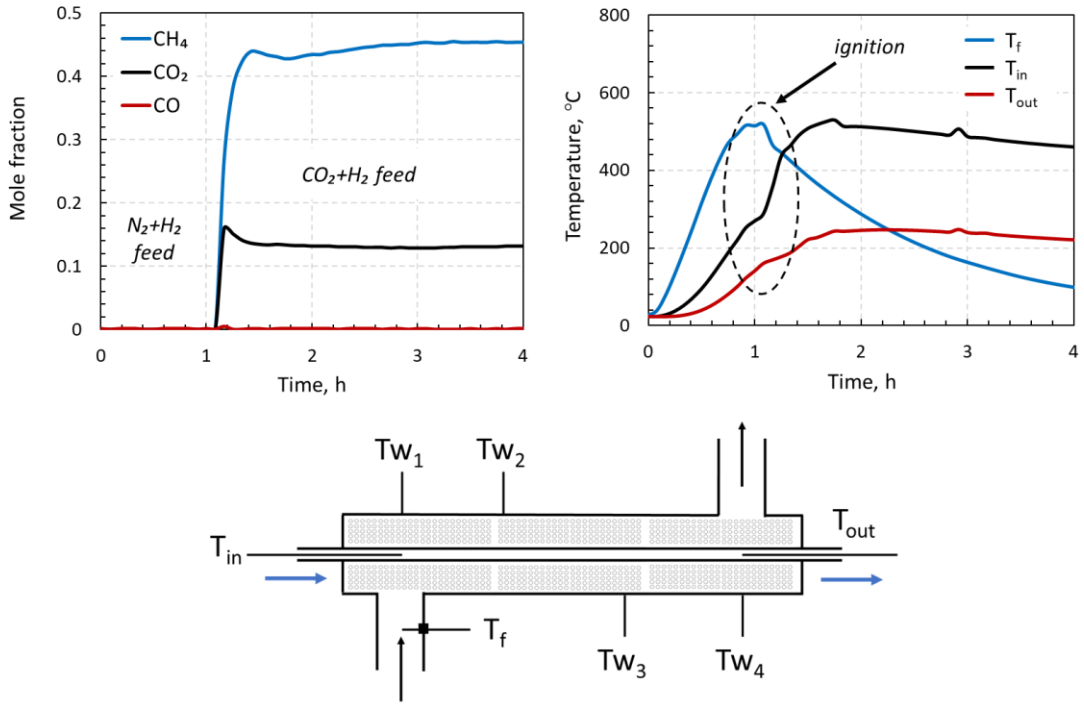

Figure 32. Reactor temperatures and outlet mole fractions during Reactor 2 ignition. *Parameters*: GHSV = 16,000 L/(kg h), H_2:CO_2 = 4, P = 1 bar, Q_c = 0 L/min.

The ignition procedure was identical to the procedure described in 3.1.3. The ignition process of Reactor 2 looks quite different from that of Reactor 1, which can be attributed to the larger size of this reactor (0.5″ OD, 5″ L, 7.2 g of catalyst). The reaction mixture was

introduced when the inlet temperature reached ca. 280 °C immediately resulting in reactor ignition as evident from the appearance of CH_4 signal. Only a very small, nearly negligible signal of CO was detected, as opposed to Reactor 1 ignition. Upon ignition, the inlet temperature increases from 280 °C to ca. 520 °C, while the outlet temperature increases by only ca. 100 °C. The feed preheating oven was turned off after ignition until the feed temperature gradually decreased to room temperature, Figure 32.

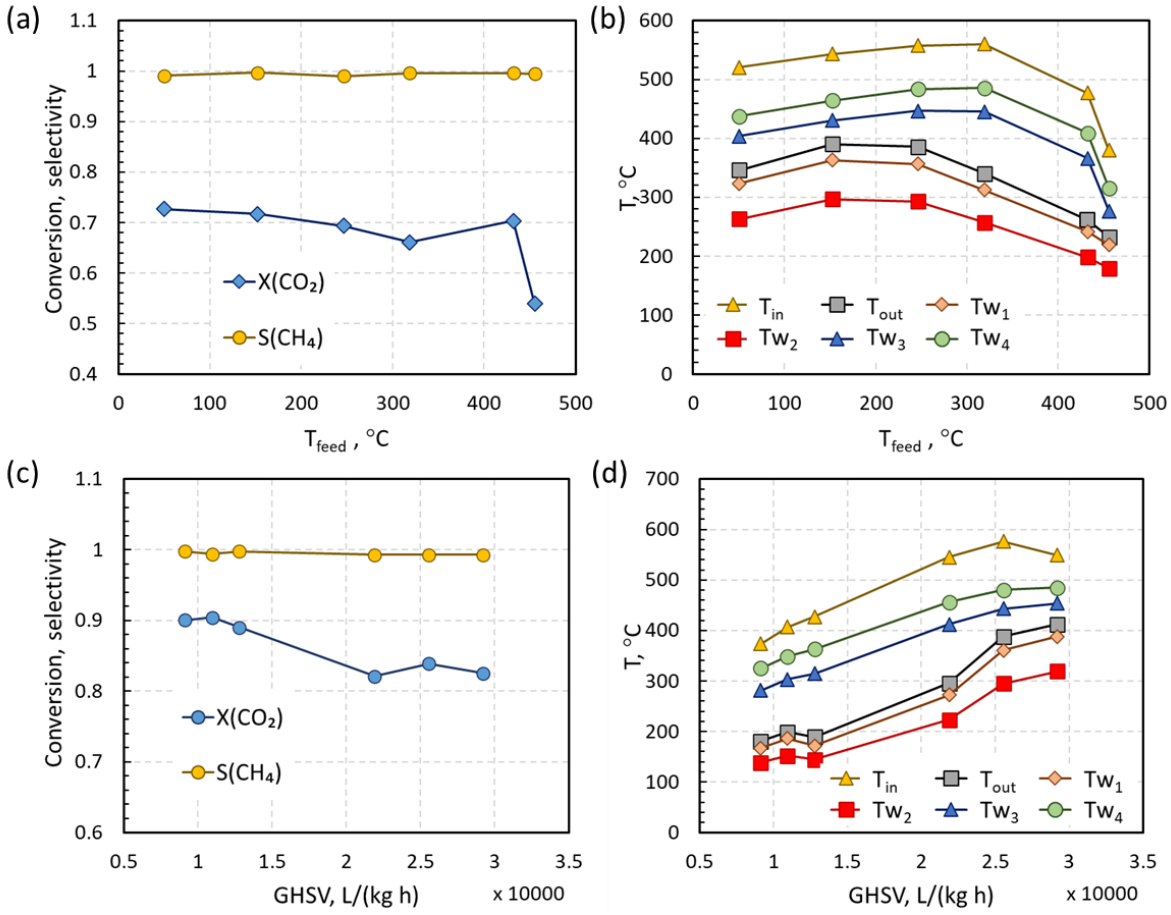

Figure 33. Reactor performance under effect of feed temperature and space velocity. *Parameters:* H_2:CO_2 = 4, CH_4:CO_2 = 1.43, Q_c = 0.25 L/min (countercurrent flow); GHSV =

22,000 L/(kg h), P = 3 bar (a, b); P = 11 bar, no feed preheating, countercurrent cooling (c, d), air balance synthetic biogas feed.

The effects of feed temperature and space velocity are shown in Figure 33. A substantial conversion increase from 52% to 70 % was observed when feed temperature dropped from 460 °C to 420 °C, and the CO_2 conversion kept going up for another 3% until preheating completely stopped, Figure 33a. The selectivity to CH_4 was maintained at 100% under all conditions. Reactor temperatures gradually went up as feed temperature decreased from 460 °C to 250 °C, then went down slightly with the feed temperature. Again, a significant temperature gradient was observed along the reactor, Figure 33b, showing a maximum of 300 °C gap between reactor inlet and outlet.

The space velocity was increased step by step after turning off the preheater and increasing pressure to 11 bars. Similar to Reactor 1, CO_2 conversion went up slightly from 81% to 90% as the space velocity decreased, which could be caused by having a longer residence time at low space velocity to form CH_4 as CO_2 methanation is commonly known to have two reaction steps [81]. Temperatures inside and on the surface of the reactor all increased significantly with the increase of space velocity, caused by the highly exothermic Sabatier reaction, Figure 33d. However, this result was quite different from the data obtained with pure CO_2 feed in Chapter 3 (temperature at the reactor outlet decreased as space velocity went up), indicating the reaction might mainly take place in a different location inside the reactor.

Figure 34 demonstrates the performance of the reactor as a function of pressure and coolant flow rate. The pressure was increased to 11 bar step by step (high pressure is favorable for Sabatier reaction) and the reactor was left until stabilization of temperatures and outlet mole

fractions. As expected, the CO_2 conversion gradually increases (from 75% to 90%) as the reactor pressure is increased from 3 to 11 bar and CO formation was not observed. Also, the slope of the CO_2 conversion declined as the pressure went higher, indicating the optimal operating pressure is probably around 10 – 15 bar. Despite the increase in CO_2 conversion, temperatures on the surface and at the outlet stayed almost unchanged, and the inlet temperature went from 360 to 400 °C, Figure 34b.

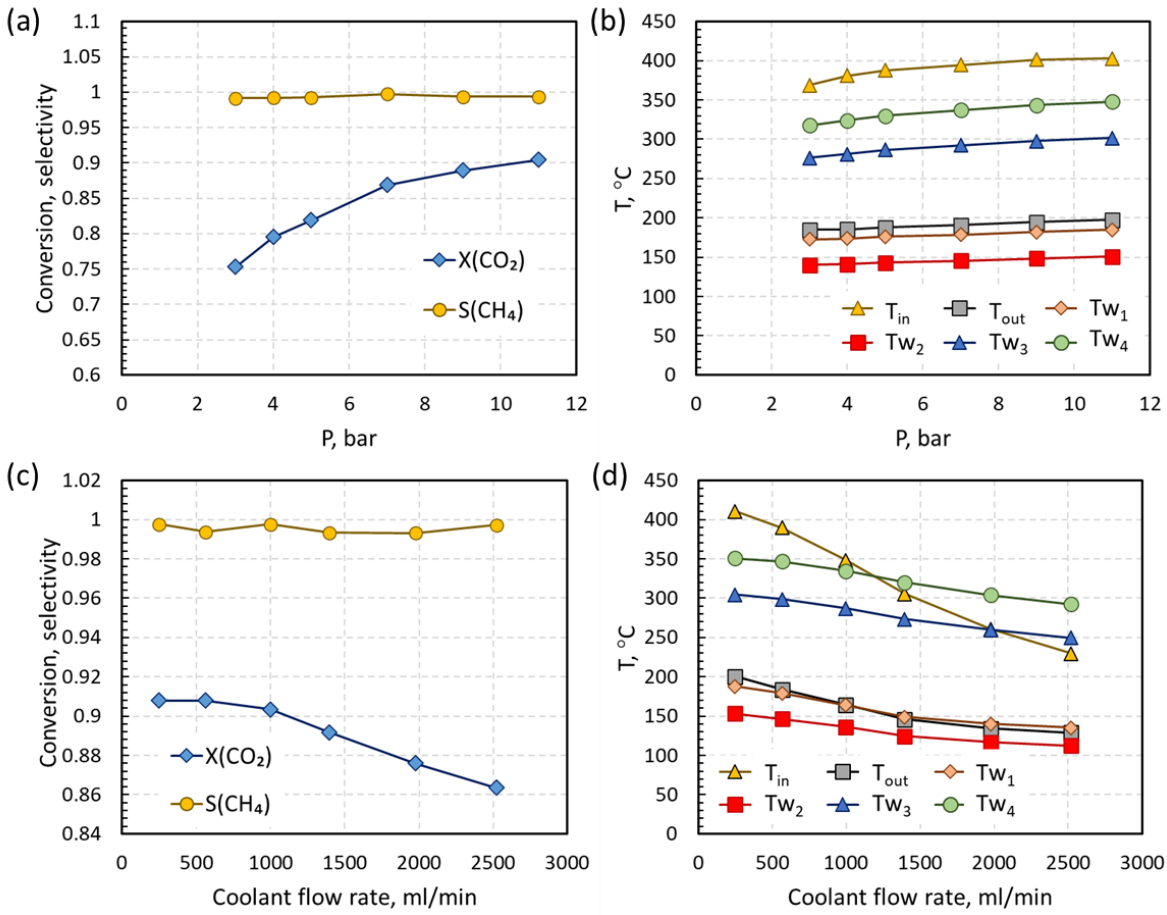

Figure 34. Reactor performance as a function of pressure and cooling flow rate. *Parameters*: No preheat, H_2:CO_2 = 4, CH_4:CO_2 = 1.43, GHSV = 11,000 L/(kg h); Q_c = 0.25 L/min (countercurrent flow) (a, b); P = 11 bar(c, d), air balance synthetic biogas feed.

Because of its larger volume and better thermal insulation, Reactor 2 was able to handle a higher feed flow rate, while generating much more heat inside. Ideally Sabatier reactors should operate under lower temperatures, reducing the extent of catalyst deactivation by coking and having higher equilibrium conversion. The effect of cooling on reactor performance is illustrated in Figure 34c,d. As the cooling rate increased from 0.25 to 2.5 L/min, the inlet temperature showed a steep drop from 400 to 220 °C, while surface and outlet temperatures slowly declined. During the test CH_4 selectivity stayed at 1 and CO_2 conversion decreased from 91 to 86%.

4.2.2.3 Reactor 3

The ignition procedure was identical to the procedure described in 3.1.3. For Reactor 3, which comprised 63 g of catalyst (1″ OD, 9″ L catalyst bed), additional thermocouples were installed, including the two thermocouples in contact with the external reactor wall (see Fig. S9 and *Appendix C* for details). Reactor ignition is shown in Figure 35. Note that the reduction time was increased due to a relatively large amount of catalyst as compared to the other two prototypes. The onset of ignition is clearly observable from the appearance of the CH_4 signal and a sharp increase of the reactor inlet temperature (T_{in}) and corresponding cooling compartment temperature (T_{C1}).

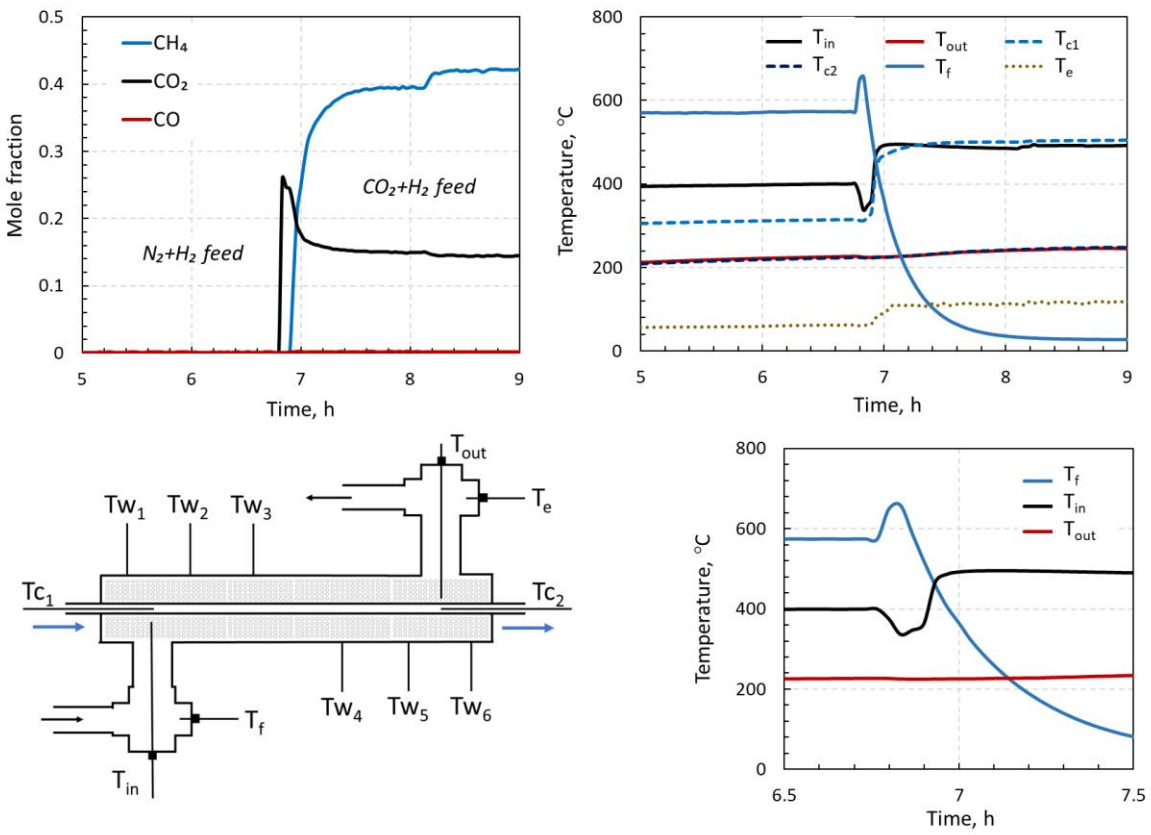

Figure 35. Reactor temperatures and outlet composition during Reactor 3 ignition. *Parameters*: H_2:CO_2 = 4, P = 1 bar, GHSV = 2,000 L/(kg h), Q_c = 0 L/min.

Figure 36 shows the effect of feed temperature on reactor performance. As the feed temperature reduced from 600 to 300 °C, inlet temperature slowly increased from 630 °C to 660 °C, followed by a 70 °C jump to 730 °C after the feed temperature reached 200 °C. Surface temperatures (T_w) and other measuring locations showed a similar trend, slowly trending upward and stabilized below 300 °C, Figure 36a,c. Figure 36b shows the axial temperature profile along the reactor, the location of the thermocouples demonstrated in Figure 36e. As shown in the figure, the temperature of the reactor increased significantly close to the inlet (at 5-inch length), and gradually decreased as the flow went further along the reactor (5-8 inches).

Right after the reactor outlet (9-inch), the temperature decreased significantly from 400 °C to 300 °C, then slowly went back. It seems most parts of the reactor stayed around 400-450 °C, which is more than enough for the Sabatier reaction. Similar to previous results, the effect of feed temperature on reactor performance was minor.

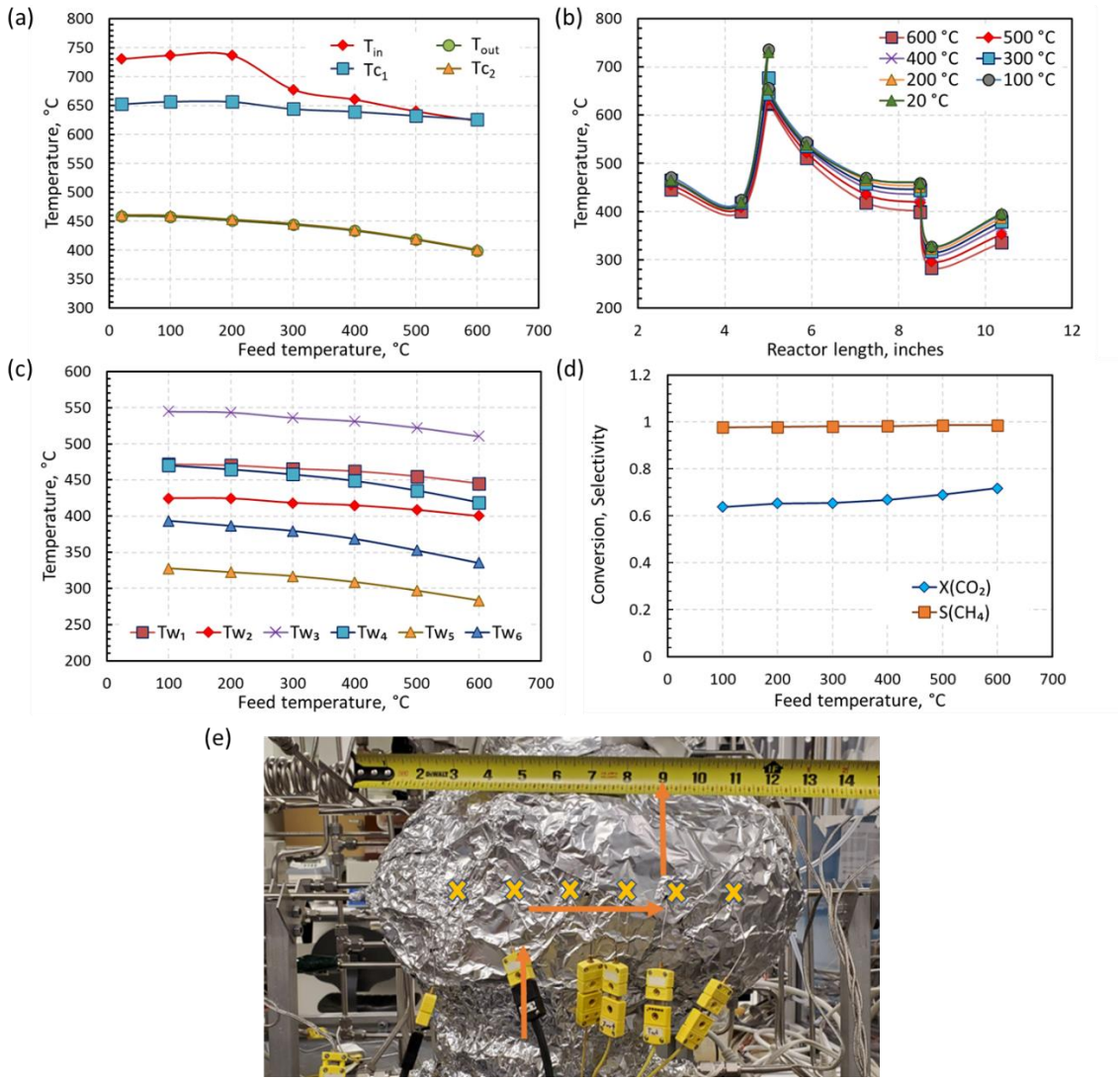

Figure 36. Reactor 3 performance as a function of feed temperature. *Parameters:* P=11 bars, GHSV= 3,100 L/(kg h), Coolant flow rate= 0 L/min, H_2:CO_2=4, CH_4:CO_2=1.43, air balance

biogas feed. Locations of the wall thermocouples illustrated in (e), arrow indicating the flow direction.

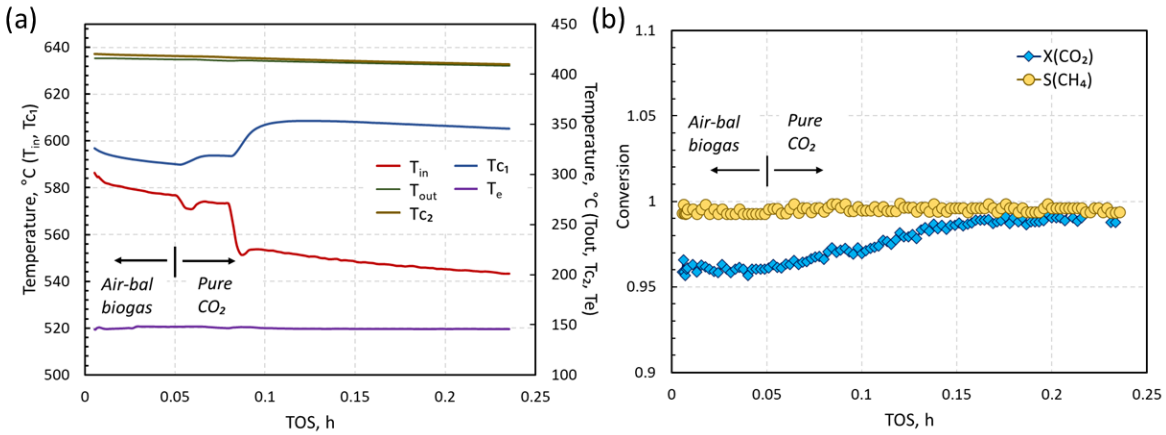

Figure 37. Temperature profile and reactor performance between pure CO_2 and air balance biogas feed. *Parameters:* No preheat, P=11 bars, H_2:CO_2=4, Coolant flow rate= 0 L/min; CH_4:CO_2=1.43, GHSV= 2,100 L/(kg h) (air balance biogas), GHSV= 1,600 L/(kg h) (pure CO_2).

To avoid frequent ignition-shutdown cycles of the reactor, the feed was switched to a low flow rate of 1:5 CO_2/H_2 mixture to keep the reactor operating and maintain reactor temperature between experiments. The temperature profile during the switching process is shown in Figure 37. Interestingly, inlet temperature had a significant drop right after the feed switch, despite almost the same amount of CO_2 and H_2 being fed to the reactor. In the meantime, CO_2 conversion went up slightly, from 96% to almost 100%. Given the existence of O_2 in the air balance synthetic biogas, a possible explanation for this phenomenon could be CH_4 or H_2 reacted with O_2, which are both highly exothermic. To examine the effect of O_2, two identical space velocity tests (air balance synthetic biogas and nitrogen balance synthetic biogas) were

conducted, and the results are shown in Figure 38. H_2 to CO_2 ratio was increased to 4.38 to account for the additional consumption of H_2 due to O_2 and improve efficiency.

It is clear that nitrogen balance biogas gave better CO_2 conversion, Figure 38. The CO_2 conversion of air balance biogas showed a linear decline as the space velocity increased, with a maximum of 88% at 3,000 L/(kg h). CO_2 conversion only dropped from 95% to 91% while GHSV increased from 3,000 to 6,500 L/(kg h) for nitrogen balance biogas feed. At the reactor outlet only 0.03% O_2 was measured by microGC, indicating that the majority of O_2 had reacted since the feed mixture originally contained 2.5% O_2, Figure 38b. This observation indicated that adding additional H_2 could improve overall conversion.

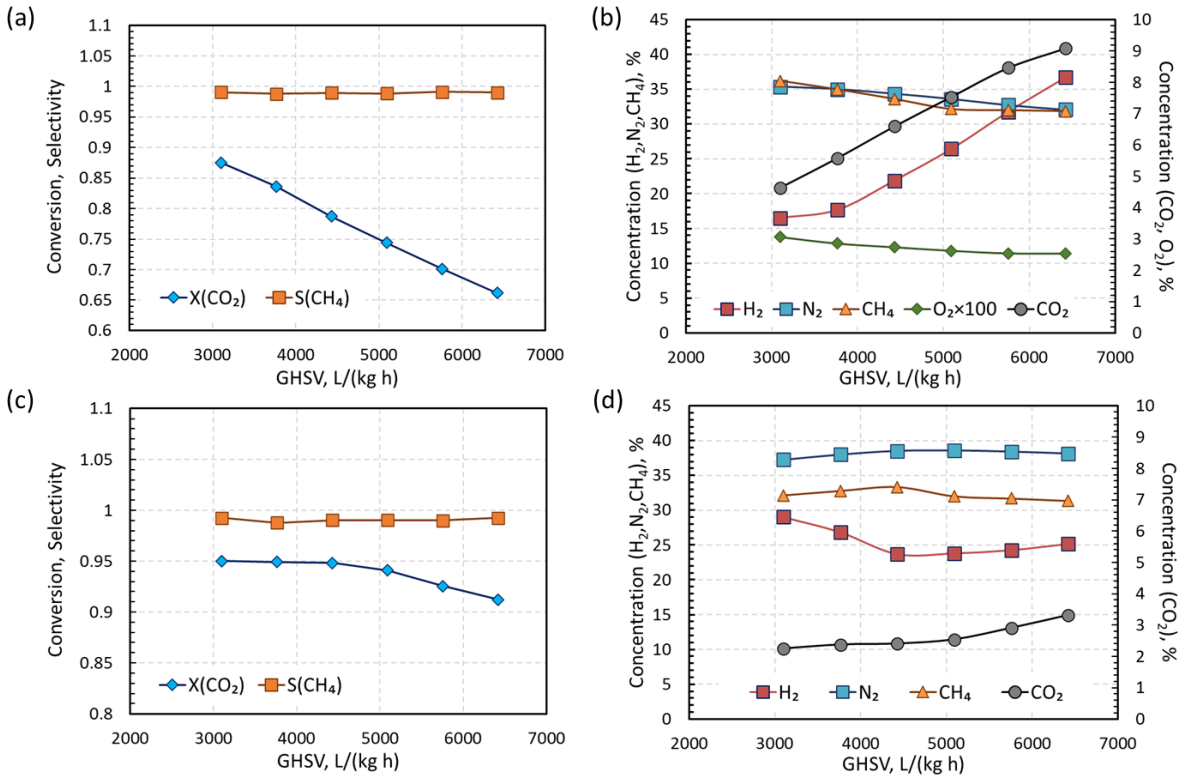

Figure 38. Effect of GHSV on Reactor 3 performance and outlet composition with air balance biogas (a, b) and nitrogen balance biogas (c, d). *Parameters:* No preheat, P=7 bars, H_2:CO_2=4.38, CH_4:CO_2=1.43, Coolant flow rate= 3-6 L/min (a, b); Coolant flow rate= 1-3 L/min (c, d).

The oxygen content in the air balance synthetic biogas also caused the inlet temperature to increase substantially compared to nitrogen balance biogas. Inlet temperature ranged from 620 °C to 670 °C for air balance biogas while for nitrogen balance biogas the range was 340 to 380 °C, Figure 39a,c. With the increase of space velocity, it is expected all temperatures gradually went up. However, inlet temperature showed a different trend when using nitrogen balance biogas as feed. It could be explained that the inert nitrogen content took away more

heat at the inlet while the heat generation was mostly inside the bed, leading to the decrease in inlet temperature. Air balance biogas showed overall higher surface temperatures (T_{W1} to T_{W6}).

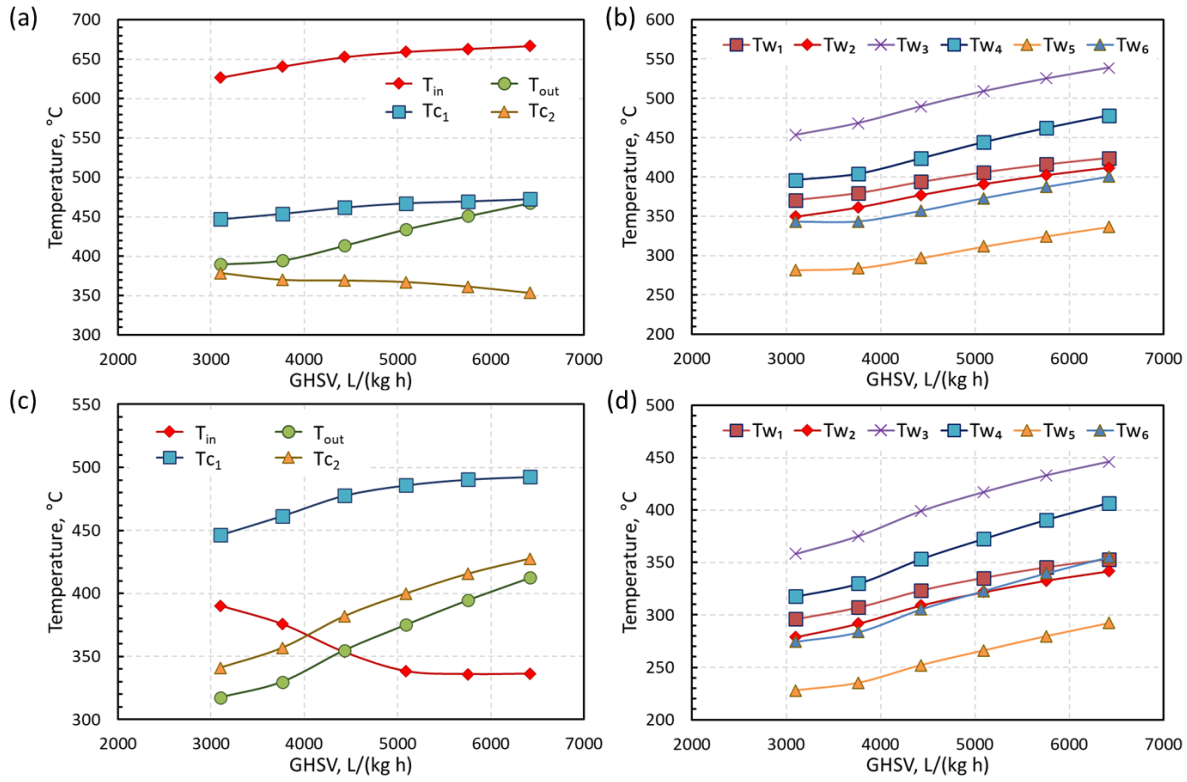

Figure 39. Effect of GHSV on Reactor 3 temperature profile with air balance biogas (a, b) and nitrogen balance biogas (c, d). *Parameters:* No preheat, P=7 bars, H_2:CO_2=4.38, CH_4:CO_2=1.43, Coolant flow rate= 3-6 L/min (a, b); Coolant flow rate= 1-3 L/min (c, d).

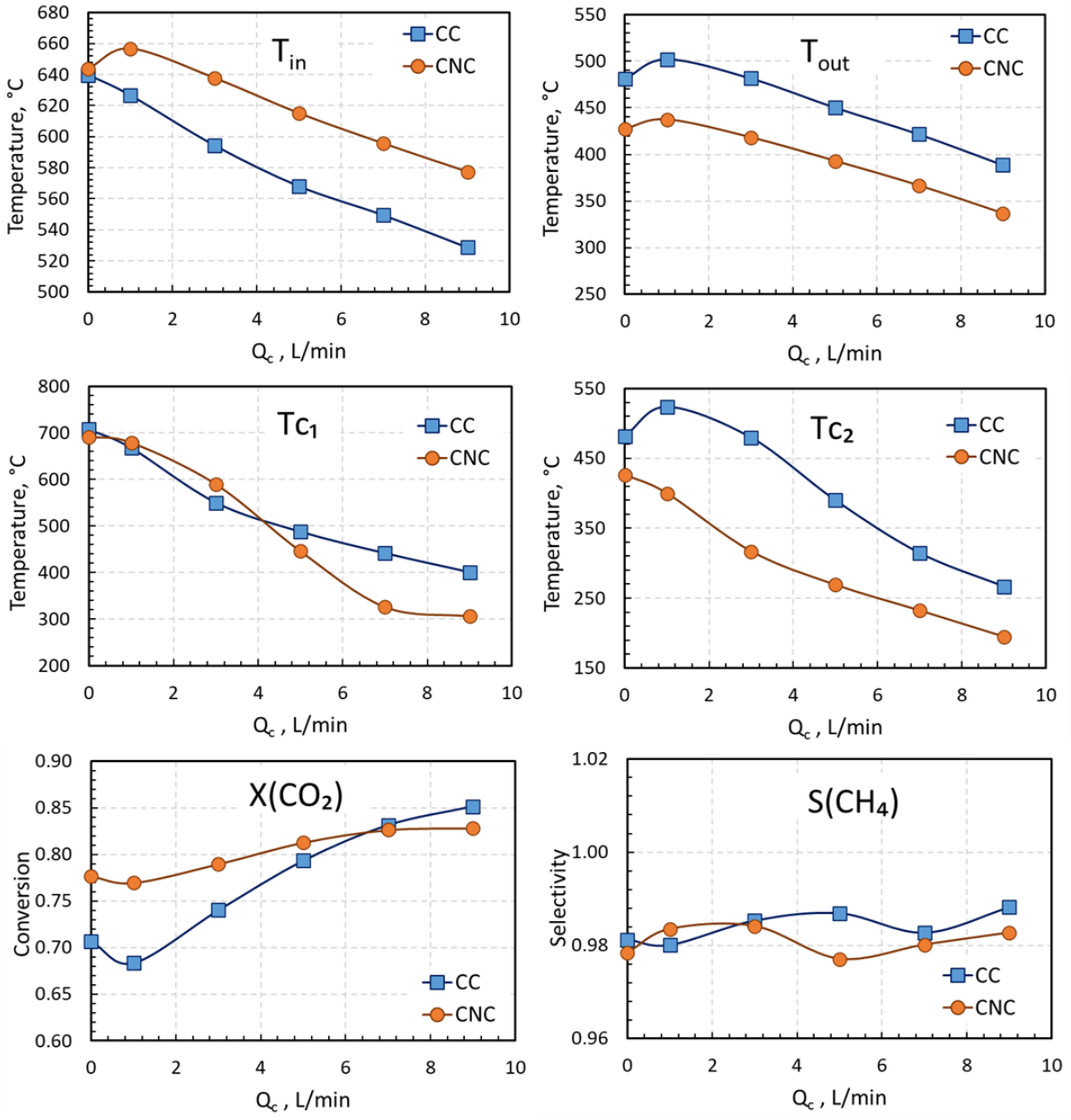

Figure 40. Effects of the cooling rate and direction (CC – cocurrent flow; CNC – countercurrent flow) on the reactor temperatures and reactor performance (in terms of conversion and selectivity). *Parameters*: P = 11 bar, H_2:CO_2 = 4.38, CH_4:CO_2=1.43, GHSV = 4,400 L/(kg h), no feed preheating, air balance biogas feed.

The effects of the cooling rate and direction are presented in Figure 40 which compares cocurrent (CC) and countercurrent (CNC) configurations in a range of the cooling flow rates. Note that the reactor was operated completely autothermally in this set of experiments, with no feed preheating (except for initial ignition). A ~ 50 °C difference can be observed for both inlet and outlet temperature, with cocurrent cooling having lower inlet temperature and countercurrent cooling resulting in lower outlet temperature. Coolant temperature next to reactor inlet (T_{C1}) does not depend significantly on the cooling direction, indicating that the temperature was likely determined by reaction heat, and the activity of Sabatier reaction was high close to the center. Depending on the cooling mode, coolant temperature at the outlet (T_{C2}) showed quite some difference between the two cooling modes under low cooling flow rate and gradually came closer as the flow rate keep going up.

Regarding the reactor performance, the CH_4 selectivity was nearly complete under all conditions for this set of experiments at around 98%. Under low cooling flow rate (0–5 L/min), countercurrent cooling mode showed 1–5% improvement in terms of CO_2 conversion. Cocurrent cooling mode was slightly better when the cooling flow rate is beyond 6 L/min, achieving 85% CO_2 conversion with 9 L/min cooling.

Figure 41 shows the stability test for Reactor 3. During the stability test the reactor was operated completely autothermally, i.e., with no feed preheating (after initial ignition). CO_2 conversion of 91% was achieved with 100% selectivity to CH_4 generation. MicroGC was used to verify CH_4 and CO_2 concentrations at 30 h and 60 h, illustrated in Figure 41c. All reactor temperatures were stable for over 100 hours. The reactor inlet temperature (T_{in}) stabilized at ca. 610 °C, with a lower corresponding coolant temperature (T_{C1}) of ca. 370 °C. Reactor wall

temperatures (T_{W1} to T_{W6}) stabilized from 240 °C to 410 °C, indicating significant heat losses through the reactor wall. Significant temperature gradient along the reactor was again observed. No substantial performance decline was observed during the test.

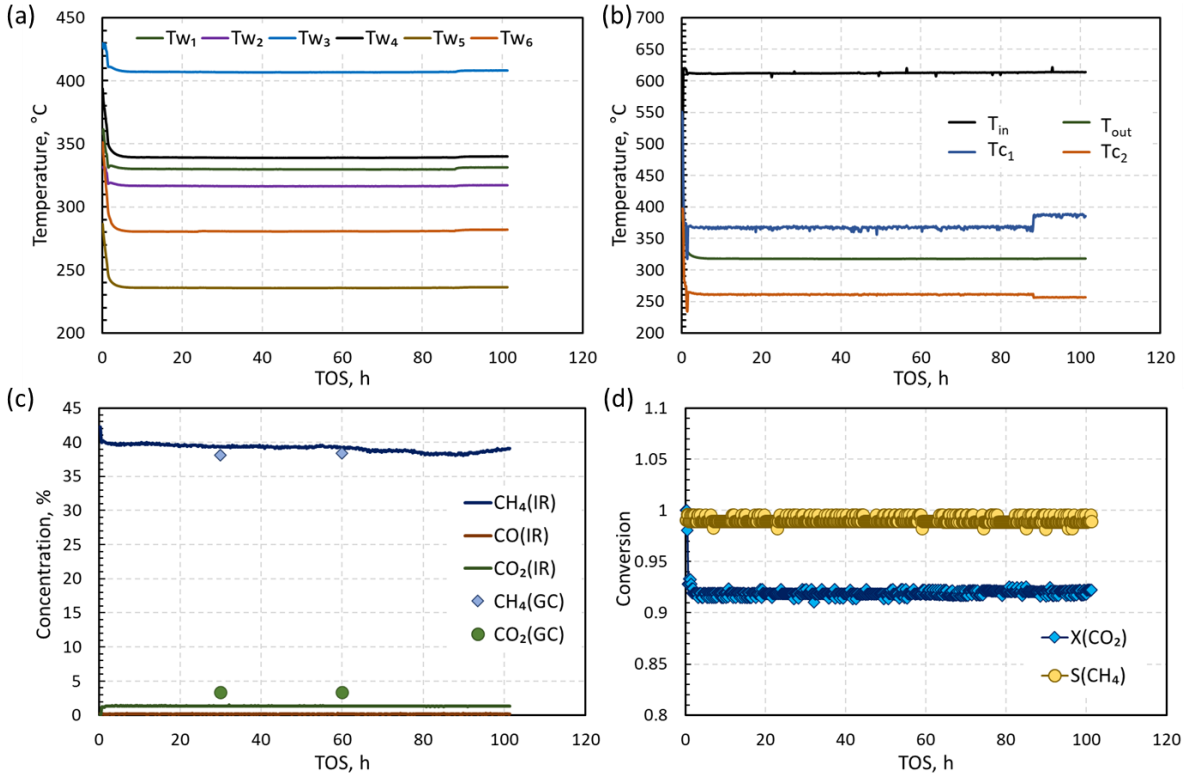

Figure 41. Reactor 3 stability test, showing the conversion, selectivity and reactor temperatures. *Parameters*: H_2:CO_2 = 4, CH_4:CO_2=1.43, GHSV = 3,100 L/(kg h), P = 11 bar, Q_c = 6 L/min (cocurrent flow), no feed preheating (after ignition), air balance biogas feed.

Chapter 5
Modeling of the Sabatier-RWGS reaction system and prototype reactor

5.1 Modeling of the Sabatier-RWGS reaction system

5.1.1 Kinetic model

Rate expressions are essential to predict the catalytic performance over a wide range of operating conditions and assess potential practical uses, also a fundamental part of developing a reactor model. If it is assumed that the Sabatier-RWGS reaction system over the commercial Ni/Al_2O_3 catalyst follows a similar reaction mechanism as the one suggested by Lalinde [82], rate equations can be written as follows:

$$r_{CH_4} = \frac{k_1 K_{COH}\, p_{CO_2}^{0.5} K_{H_2}\, p_{H_2} \left(1 - \left(\frac{p_{H_2O}^2\, p_{CH_4}}{p_{H_2}^4\, p_{CO_2} K_{eq,SR}}\right)\right)}{DEN^2} \tag{14}$$

$$r_{RWGS} = \frac{k_2\, p_{CO_2} K_{H_2}^{0.5} p_{H_2}^{0.5} \left(1 - \left(k_\beta \frac{p_{CO}\, p_{H_2O}}{p_{H_2}\, p_{CO_2} K_{eqRWGS}}\right)\right)}{DEN^2} \tag{15}$$

$$DEN = 1 + K_{COH}\, p_{CO_2}^{0.5} K_{H_2}^{0.5} p_{H_2}^{0.5} + \sqrt{K_{H_2} p_{H_2}} + K_{COH} \frac{p_{H_2O}}{\sqrt{p_{H_2}}} \tag{16}$$

$$\begin{aligned} R_{H_2} &= -4 r_{CH_4} - r_{RWGS} \\ R_{CO} &= r_{RWGS} \\ R_{CO_2} &= -r_{CH_4} - r_{RWGS} \\ R_{CH_4} &= r_{CH_4} \\ R_{H_2O} &= 2 r_{CH_4} + r_{RWGS} \end{aligned} \tag{17}$$

Reaction rate and adsorption constants are given by the following equations:

$$k_i = k_{ref,i} \exp\left(\frac{E_{a,i}}{R}\left(\frac{1}{T_{ref}} - \frac{1}{T}\right)\right), T_{ref} = 613.15K \quad (18)$$

$$K_i = K_{ref,i} \exp\left(\frac{\Delta H_j}{R}\left(\frac{1}{T_{ref}} - \frac{1}{T}\right)\right), T_{ref} = 613.15K \quad (19)$$

Equilibrium constants of Sabatier reaction and RWGS shown below in Eqs. (20-21) [83, 84]:

$$K_{eq,SR} = e^{\left[\left(\frac{1}{1.987}\right)\left(56000/T^2 + 34633/T - 16.4\ln(T) + 0.00557T\right) + 33.165\right]} \quad (20)$$

$$K_{eq,RWGS} = 9.01\times10^{-6} T^{0.968} \exp\left(\frac{43.6kJ/mol}{R_g T}\right) \quad (21)$$

5.1.2 Kinetic parameter estimation

To estimate the total 12 parameters (shown in Table 4) a set of lab experiments to monitor change in species concentrations as a function of temperature and space velocity was carried out. CO_2 and H_2 were fed by mass flow controllers to a lab-scale flow reactor containing ~0.2g of catalyst with the outlet concentrations continuously monitored and recorded by an IR analyzer. The absence of mass and heat transfer limitations in the kinetic reactor was verified by corresponding analytical criteria (see *Appendix G*).

Table 4. Estimated kinetic parameters for commercial Ni/Al_2O_3 catalyst.

k_1	Ea_1	k_2	Ea_2	K_{COH}	ΔH_{COH}
K_{H_2}	ΔH_{H_2}	K_{OH}	ΔH_{OH}	K_β	ΔH_β

Parameter estimation was done using the minimization of the sum of weighted residual squares of the CO_2, CO and CH_4 concentrations employing the Trust-Region Reflective Algorithm [85]. Simulated mole fractions were obtained by integrating a set of ordinary differential equations described by Eq. 22 representing time evolution of all species participating in the Sabatier-RWGS reaction system, i.e., CO_2, H_2, CO, CH_4 and H_2O:

$$\varepsilon \frac{dC_i}{dt} = -\frac{\varepsilon Q_f (C_i - C_{if})}{V_r} + (1-\varepsilon)\rho_s \alpha_i R_{i,j} \tag{22}$$

In Eq. 23, c_i is molar concentration for species i, ε is void fraction, Q_f is volumetric flow rate, V_r is reactor volume, ρ_s is catalyst density, and α_i is stoichiometric coefficient of species i. Initial guesses for adsorption constants (Eq. 19) were adopted from Lalinde [82].

To simply the model and reduce the computational time, the adsorption term (denominator, DEN) was first assumed to be equal to 1:

$$DEN = 1 \tag{23}$$

The simulation results and experimental data in terms of CO_2, CO and CH_4 concentrations and CO_2 conversion as a function of temperature are shown in Figure 42. The simulation results are quite similar under all three space velocities, and the model fits well under 400 °C. The trend of the simulation was not able to fit experimental data well above 450 °C.

Since almost no CO formation was observed in all experiments, the RWGS reaction likely had little effect on the overall results within the tested operating conditions. The reaction rate of the RWGS reaction was subsequently set to 0 to examine the possibility to simplify the model by removing the RWGS expression from the model. The simulation results are shown

in Figure 43. Compared to previous results, no significant change was found after the removal of the RWGS reaction from the kinetic model.

However after the removal of the RWGS rate, the model was still not able to fit experimental data well. One of the possible causes is the absorption of the reactants and intermediates play an important role in the reaction model. After taking into consideration the effect of adsorption, the simulation results are shown in Figure 44. With the addition of adsorption, the model simulation showed notable improvements, especially the trend above 450 °C compared to the previous results. The finalized kinetic model is adopted in the COMSOL model later to model prototype Reactor 3.

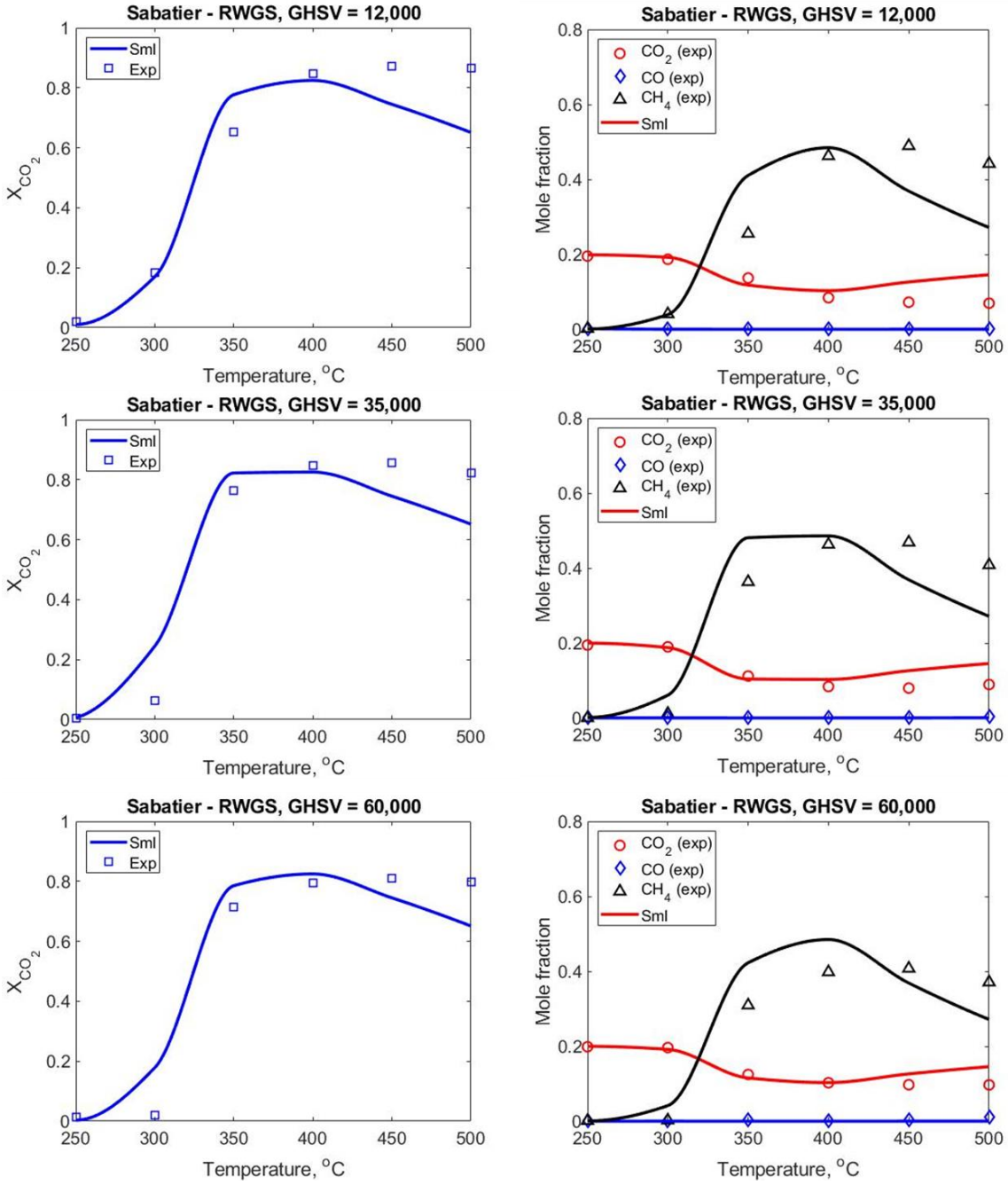

Figure 42. The simulation results vs. experimental in terms of species concentrations and CO_2 conversion as a function of temperature (DEN=1). *Experimental conditions:* H_2:CO_2 = 4, P = 3 bar, 0.24g commercial Ni/Al_2O_3 catalyst, data collected using kinetic reactor.

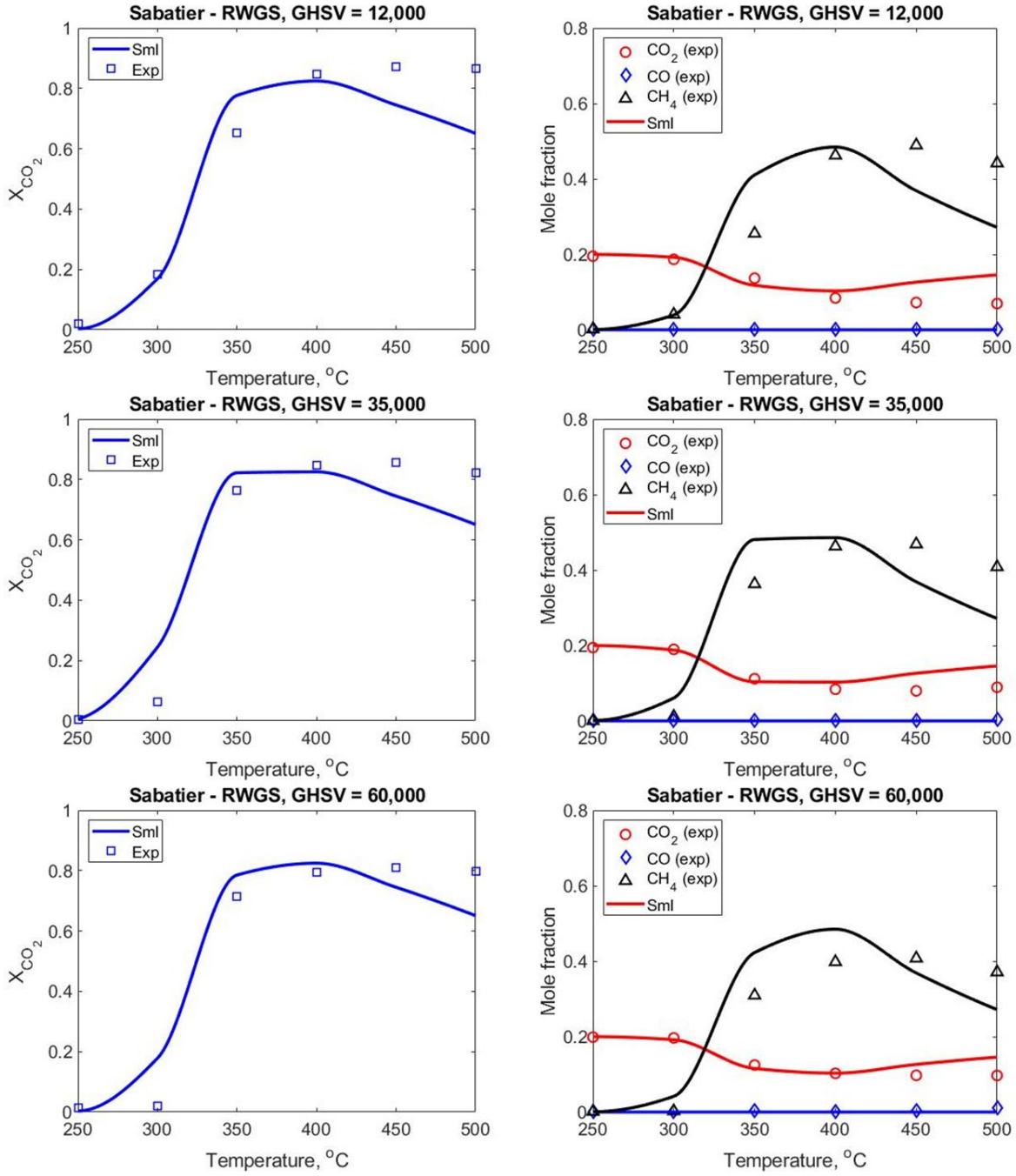

Figure 43. The simulation results vs. experimental in terms of species concentrations and CO_2 conversion as a function of temperature (DEN=1, r_{RWGS}=0). *Experimental conditions:* H_2:CO_2 = 4, P = 3 bar, 0.24g commercial Ni/Al_2O_3 catalyst, data collected using kinetic reactor.

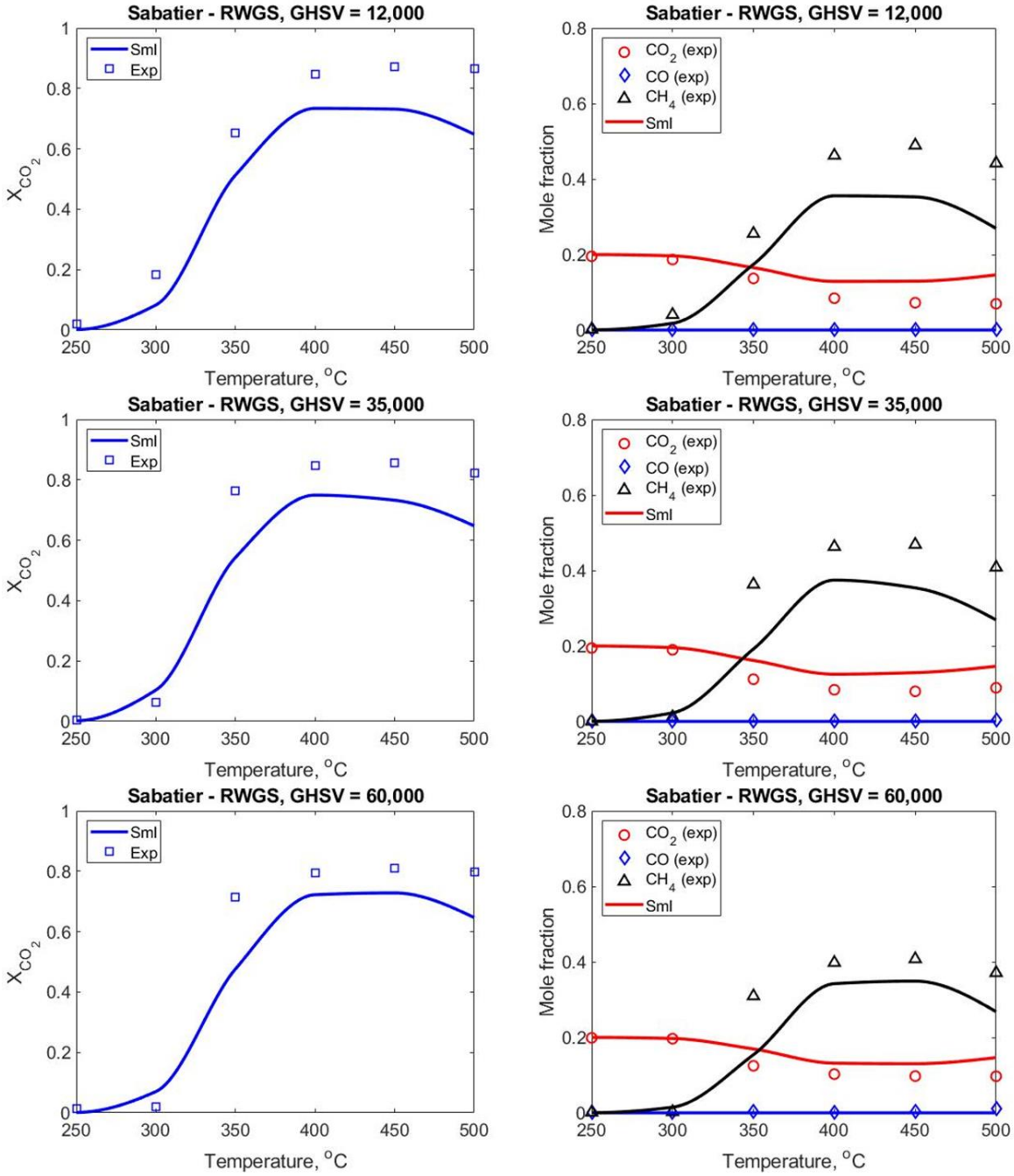

Figure 44. The simulation results vs. experimental in terms of species concentrations and CO_2 conversion as a function of temperature (r_{RWGS}=0). *Experimental conditions:* H_2:CO_2 = 4, P = 3 bar, 0.24g commercial Ni/Al_2O_3 catalyst, data collected using kinetic reactor.

5.2 COMSOL reactor model

5.2.1 Model equations

A 2D pseudo-homogeneous model was developed accounting for axial and radial gradients based on the geometry of prototype Reactor 3, all details of Reactor 3 are provided in *Appendix B* (see Figs S5), the configuration and diagram of the modeled reactor are shown in Figure 45 and Figure 46.

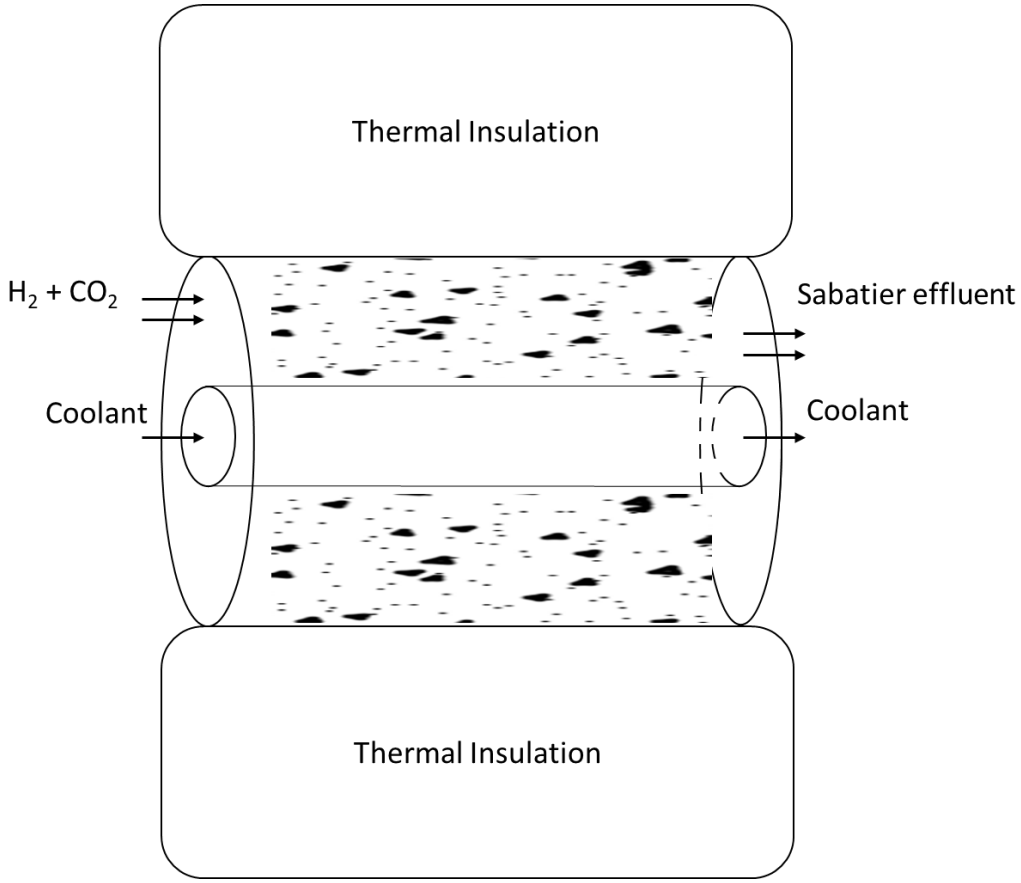

Figure 45. Structure of Reactor 3.

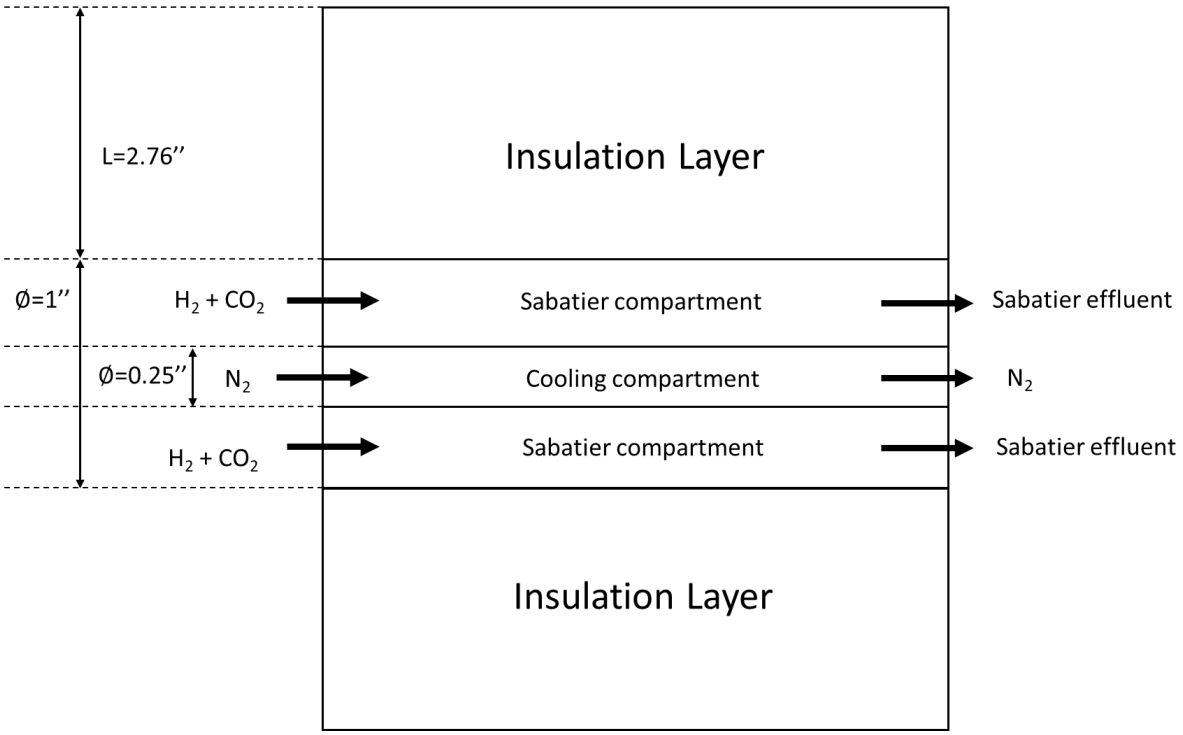

Figure 46. 2D reactor schematic. Dimensions taken from Reactor 3, all details are provided in *Appendix B* (see Figs S5).

Mass balance and energy balance inside the Sabatier and cooling compartment are calculated by Eqs. (24-27). Inside the insulation layer, since there is no reaction and mass transfer, only energy balance is accounted for, shown in Eq. (28). Eq. (29) shows the initial conditions for the model. Radial and axial boundary conditions are listed in Eqs. (30-31). Notation is explained in *Nomenclature*.

$$\left(\varepsilon\rho_g\right)^{SR}\frac{\partial y_i^{SR}}{\partial t}=\left(\rho_g D_{re}\right)^{SR}\frac{\partial^2 y_i^{SR}}{\partial r^2}+\left(\rho_g D_{ae}\right)^{SR}\frac{\partial^2 y_i^{SR}}{\partial z^2}+\frac{1}{r}\left(\rho_g D_{re}\right)^{SR}\frac{\partial y_i^{SR}}{\partial r}$$
$$-\left(\varepsilon v_g \rho_g\right)^{SR}\frac{\partial y_i^{SR}}{\partial z}+\left(1\text{-}\varepsilon^{SR}\right)\rho_s^{SR}\alpha_i R_j \qquad (24)$$

$$\left(\rho C_p\right)_{eff}^{SR}\frac{\partial T^{SR}}{\partial t}=k_{re}^{SR}\frac{\partial^2 T^{SR}}{\partial r^2}+k_{ae}^{SR}\frac{\partial^2 T^{SR}}{\partial z^2}+\frac{k_{re}^{SR}}{r}\frac{\partial T^{SR}}{\partial r}-\left(\varepsilon v_g\rho_g C_{pg}\right)^{SR}\frac{\partial T^{SR}}{\partial z}+\left(1\text{-}\varepsilon^{SR}\right)\rho_s^{SR}\left(-\Delta H_j\right)R_j \tag{25}$$

$$\left(\varepsilon\rho_g\right)^{SR}\frac{\partial y_i^{SR}}{\partial t}=\left(\rho_g D_{re}\right)^{SR}\frac{\partial^2 y_i^{SR}}{\partial r^2}+\left(\rho_g D_{ae}\right)^{SR}\frac{\partial^2 y_i^{SR}}{\partial z^2}+\frac{1}{r}\left(\rho_g D_{re}\right)^{SR}\frac{\partial y_i^{SR}}{\partial r}-\left(\varepsilon v_g\rho_g\right)^{SR}\frac{\partial y_i^{SR}}{\partial z} \tag{26}$$

$$\left(\rho C_p\right)_{eff}^{c}\frac{\partial T^{c}}{\partial t}=k_{re}^{c}\frac{\partial^2 T^{c}}{\partial r^2}+k_{ae}^{c}\frac{\partial^2 T^{c}}{\partial z^2}+\frac{k_{re}^{c}}{r}\frac{\partial T^{c}}{\partial r}-\left(\varepsilon v_g\rho_g C_{pg}\right)^{c}\frac{\partial T^{c}}{\partial z} \tag{27}$$

$$k_{ins}\frac{1}{r}\left(\frac{\partial T^{ins}}{\partial r}+r\frac{\partial^2 T^{ins}}{\partial r^2}\right)+k_{ins}\frac{\partial^2 T^{ins}}{\partial z^2}=0 \tag{28}$$

$$t=0:\quad y_i^{SR}=y_{i0}^{SR},T^{SR}=T_0^{SR};\ y_i^{c}=y_{i0}^{c},T^{c}=T_0^{c};T^{ins}=T_0^{ins} \tag{29}$$

Radial boundary conditions

$$\begin{aligned}
&r=0,\ 0\le z\le L:\quad \frac{\partial T^{c}}{\partial r}=0\\
&r=R_c,\ 0\le z\le L:\quad -k_{re}^{c}\frac{\partial T^{c}}{\partial r}=U_{w,HE}\left(T^{SR}-T^{c}\right)\\
&r=R_{SR},\ 0\le z\le L:\quad -k_{re}^{SR}\frac{\partial T^{SR}}{\partial r}=U_{w,HL}\left(T^{SR}-T_{ins}\right)\\
&r=R_{ins},\ 0\le z\le L:\quad -k_{re}^{ins}\frac{\partial T^{ins}}{\partial r}=U_{w,HL}\left(T_{ins}-T_a\right)
\end{aligned} \tag{30}$$

Axial boundary conditions

$$
\begin{aligned}
&z=0,\ 0\le r\le R_c: \quad \left(v_g\rho_g C_{pg}\right)^c\left(T_f^c-T^c\right)=-k_{ae}^c\frac{\partial T^c}{\partial z}\\
&z=0,\ R_c\le r\le R_{SR}: \quad \left(\varepsilon v_g\right)^{SR}\left(y_{if}^{SR}-y_i^{SR}\right)=-D_{ae}^{SR}\frac{\partial y_i^{SR}}{\partial z}\\
&\qquad\qquad \left(\varepsilon v_g\rho_g C_{pg}\right)^{SR}\left(T_f^{SR}-T^{SR}\right)=-k_{ae}^{SR}\frac{\partial T^{SR}}{\partial z} \qquad (31)\\
&z=L,\ 0\le r\le R_c: \quad \frac{\partial T^c}{\partial z}=0\\
&z=L,\ R_c\le r\le R_{SR}: \quad \frac{\partial y_i^{SR}}{\partial z}=0,\ \frac{\partial T^{SR}}{\partial z}=0
\end{aligned}
$$

The same Sabatier-RWGS reaction kinetic model expressions and parameters are taken from Chapter 5.1.1 and adopted in the COMSOL model to calculate reaction rate. The estimated parameters are shown in Table 5. Table 6 lists the operating conditions of the reactor modeled in COMSOL. The operating conditions correspond to the stability test of Reactor 3, described in Chapter 3.2.2.4 (Figure 27).

Table 5. List of estimated kinetic parameters.

Parameter	Value	Units
k_1	1.165	mol $kgcat^{-1}$ $bar^{-0.5}$
Ea_1	117.57	kJ mol^{-1}
k_2	0.968	mol $kgcat^{-1}$ bar^{-1}
Ea_2	195.17	kJ mol^{-1}
K_{COH}	3.947	$bar^{-0.5}$
ΔH_{COH}	89.23	kJ mol^{-1}
K_{H_2}	0.286	bar
ΔH_{H_2}	-6.706	kJ mol^{-1}
K_{OH}	1.73	bar^{-1}
ΔH_{OH}	64.4	kJ mol^{-1}
K_β	118.9	-

ΔH_β	-19.67	kJ mol^{-1}

Table 6. Reactor model operating conditions.

Parameter	Symbol	Value	Units
Cooling compartment pressure	P_c	1	bar
SR compartment pressure	P_{SR}	15	bar
Cooling compartment feed temperature	$T_{f,c}$	25	℃
SR compartment feed temperature	$T_{f,SR}$	50	℃
Cooling compartment initial temperature	$T_{0,c}$	25	℃
SR compartment initial temperature	$T_{0,SR}$	300	℃
Ambient temperature	T_a	25	℃
SR compartment feed composition	H_2:CO_2	4	-
Cooling compartment flow rate	$Q_{f,c}$	2	L/min
SR compartment GHSV	$GHSV_{SR}$	2,400	L/(kg h)

5.2.2 Simulation results

Figure 47 shows the mole fraction of all species in the Sabatier compartment along reactor length (dimensionless) after reaching steady-state. At the front of the reactor, 10% of CH_4 is observed, indicating significant reaction activity at the inlet. H_2 and CO_2 concentrations gradually go down as the mole fraction of CH_4 and water increase. Modeling results suggest 18% CH_4 and 2% CO_2 exit the reactor, leading to a 90% CO_2 conversion. At the center of the cooling compartment, the temperature dramatically goes up from 25 °C to 400 °C, Figure 48.

The temperature in both Sabatier compartment and insulation layer slowly decrease along the reactor. As mentioned above, the operating conditions of the model are taken from the stability test of Reactor 3, Chapter 3.2.2.4. Inlet and outlet temperatures in the experimental study were 500 °C and 300 °C respectively, which are ~70 °C less than the model predictions. Wall temperature followed a similar trend as the model results suggest. Note that the CO_2 conversion also does not deviate much from experimental data, which was 93%.

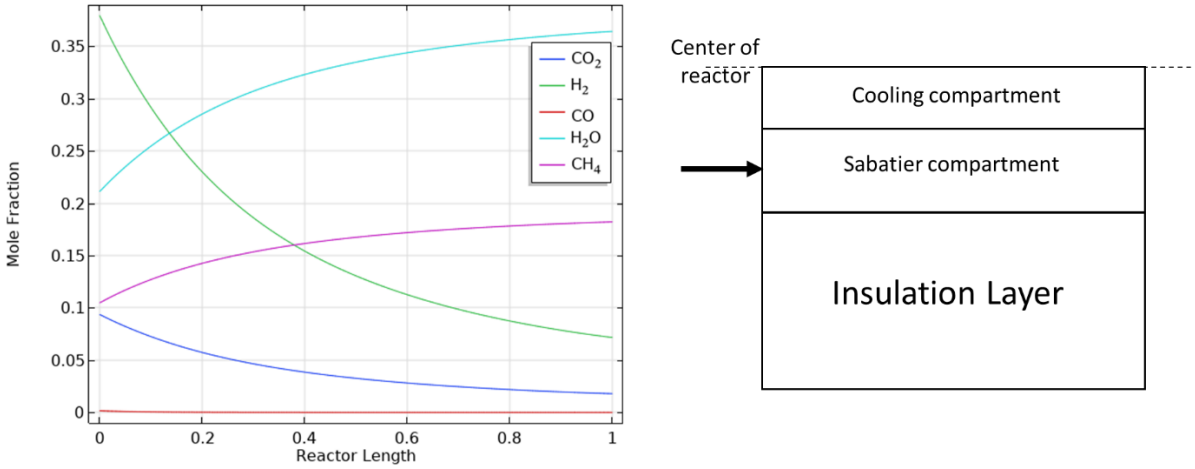

Figure 47. Mole fraction of CO_2, H_2, CO, H_2O and CH_4 at the center of Sabatier compartment. *Parameters:* P=15 bar, GHSV=2,400 L/(kg h), H_2:CO_2=4, Q_c=2L/min (cocurrent flow).

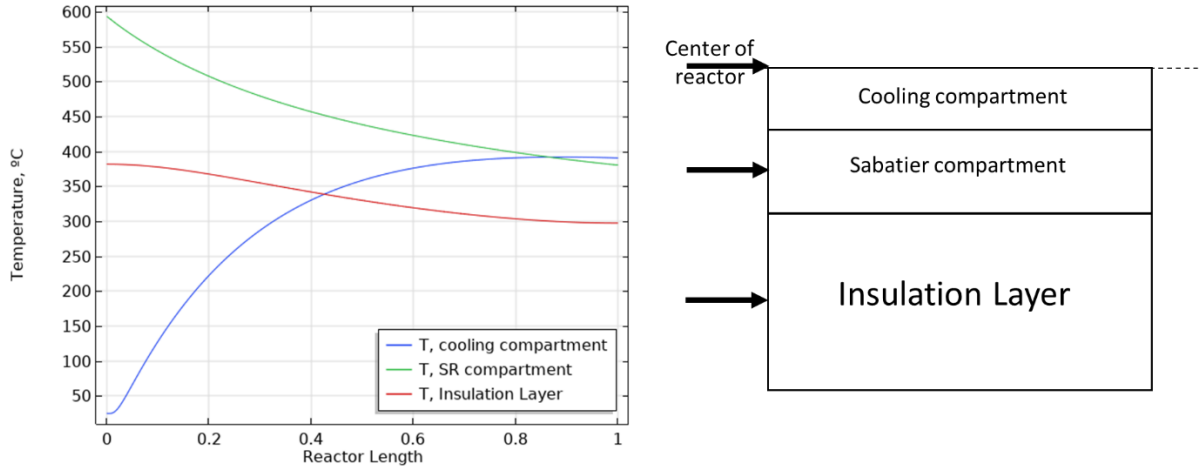

Figure 48. Temperature profile in the middle of cooling compartment, Sabatier compartment and insulation layer. *Parameters:* P=15 bar, GHSV=2,400 L/(kg h), H_2:CO_2=4, Q_c=2L/min (cocurrent flow).

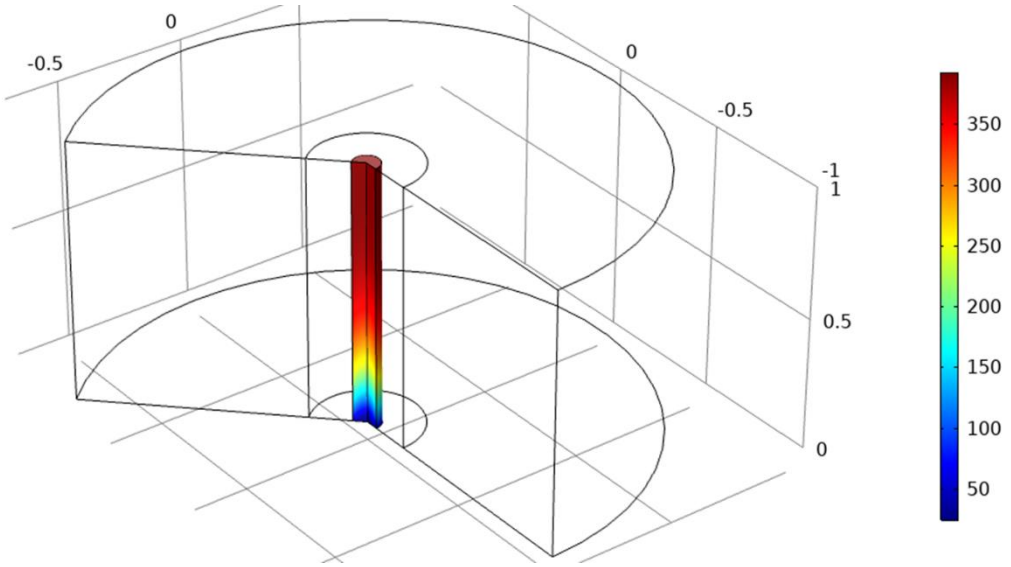

Figure 49. Axial and radial temperature distribution of cooling compartment. *Parameters:* P=15 bar, GHSV=2,400 L/(kg h), H_2:CO_2=4, Q_c=2L/min (cocurrent flow).

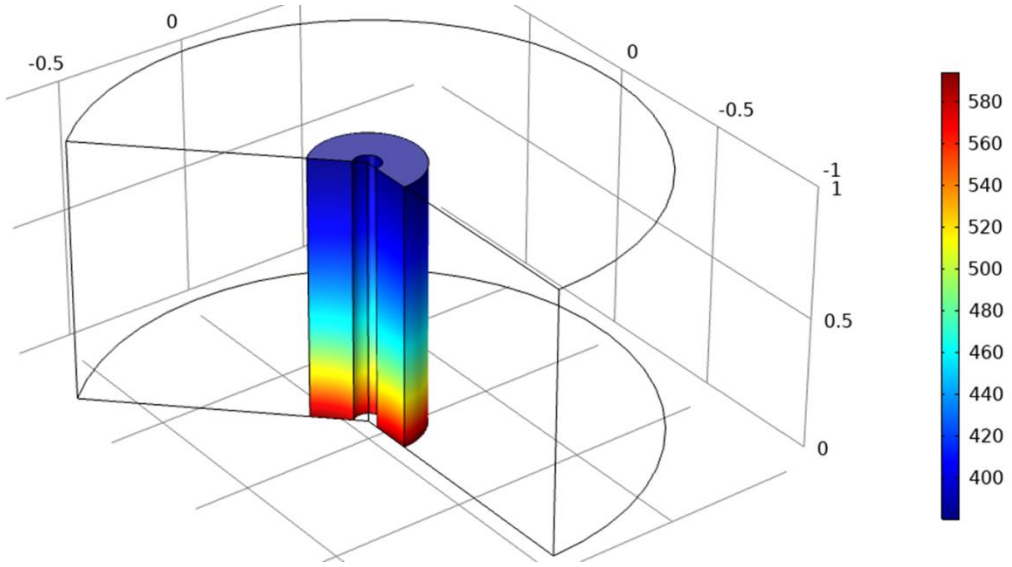

Figure 50. Spatial profile of temperature at the middle of Sabatier compartment. *Parameters:* P=15 bar, GHSV=2,400 L/(kg h), H_2:CO_2=4, Q_c=2L/min (cocurrent flow).

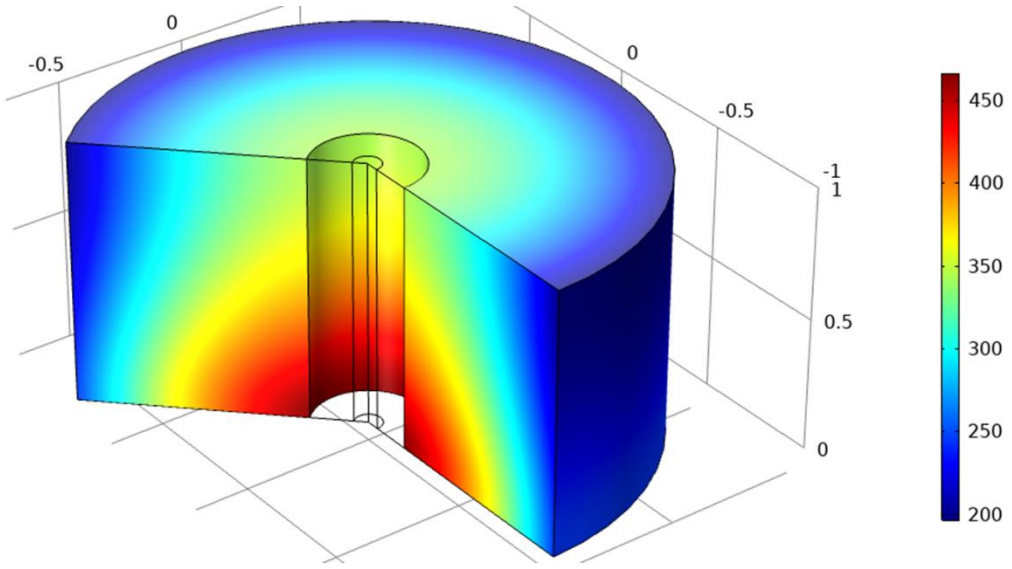

Figure 51. Insulation layer temperature distribution. *Parameters:* P=15 bar, GHSV=2,400 L/(kg h), H_2:CO_2=4, Q_c=2L/min (cocurrent flow).

Figure 49, Figure 50 and Figure 51 demonstrate both the axial and radial temperature profile in the cooling compartment, Sabatier compartment and insulation layer. It is expected

that the highest reactor temperature located at the beginning of the reactor, and the reactor slowly cools down as the reactants flow through the bed. The same phenomena have also been observed during the experimental studies, as the inlet always showed the highest temperature among all measured locations. It is also demonstrated that the surface of the reactor reaches a surprising 200 °C, indicating the possibility to recover and utilize the excess heat.

In summary, it is concluded that the model describes the reactor reasonably well within the operating conditions. It shows the significance of thermal management and could be beneficial in the future scale-up of the reactor as well as optimization of operating conditions.

Chapter 6
Conclusion

6.1 CO_2 methanation

An N_2-cooled Sabatier reactor was investigated, examining the effects of feed temperature, space velocity, pressure and cooling rate on the reactor performance in terms of CO_2 conversion and selectivity to CH_4 generation. The stainless steel, tube-and-shell reactor comprised a commercial Ni/Al_2O_3 catalyst in the shell compartment, with the inner tube being used for active cooling. The reactor stability was investigated as well. The maximum CO_2 conversion of 93.5% with 100% selectivity to CH_4 generation was achieved at 2,400 L/(kg h) and 14 bar in the 1″ diameter, 10″ length reactor operated autothermally (without feed preheating), over 120 h of a continuous, stable operation with average bed temperature at ~400 °C.

Three different prototypes were investigated, gradually increasing the reactor size (3.5″, 5″ and 9″ length of the active bed) and thus the catalyst amount. All prototypes were operated without electrical heating of the reactor, with the feed being preheated in certain experiments and supplied at room temperature in other experiments. It has been demonstrated that the reactors can be operated autothermally after the initial preheating for ignition. After ignition, the reactors were operated partially (with certain feed preheating) or completely (room temperature feed) autothermally. For all three prototypes, the reactor operation was robust to the change in operating conditions (feed temperature, space velocity, pressure and cooling

rate). In all experiments, the CO_2 conversion was in 80-94% range with the selectivity to CH_4 generation of 99-100%.

At 93.5% CO_2 conversion the compositions at the outlet of the reactor are 73.7% CH_4, 5.1 % CO_2 and 21.2% H_2 after the removal of water. Equilibrium data suggests that the reaction is limited by thermodynamic equilibrium with an average bed temperature of 400 °C [32]. Similar CO_2 methanation pilot plants from the literature reported running at 250-500 °C under 5-30 bars using multiple stages, with the final product reaching as high as 97% CH_4 [32, 58, 86]. The single stage conversion in of the pilot plants adopting a fluidized bed reactor was around 91% at 300 °C, with the second stage increasing to 98% under 350 °C [87]. Another study pointed out that bed temperature appears to be the most influential parameter, achieving 95.4-98.2% conversion in the temperature range of 280-350 °C [88], which is quite low compared to this study.

Our findings provide important insights into the operation of lab-scale Sabatier reactors. Due to the simplicity of assembly, such laboratory reactors are very useful for investigating the effects of various operating parameters on reactor performance. Another important aspect is reactor stability, which can be investigated at low cost using a small-scale, laboratory Sabatier reactor. Interestingly, a commercial reforming catalyst provided an excellent performance (maximum 94% CO_2 conversion with 100% selectivity to CH_4 formation). The results of our investigation can be also used as a calibration set of data for building a reliable mathematical model of the Sabatier reactor, which can be further scaled up via numerical simulations.

6.2 Direct biogas upgrade

Similar to the previous section, the performance of the same N_2-cooled Sabatier reactor had been studied and the effect of operating parameters including feed temperature, space velocity and cooling flow rate had been investigated. Compared to the previous section, this study focused on upgrading biogas directly instead of feeding pure CO_2. The performance of commercial Ni/Al_2O_3 catalyst on raw biogas was assessed. Air balance synthetic biogas was found to be an excellent substitute for treated biogas (after H_2S and VOC removal) for reactor testing. All reactor prototypes were demonstrated to be able to operate autothermally using air balance synthetic biogas as feed, which has not been mentioned in the literature so far. The final prototype achieved a 91% CO_2 conversion while maintaining complete selectivity to CH_4 for over 100 hours at 3,100 L/(kg h) with stable reactor temperatures.

Compared to previous reported successful direct upgrade tests, the yield of CH_4 was as high as 91%, which is comparable to direct upgrade project utilizing fluidized bed reactor design reaching 96% [79]. The CH_4 concentration after the main reactor ranges from 73% to 95% [89, 90] which is much higher than what this project presented at ~40%. This is mainly because of the large quantities of N_2 and O_2 content in the synthetic biogas feed, and the feed stream in other studies generally only contains CH_4 and CO_2. The final prototype runs slightly hotter (330-700 °C) than other fixed bed upgrade reactors (250-680 °C), which used thermal oil and boiling water as coolant) [89, 91]. It was also reported that minor catalyst deactivation was observed after 400 hours of continuous operation [79], while some projects added steam to the reactor to inhibit coke formation. Stability after 400-500 hours need to be examined in the future. This study provides another perspective on biogas utilization. The collected data

from this study can also be used to calibrate a reactor model, which could be used for further scale-up.

6.3 Reactor modeling

Kinetic model of the Sabatier-RWGS reaction system was selected from literature and 12 kinetic parameters were estimated using experimental data obtained with the commercial Ni/Al_2O_3 catalyst. Simulation results adopting estimated parameters indicated little effect on the RWGS reaction within the examined temperature range while the adsorption affects the modeling results significantly. COMSOL model based on the geometry of Reactor 3 had been developed and it is shown that the experimental data was described well with minor deviation.

The model can be used to extrapolate to a variety of operating conditions to examine the potential optimization of the reactor performance. Future work will include model improvement, assessing the reactor performance over a wide range of industrially relevant operating conditions (space velocity, pressure, cooling flow rate), optimizing reactor dimensions and configurations, as well as further scaling up.

Bibliography

[1] M.o.E.a.C. Change, National Inventory Report 1990–2019: Greenhouse gas sources and sinks in Canada., in: E.a.C.C. Canada (Ed.)Gatineau, 2021.
[2] M. Aresta, A. Dibenedetto, Utilisation of CO_2 as a chemical feedstock: opportunities and challenges, Dalton T., (2007) 2975-2992.
[3] M. Eco-Network, CO_2 equivalents, 2016.
[4] M.J. Tuinier, M. vanSintAnnaland, Biogas purification using cryogenic packedbed technology, Ind. Eng. Chem. Res., 51 (2012) 5552-5558.
[5] H.-C. Shin, J.-W. Park, H.-S. Kim, E.-S.J.E.p. Shin, Environmental and economic assessment of landfill gas electricity generation in Korea using LEAP model, Energ. Policy, 33 (2005) 1261-1270.
[6] E.S. Karapidakis, A.A. Tsave, P. Soupios, Y. Katsigiannis, Energy efficiency and environmental impact of biogas utilization in landfills, Int. J. Environ. Sci. Te., 7 (2010) 599-608.
[7] W.B. Association, WBA global bioenergy statistics 2015, 2015.
[8] J.B. Holm-Nielsen, T. Al Seadi, P. Oleskowicz-Popiel, The future of anaerobic digestion and biogas utilization, J. Bioresource Tech., 100 (2009) 5478-5484.
[9] R. Hakawati, B.M. Smyth, G. McCullough, F. De Rosa, D. Rooney, What is the most energy efficient route for biogas utilization: heat, electricity or transport?, J. Appl. Energ., 206 (2017) 1076-1087.
[10] P. Weiland, Biogas production: current state and perspectives, Appl. Microbiol. Biot., 85 (2010) 849-860.
[11] O. Edenhofer, R. Pichs-Madruga, Y. Sokona, E. Farahani, S. Kadner, K. Seyboth, A. Adler, I. Baum, S. Brunner, P. Eickemeier, Mitigation of climate change, Contribution of Working Group III to the 5th Assessment Report of the Intergovernmental Panel on Climate Change. Cambridge. United Kingdom, (2014).
[12] M. Pöschl, S. Ward, P. Owende, Evaluation of energy efficiency of various biogas production and utilization pathways, J. Appl. Energ., 87 (2010) 3305-3321.
[13] S.E. Hosseini, M.A. Wahid, Biogas utilization: Experimental investigation on biogas flameless combustion in lab-scale furnace, J. Energ. Convers. Manage., 74 (2013) 426-432.
[14] R. Kapoor, P. Ghosh, B. Tyagi, V.K. Vijay, V. Vijay, I.S. Thakur, H. Kamyab, D.D. Nguyen, A. Kumar, Advances in biogas valorization and utilization systems: A comprehensive review, J. Clean. Prod., 273 (2020) 123052.
[15] P. Patrizio, S. Leduc, D. Chinese, E. Dotzauer, F. Kraxner, Biomethane as transport fuel–a comparison with other biogas utilization pathways in northern Italy, J. Appl. Energ., 157 (2015) 25-34.
[16] C.B. Association, Canadian 2020 Biogas Market Report – Summary, in: C.B. Association (Ed.), 2021.
[17] H. Yang, Z. Xu, M. Fan, R. Gupta, R.B. Slimane, A.E. Bland, I. Wright, Progress in carbon dioxide separation and capture: A review, J. Environ. Sci., 20 (2008) 14-27.
[18] M.K. Mondal, H.K. Balsora, P. Varshney, Progress and trends in CO_2 capture/separation technologies: A review, Energy, 46 (2012) 431-441.
[19] E.I. Koytsoumpa, C. Bergins, E. Kakaras, The CO_2 economy: Review of CO_2 capture and reuse technologies, J. Supercrit. Fluid., 132 (2018) 3-16.
[20] S. Perathoner, G. Centi, CO_2 recycling: a key strategy to introduce green energy in the chemical production chain, ChemSusChem, 7 (2014) 1274-1282.
[21] G. Centi, S. Perathoner, Opportunities and prospects in the chemical recycling of carbon dioxide to fuels, Catal. Today, 148 (2009) 191-205.

[22] W. Wang, S. Wang, X. Ma, J. Gong, Recent advances in catalytic hydrogenation of carbon dioxide, Chem. Soc. Rev., 40 (2011) 3703-3727.
[23] D.S. Simakov, Renewable synthetic fuels and chemicals from carbon dioxide: fundamentals, catalysis, design considerations and technological challenges, Springer2017.
[24] Y. Chen, N.S. Lewis, C. Xiang, Operational constraints and strategies for systems to effect the sustainable, solar-driven reduction of atmospheric CO_2, Energ. Environ. Sci., 8 (2015) 3663-3674.
[25] B. Kumar, M. Llorente, J. Froehlich, T. Dang, A. Sathrum, C.P. Kubiak, Photochemical and photoelectrochemical reduction of CO_2, Annu. Rev. Phys. Chem., 63 (2012) 541-569.
[26] G. Garbarino, D. Bellotti, P. Riani, L. Magistri, G. Busca, Methanation of carbon dioxide on Ru/Al_2O_3 and Ni/Al_2O_3 catalysts at atmospheric pressure: Catalysts activation, behaviour and stability, Int. J. Hydrog. Energ., 40 (2015) 9171-9182.
[27] Y.A. Daza, J.N. Kuhn, CO_2 conversion by reverse water gas shift catalysis: comparison of catalysts, mechanisms and their consequences for CO_2 conversion to liquid fuels, RSC Adv., 6 (2016) 49675-49691.
[28] M.D. Porosoff, B. Yan, J.G. Chen, Catalytic reduction of CO_2 by H_2 for synthesis of CO, methanol and hydrocarbons: challenges and opportunities, Energ. Environ. Sci., 9 (2016) 62-73.
[29] C.V. Miguel, M.A. Soria, A. Mendes, L.M. Madeira, Direct CO_2 hydrogenation to methane or methanol from post-combustion exhaust streams–A thermodynamic study, J. Nat. Gas Sci. Eng., 22 (2015) 1-8.
[30] B. Castellani, A. Gambelli, E. Morini, B. Nastasi, A. Presciutti, M. Filipponi, A. Nicolini, F. Rossi, Experimental investigation on CO_2 methanation process for solar energy storage compared to CO_2-based methanol synthesis, Energies, 10 (2017) 855.
[31] S. Canada, Canadian monthly natural gas distribution, Canada and provinces, 2021.
[32] S. Rönsch, J. Schneider, S. Matthischke, M. Schlüter, M. Götz, J. Lefebvre, P. Prabhakaran, S. Bajohr, Review on methanation–from fundamentals to current projects, Fuel, 166 (2016) 276-296.
[33] J. Rostrup-Nielsen, K. Pedersen, J. Sehested, High temperature methanation: Sintering and structure sensitivity, Appl. Catal. A-Gen, 330 (2007) 134-138.
[34] T. Nguyen, L. Wissing, M. Skjøth-Rasmussen, High temperature methanation: Catalyst considerations, Catal. Today, 215 (2013) 233-238.
[35] P. Dobre, F. Nicolae, F. Matei, Main factors affecting biogas production-an overview, Rom. Biotech. Lett., 19 (2014) 9283-9296.
[36] I. Angelidaki, L. Treu, P. Tsapekos, G. Luo, S. Campanaro, H. Wenzel, P.G. Kougias, Biogas upgrading and utilization: Current status and perspectives, J. Biotech. Adv., 36 (2018) 452-466.
[37] M. Miltner, A. Makaruk, M. Harasek, Review on available biogas upgrading technologies and innovations towards advanced solutions, J. Clean. Prod., 161 (2017) 1329-1337.
[38] R. Muñoz, L. Meier, I. Diaz, D. Jeison, A review on the state-of-the-art of physical/chemical and biological technologies for biogas upgrading, Rev. Environ. Sci. Bio., 14 (2015) 727-759.
[39] A. Pertl, P. Mostbauer, G. Obersteiner, Climate balance of biogas upgrading systems, Waste Manage., 30 (2010) 92-99.
[40] S.F. Ahmed, M. Mofijur, K. Tarannum, A.T. Chowdhury, N. Rafa, S. Nuzhat, P.S. Kumar, D.-V.N. Vo, E. Lichtfouse, T. Mahlia, Biogas upgrading, economy and utilization: a review, Environ. Chem. Lett., 19 (2021) 4137-4164.
[41] Q. Sun, H. Li, J. Yan, L. Liu, Z. Yu, X. Yu, Selection of appropriate biogas upgrading technology-a review of biogas cleaning, upgrading and utilisation, Renew. Sust. Energ. Rev., 51 (2015) 521-532.
[42] R. Kapoor, P. Ghosh, M. Kumar, V.K. Vijay, Evaluation of biogas upgrading technologies and future perspectives: a review, Environ. Sci. Pollut. Res., 26 (2019) 11631-11661.

[43] D. Andriani, A. Wresta, T.D. Atmaja, A. Saepudin, A review on optimization production and upgrading biogas through CO_2 removal using various techniques, Appl. Biochem. Biotech. , 172 (2014) 1909-1928.
[44] F. Osorio, J.C. Torres, Biogas purification from anaerobic digestion in a wastewater treatment plant for biofuel production, Renew. Energ., 34 (2009) 2164-2171.
[45] N. Abatzoglou, S. Boivin, A review of biogas purification processes, Biofuels Bioprod. Bioref., 3 (2009) 42-71.
[46] F.M. Baena-Moreno, E. le Saché, L. Pastor-Perez, T. Reina, Membrane-based technologies for biogas upgrading: a review, Environ. Chem. Lett., 18 (2020) 1649-1658.
[47] A.S. Calbry-Muzyka, T.J. Schildhauer, Direct Methanation of Biogas—Technical Challenges and Recent Progress, Front. Energ. Res., (2020) 356.
[48] J. Witte, J. Settino, S.M. Biollaz, T.J. Schildhauer, Direct catalytic methanation of biogas–Part I: New insights into biomethane production using rate-based modelling and detailed process analysis, Energ. Convers. and Management, 171 (2018) 750-768.
[49] D. Sun, F.M. Khan, D.S. Simakov, Heat removal and catalyst deactivation in a Sabatier reactor for chemical fixation of CO_2: Simulation-based analysis, Chem. Eng. J., 329 (2017) 165-177.
[50] D. Sun, D.S. Simakov, Thermal management of a Sabatier reactor for CO_2 conversion into CH_4: Simulation-based analysis, J. CO_2 Util., 21 (2017) 368-382.
[51] R. Currie, S. Mottaghi-Tabar, Y. Zhuang, D.S.A. Simakov, Design of an Air-Cooled Sabatier Reactor for Thermocatalytic Hydrogenation of CO_2: Experimental Proof-of-Concept and Model-Based Feasibility Analysis, Ind. Eng. Chem. Res., 58 (2019) 12964-12980.
[52] T. Bligaard, J.K. Nørskov, S. Dahl, J. Matthiesen, C.H. Christensen, J. Sehested, The Brønsted–Evans–Polanyi relation and the volcano curve in heterogeneous catalysis, J. Catal., 224 (2004) 206-217.
[53] M.H. Amin, K. Mantri, J. Newnham, J. Tardio, S.K. Bhargava, Highly stable ytterbium promoted Ni/γ-Al_2O_3 catalysts for carbon dioxide reforming of methane, Appl. Catal. B: Environ., 119 (2012) 217-226.
[54] H. Muroyama, Y. Tsuda, T. Asakoshi, H. Masitah, T. Okanishi, T. Matsui, K. Eguchi, Carbon dioxide methanation over Ni catalysts supported on various metal oxides, J. Catal., 343 (2016) 178-184.
[55] M. Vannice, The catalytic synthesis of hydrocarbons from carbon monoxide and hydrogen, Catal. Rev., 14 (1976) 153-191.
[56] C. Bartholomew, Catalyst deactivation and regeneration, Kirk Othmer Encyclopedia of Chemical Technology2000, pp. 13-15.
[57] T.J. Schildhauer, S. Biollaz, Reactors for catalytic methanation in the conversion of biomass to synthetic natural gas (SNG), CHIMIA Int. J. Chem., 69 (2015) 603-607.
[58] HELMETH, Methanation process 2017.
[59] H.Z.I. AG, Power-to-Gas, 2017.
[60] G. Benjaminsson, J. Benjaminsson, R.B. Rudberg, Power-to-Gas: a technical review, Svenskt gastekniskt center2013.
[61] R. Lohmüller, Methansynthese mit kombinierten isothermen und adiabaten Reaktoren, Berichte aus Technik und Wissenschaft, (1977).
[62] K.P. Brooks, J. Hu, H. Zhu, R.J. Kee, Methanation of carbon dioxide by hydrogen reduction using the Sabatier process in microchannel reactors, Chem. Eng. Sci., 62 (2007) 1161-1170.
[63] M. Sudiro, A. Bertucco, G. Groppi, E. Tronconi, Simulation of a structured catalytic reactor for exothermic methanation reactions producing synthetic natural gas, Computer Aided Chemical Engineering, Elsevier2010, pp. 691-696.

[64] W.J. Lee, C. Li, H. Prajitno, J. Yoo, J. Patel, Y. Yang, S. Lim, Recent trend in thermal catalytic low temperature CO_2 methanation: A critical review, Catal. Today, (2020).
[65] J. Li, L. Zhou, P. Li, Q. Zhu, J. Gao, F. Gu, F. Su, Enhanced fluidized bed methanation over a Ni/Al_2O_3 catalyst for production of synthetic natural gas, Chem. Eng. J., 219 (2013) 183-189.
[66] M.C. Seemann, T.J. Schildhauer, S.M. Biollaz, Fluidized bed methanation of wood-derived producer gas for the production of synthetic natural gas, Ind. Eng. Chem. Res., 49 (2010) 7034-7038.
[67] J. Kopyscinski, T.J. Schildhauer, S.M. Biollaz, Fluidized-bed methanation: interaction between kinetics and mass transfer, Ind. Eng. Chem. Res., 50 (2010) 2781-2790.
[68] W. Lommerzheim, C. Flockenhaus, One stage combined shift-conversion and partial methanation process for upgrading synthesis gas to pipeline quality, Proceeding of tenth synthetic pipeline gas symposium, Chicago, American Gas Association, 1978, pp. 439-451.
[69] B. Liu, S. Ji, Comparative study of fluidized-bed and fixed-bed reactor for syngas methanation over $Ni-W/TiO_2-SiO_2$ catalyst, J. Energ. Chem., 22 (2013) 740-746.
[70] J. Kopyscinski, T.J. Schildhauer, S.M. Biollaz, Methanation in a fluidized bed reactor with high initial CO partial pressure: Part I—Experimental investigation of hydrodynamics, mass transfer effects, and carbon deposition, Chem. Eng. Sci., 66 (2011) 924-934.
[71] D. Kunii, O. Levenspiel, Fluidization Engineering, Elsevier2013.
[72] C. Junaedi, K. Hawley, D. Walsh, S. Roychoudhury, M. Abney, J. Perry, Compact and lightweight sabatier reactor for carbon dioxide reduction, 41st International Conference on Environmental SystemsPortland, OR, US, 2011.
[73] C. Junaedi, K. Hawley, D. Walsh, S. Roychoudhury, M.B. Abney, J.L. Perry, CO_2 Reduction assembly prototype using microlith-based sabatier reactor for ground demonstration, 44th International Conference on Environmental SystemsTuscon, AZ, US, 2014.
[74] J.O. Thompson, Scaleable, High Efficiency Microchannel Sabatier Reactor, 45th International Conference on Environmental SystemsBellevue, WA, US, 2015.
[75] M. Biset-Peiró, R. Mey, J. Guilera, T. Andreu, Adiabatic plasma-catalytic reactor configuration: energy efficiency enhancement by plasma and thermal synergies on CO_2 methanation, Chem. Eng. J., (2020) 124786.
[76] M. Götz, F. Ortloff, R. Reimert, O. Basha, B.I. Morsi, T. Kolb, Evaluation of organic and ionic liquids for three-phase methanation and biogas purification processes, Energ. Fuel, 27 (2013) 4705-4716.
[77] J. Lefebvre, M. Götz, S. Bajohr, R. Reimert, T. Kolb, Improvement of three-phase methanation reactor performance for steady-state and transient operation, Fuel Process. Technol., 132 (2015) 83-90.
[78] M. Götz, J. Lefebvre, D. Schollenberger, S. Bajohr, R. Reimert, T. Kolb, Novel methanation concepts for the production of Substitute Natural Gas, International Gas Union Research Conference (IGRC), 2013.
[79] J. Witte, A. Calbry-Muzyka, T. Wieseler, P. Hottinger, S.M. Biollaz, T.J. Schildhauer, Demonstrating direct methanation of real biogas in a fluidised bed reactor, Appl. Energ., 240 (2019) 359-371.
[80] C. Dannesboe, J.B. Hansen, I. Johannsen, Catalytic methanation of CO_2 in biogas: Experimental results from a reactor at full scale, React. Chem. Eng., 5 (2020) 183-189.
[81] P.J.S. de Miranda, E.o.H.B.E. Technologies, Chapter 5.3. 3-application of hydrogen by use of chemical reactions of hydrogen and carbon dioxide, J. Sci. Eng, Hydrogen Based Energ. Tech., (2019) 279-289.

[82] J.A.H. Lalinde, P. Roongruangsree, J. Ilsemann, M. Baeumer, J. Kopyscinski, CO_2 methanation and reverse water gas shift reaction. Kinetic study based on in situ spatially-resolved measurements, Chem. Eng. J., 390 (2020) 124629.
[83] L. Aparicio, Transient isotopic studies and microkinetic modeling of methane reforming over nickel catalysts, J. Catal., 165 (1997) 262-274.
[84] C.V. Miguel, A. Mendes, L.M. Madeira, Intrinsic kinetics of CO_2 methanation over an industrial nickel-based catalyst, J. CO_2 Util., 25 (2018) 128-136.
[85] S. Wu, K. McAuley, T. Harris, Selection of simplified models: II. Development of a model selection criterion based on mean squared error, Can. J. Chem. Eng., 89 (2011) 325-336.
[86] M. Götz, J. Lefebvre, F. Mörs, A.M. Koch, F. Graf, S. Bajohr, R. Reimert, T. Kolb, Renewable Power-to-Gas: A technological and economic review, Renew. Energ., 85 (2016) 1371-1390.
[87] T. Chwoła, T. Spietz, L. Więcław-Solny, A. Tatarczuk, A. Krótki, S. Dobras, A. Wilk, J. Tchórz, M. Stec, J. Zdeb, Pilot plant initial results for the methanation process using CO_2 from amine scrubbing at the Łaziska power plant in Poland, Fuel, 263 (2020) 116804.
[88] M. Hervy, J. Maistrello, L. Brito, M. Rizand, E. Basset, Y. Kara, M. Maheut, Power-to-gas: CO_2 methanation in a catalytic fluidized bed reactor at demonstration scale, experimental results and simulation, J. CO_2 Util., 50 (2021) 101610.
[89] C. Dannesboe, J.B. Hansen, I. Johannsen, Removal of sulfur contaminants from biogas to enable direct catalytic methanation, Biomass Conv. Bior., 11 (2021) 1823-1834.
[90] J. Guilera, T. Andreu, N. Basset, T. Boeltken, F. Timm, I. Mallol, J.R. Morante, Synthetic natural gas production from biogas in a waste water treatment plant, Renew. Energ., 146 (2020) 1301-1308.
[91] M. Specht, J. Brellochs, V. Frick, B. Stürmer, U. Zuberbühler, The Power to Gas Process: Storage of Renewable Energy in the Natural Gas Grid via Fixed Bed Methanation of CO_2/H_2, Syn. Natural gas from coal, dry biomass,
power-to-gas Appl., (2016).
[92] D.E. Mears, Tests for transport limitations in experimental catalytic reactors, Ind. Eng. Chem. Proc. DD., 10 (1971) 541-547.
[93] N. Wakao, S. Kaguei, T. Funazkri, Effect of fluid dispersion coefficients on particle-to-fluid heat transfer coefficients in packed beds: correlation of Nusselt numbers, J. Chem. Eng. Sci, 34 (1979) 325-336.
[94] H.S. Fogler, S.H. Fogler, Elements of chemical reaction engineering, Pearson Educación1999.
[95] R. Mutschler, E. Moioli, A. Züttel, Modelling the CO_2 hydrogenation reaction over Co, Ni and Ru/Al_2O_3, J. Catal., 375 (2019) 193-201.
[96] G. Chabot, R. Guilet, P. Cognet, C. Gourdon, A mathematical modeling of catalytic milli-fixed bed reactor for Fischer–Tropsch synthesis: Influence of tube diameter on Fischer Tropsch selectivity and thermal behavior, J. Chem. Eng. Sci, 127 (2015) 72-83.
[97] R.J. Berger, J. Pérez-Ramırez, F. Kapteijn, J.A. Moulijn, Catalyst performance testing: Radial and axial dispersion related to dilution in fixed-bed laboratory reactors, Appl. Catal. A-Gen, 227 (2002) 321-333.
[98] R. Roberts, Molecular diffusion of gases, J. Am. Inst. Phys., (1963) 235.
[99] S.W. Churchill, H.H. Chu, Correlating equations for laminar and turbulent free convection from a vertical plate, Int. J. Heat Mass Tran., 18 (1975) 1323-1329.
[100] O. Sergeev, A. Shashkov, A. Umanskii, Thermophysical properties of quartz glass, J. Eng. Phys., 43 (1982) 1375-1383.
[101] R. Morrell, Handbook of Properties of Technical and Engineering Ceramics. Part 2: Data Reviews. Section I: High-Alumina Ceramics, Her Majesty's Stationery Office, (1987) 255.

[102] Y. Touloukian, R. Kirby, E. Taylor, T. Lee, Thermophysical properties of matter-the tprc data series. volume 13. thermal expansion-nonmetallic solids, Thermophysical and Electronic Properties Information Analysis Center, 1977.

Appendix A

Flow system configuration

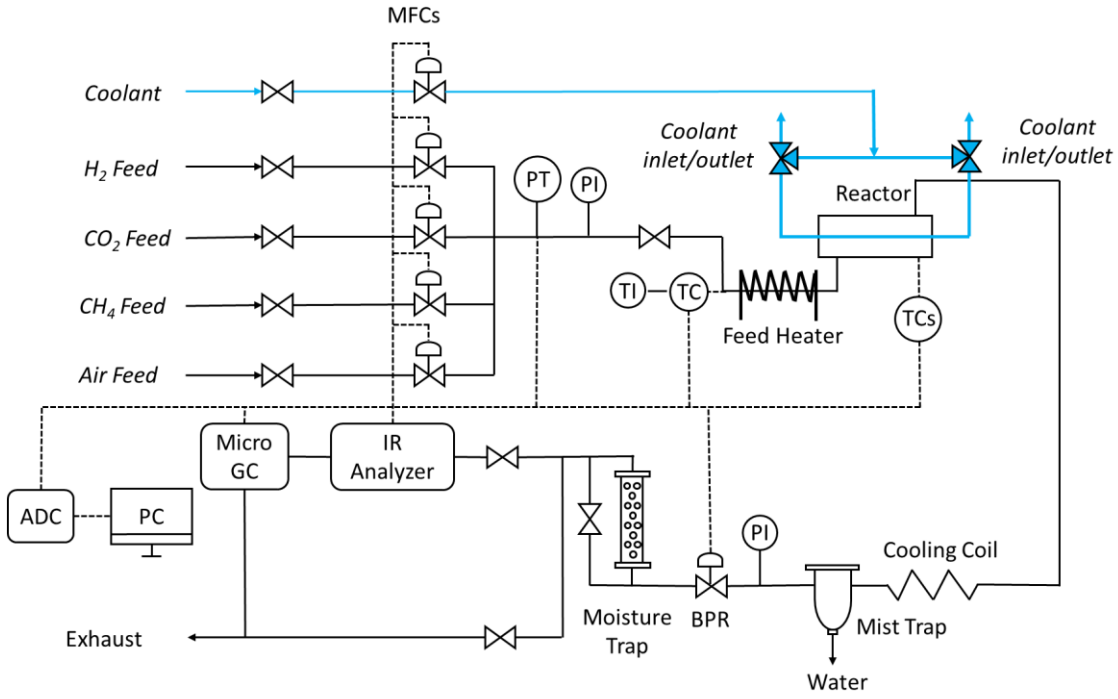

Fig. S1. Flow system setup. Abbreviations: ADC – analog-to-digital converter, BPR – back pressure regulator, IR – infrared, MFC – mass flow controller, PI – pressure indicator, PC – computer, PT – pressure transducer, TC – thermocouple, TI – temperature indicator and controller.

The flow system used in all reactor tests is shown in Fig. S1. For isothermal experiments, a kinetic reactor (Fig. S2) was placed inside the furnace (Lindberg/Blue M™ Mini-Mite™ Tube Furnaces, Thermo Fisher Scientific). A K-type thermocouple (1/8″, Omega Engineering) was inserted through the outlet tube so that the thermocouple tip is in contact with the catalyst bed. For reactor experiments, Reactors 1, 2 and 3 were connected to the flow system using

stainless steel tubing. The furnace was used for the feed preheating for Reactors 1 and 2 (Figs S3, S4). For Reactor 3, the feed line was preheated with a heating tape (Fig. S5).

Flow rates were controlled by mass flow controllers (Bronkhorst High-Tech B.V.). Two three-way valves (Swagelok) were used to change the direction of the coolant (for concurrent or countercurrent operation). An electronic back pressure regulator (Bronkhorst High-Tech B.V.) was used to adjust the reactor pressure. Water was removed from the outlet stream using a mist trap (SMC Corporation, AFM40-N02-Z-A) installed before the back pressure regulator, and a silica gel column (Agilent Technologies, 5182-9411, the original adsorbent was replaced with orange silica gel, Fisher Scientific). Concentrations of CO, CO_2 and CH_4 in the outlet stream were measured on a dry basis (after the removal of water and moisture) with an IR analyzer (IR-208, Infrared Industries, Inc., USA). The entire flow system was computer-controlled using a custom-made control panel coded in LabVIEW (National Instruments) and analog-to-digital converters (NI 9215, NI 9263, National Instruments). All flow rates, pressures, temperatures and outlet gas concentrations were continuously monitored and recorded. CO_2 conversion, selectivity to CH_4 formation and carbon balance (see Appendix C) were continuously calculated, displayed and recorded through the duration of the entire experiment. A microGC (MircoGC Fusion Gas Analyzer, Inficon) was used to measure O_2 and N_2 concentrations in synthetic biogas experiments.

Appendix B

Reactor configurations (CO_2 methanation)

The kinetic reactor, Fig. S2, was made from a 1/4″ stainless steel union tee (Swagelok) connected to 1/4″ stainless steel tubing on both sides (Swagelok), with a type K-type thermocouple (1/8″, Omega Engineering, Inc.) placed in contact with the catalytic bed. Commercial catalytic pellets (12 wt% Ni/Al_2O_3, BASF, supplied by Research Catalysts, Inc. USA) were crushed and sieved to 0.275-0.425 mm pellets. The catalyst (250 mg) was loaded into the union tee, which was sealed at the top with a stainless steel plug (Swagelok). The reactor was placed in a furnace (see *Appendix A*) to maintain isothermal operation.

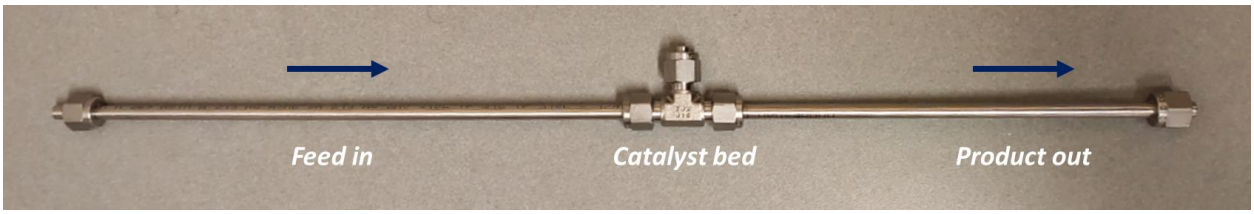

Fig. S2. Kinetic reactor configuration.

Reactor 1 was built from 0.25″ stainless steel tubing and Swagelok connectors, Fig. S3. Commercial catalytic pellets (12 wt% Ni/Al_2O_3, BASF, supplied by Research Catalysts, Inc. USA) were crushed and sieved to 0.275-0.425 mm pellets; 1.4 g of catalyst was used. Two K-type thermocouples (1/8″, Omega Engineering) were placed before and after the catalytic bed (being in direct contact with the catalyst) to monitor the reactor inlet (T_{in}) and outlet (T_{out}) temperatures. The reactor was placed next to the furnace, which was used for the feed preheating. Given the small size of the reactor, no active cooling system was installed. The reactor body was warped in quartz wool and covered with aluminum foil for thermal insulation.

Feed temperature (T_f) was measured using a thermocouple installed in contact with the feed tube extremal wall close to the furnace exit.

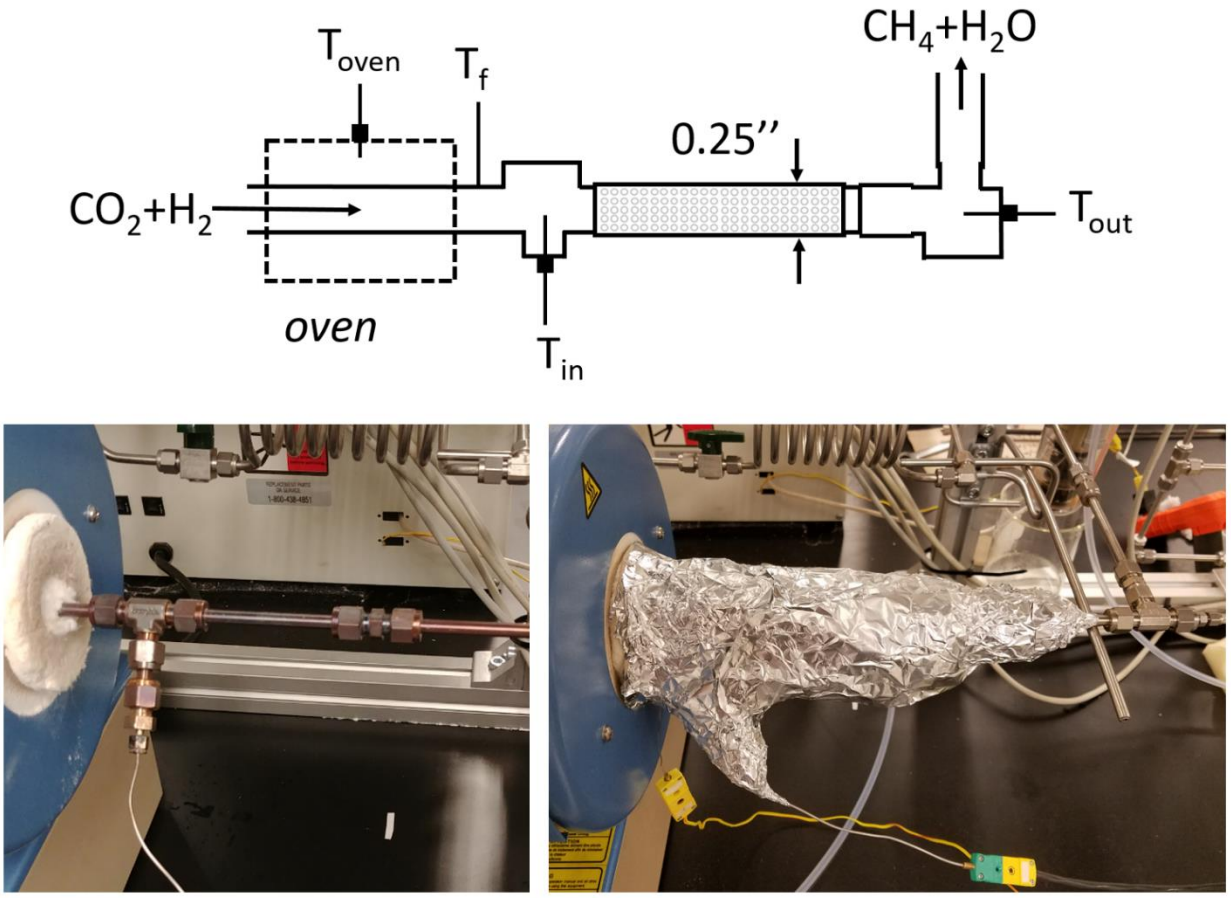

Fig. S3. Reactor 1 scheme and pictures (installed in the flow system, with and without insulation).

Reactor 2 was made from a 5″ long 1/2″ OD stainless steel tube, with a piece of 1/4″ OD tube placed inside (tube-and-shell) for active cooling using compressed N_2, Fig. S4. Reducing tees (Swagelok) were used to seal the space between the 1/4″ cooling tube and the 1/2″ reactor. K-type thermocouples (1/8″, Omega Engineering, Inc.) were placed inside the cooling tube to

estimate the reactor inlet (T_{in}) and outlet (T_{out}) temperatures. Another thermocouple (K-type, 1/8″, Omega Engineering, Inc.) was placed before the reactor inlet to measure the feed temperature (T_f). Commercial catalytic pellets (12 wt% Ni/Al_2O_3, BASF, supplied by Research Catalysts, Inc. USA) were crushed and sieved to 0.275-0.425 mm pellets. The resulted pellets (7.2 g) were loaded via the 1/2″ ports of the tee connectors and capped with stainless steel mesh and quartz wool. The oven was used to heat the feed stream. The reactor body assembly was wrapped in a 3 cm thick layer of quartz wool and covered with aluminum foil for thermal insulation. The gap between the furnace and the reactor was also filled with quartz wool and covered with aluminum foil to minimize heat losses.

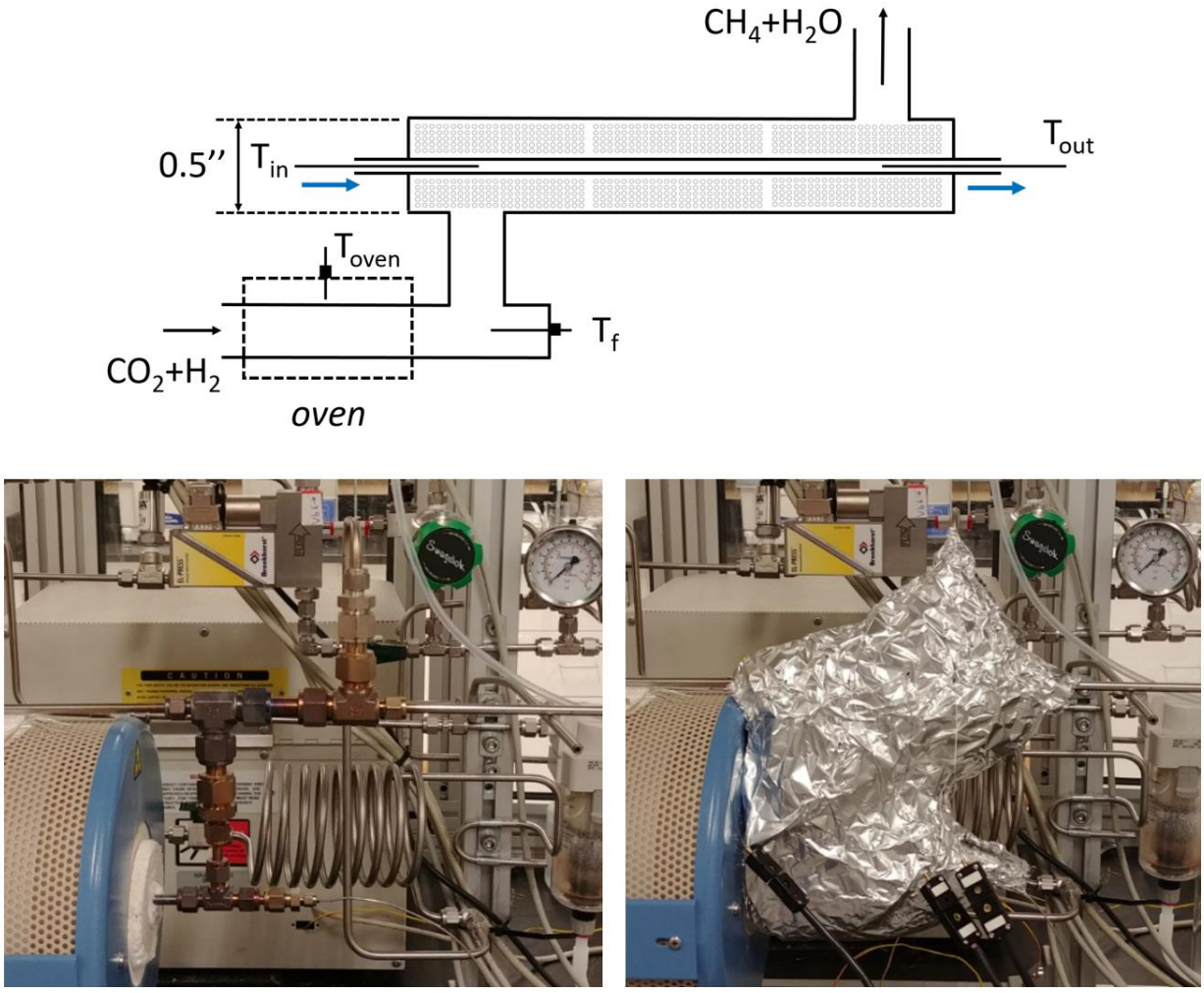

Fig. S4. Reactor 2 scheme and pictures (installed in the flow system, with and without insulation).

The outer diameter of Reactor 3 shell side was increased to 1″. The main reactor body was assembled from a piece of 1″ stainless steel tube and two reducing tees (Swagelok) as shown in Fig. S5. Commercial catalytic pellets (12 wt% Ni/Al_2O_3, BASF, supplied by Research Catalysts, Inc. USA) were crushed and sieved to 0.7-1 mm pellets. The catalyst (63 g) was filled into the reactor via the 1″ port on the reducing tee and stainless-steel mesh and quartz

wool were placed on top of the 1″ port, preventing the catalyst bed from moving. The length of the active bed was 9″. The cooling tube was a 1/4″ OD stainless steel placed inside the 1″ tube (tube-and-shell). N_2 was used as the coolant.

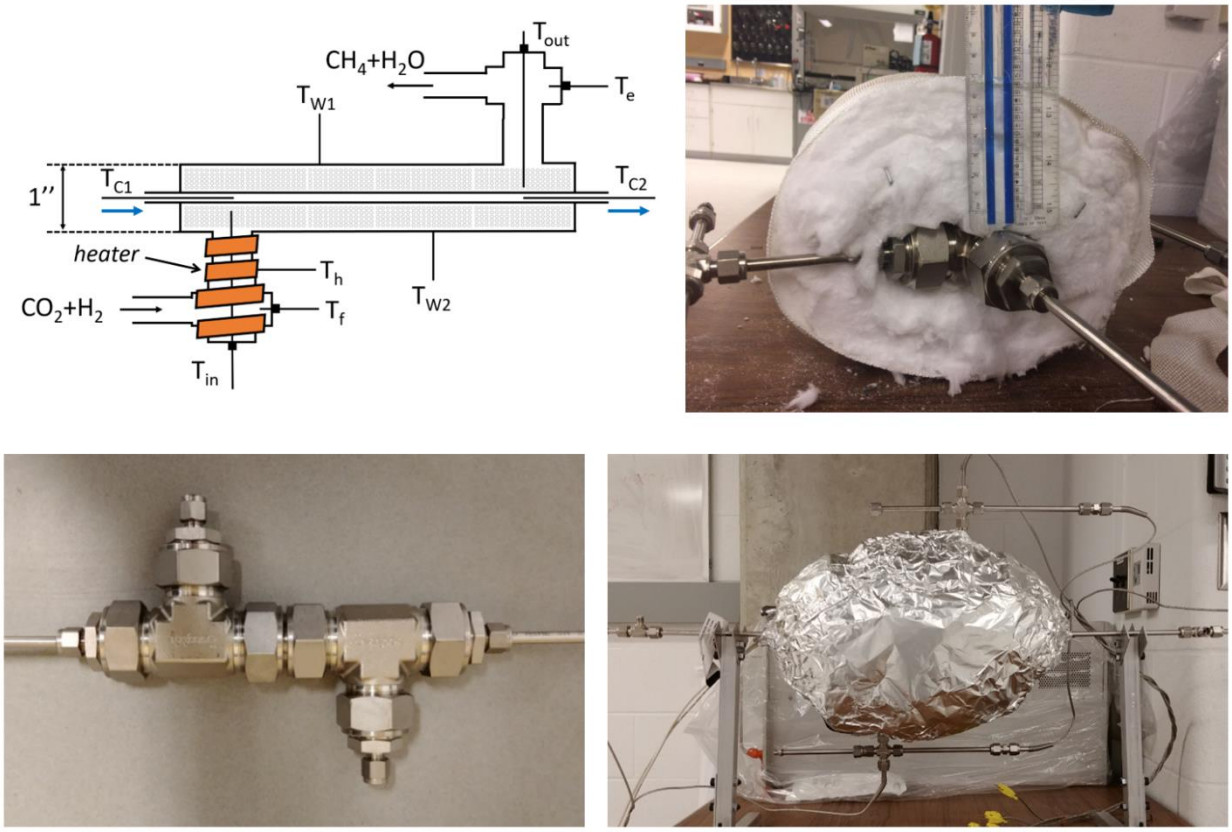

Fig. S5. Reactor 3 scheme and pictures (showing the main reactor body, the thickness of the insulation layer and complete reactor with installed thermocouples).

A heating tape (300 W, Omega Engineering) with a temperature controller (CN7200, Omega Engineering) was wrapped around the inlet for feed preheating. A thermocouple (K-type, 1/16″, Omega Engineering, Inc.) was placed in contact with the heating tape (T_h in Fig. S5). The reactor body assembly was wrapped with a layer of quartz wool and covered with

aluminum foil for thermal insulation. Thermocouples (K-type, 1/8″, Omega Engineering, Inc.) were placed inside the catalytic bed at the reactor inlet/outlet (T_{in}, T_{out}), at inlet/outlet ends of the cooling tube (T_{C1}, T_{C2}), and inside the feed/effluent lines (T_{W1}, T_{W2}). Two additional thermocouples (J-type, 1/16″, Omega Engineering, Inc.) were placed on the reactor wall (T_{W1}, T_{W2}).

Appendix C

Reactor configurations (direct biogas upgrade)

The packed bed reactor for evaluating raw biogas upgrade, Fig. S6, was made from a 2″ long 1/4″ OD stainless steel tube, connected between a 1/4″ and a 3/8″ stainless steel tube, with a type K-type thermocouple (1/8″, Omega Engineering, Inc.) placed in contact with the catalytic bed. Commercial catalytic pellets (12 wt% Ni/Al_2O_3, BASF, supplied by Research Catalysts, Inc. USA) were crushed and sieved to 0.275-0.425 mm pellets. The catalyst (800 mg) was loaded into the stainless steel tube, and two pieces of quartz wool were placed on each side to make sure the catalyst stays in place under flow. The reactor was placed inside a furnace (see *Appendix A*) to maintain isothermal operation.

Fig. S6. Reactor configuration for raw biogas upgrade.

Configurations of Reactor 1, 2 and 3 utilized in direct biogas upgrade are the same reactors used in Chapter 3 (CO_2 methanation) but with minor changes on the thermal insulation and thermocouple placement. The changes are highlighted with bold fonts.

Reactor 1 was built from 0.25″ stainless steel tubing and Swagelok connectors, Fig. S7. Commercial catalytic pellets (12 wt% Ni/Al_2O_3, BASF, supplied by Research Catalysts, Inc. USA) were crushed and sieved to 0.275-0.425 mm pellets; 1.4 g of catalyst was used. Two K-type thermocouples (1/8″, Omega Engineering) were placed before and after the catalytic bed

(being in direct contact with the catalyst) to monitor the reactor inlet (T_{in}) and outlet (T_{out}) temperatures. The reactor was placed next to the furnace, which was used for the feed preheating. Given the small size of the reactor, no active cooling system was installed. The reactor body was warped in quartz wool and covered with aluminum foil for thermal insulation. Feed temperature (T_f) was measured using a thermocouple installed in contact with the feed tube extremal wall close to the furnace exit.

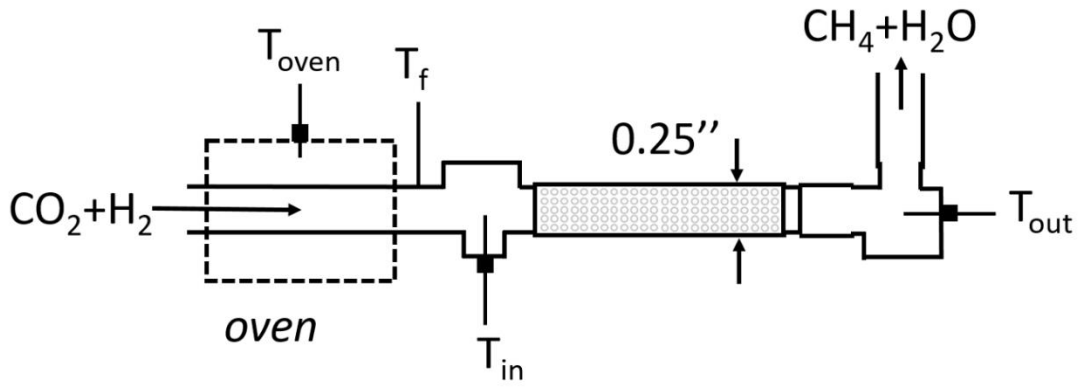

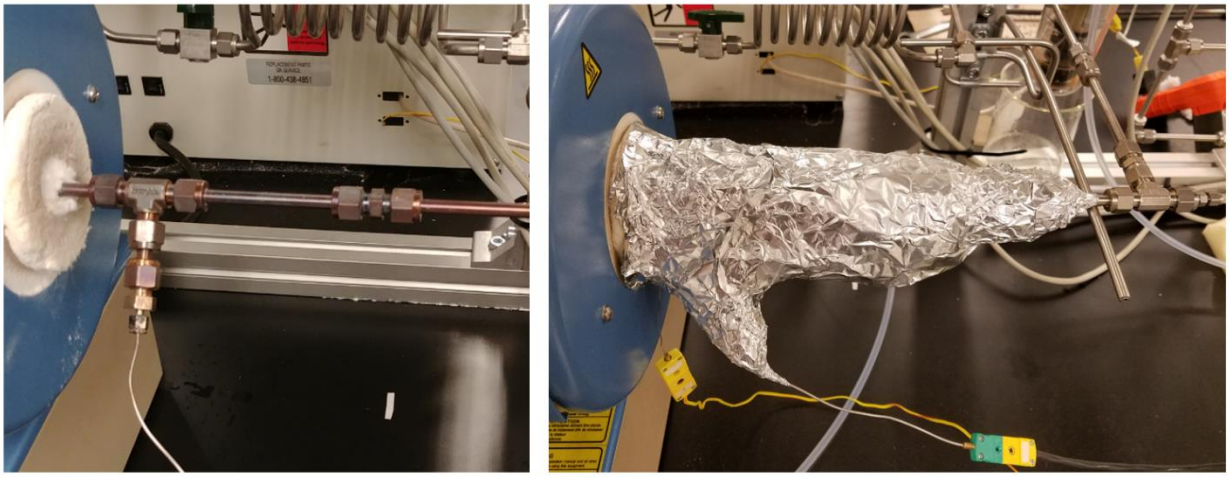

Fig. S7. Reactor 1 scheme and pictures (installed in the flow system, with and without insulation).

Reactor 2 was made from a 5″ long 1/2″ OD stainless steel tube, with a piece of 1/4″ OD tube placed inside (tube-and-shell) for active cooling using compressed N_2, Fig. S8. Reducing tees (Swagelok) were used to seal the space between the 1/4″ cooling tube and the 1/2″ reactor. K-type thermocouples (1/8″, Omega Engineering, Inc.) were placed inside the cooling tube to estimate the reactor inlet (T_{in}) and outlet (T_{out}) temperatures. Another thermocouple (K-type, 1/8″, Omega Engineering, Inc.) was placed before the reactor inlet to measure the feed temperature (T_f). Commercial catalytic pellets (12 wt% Ni/Al_2O_3, BASF, supplied by Research Catalysts, Inc. USA) were crushed and sieved to 0.275-0.425 mm pellets. The resulted pellets (7.2 g) were loaded via the 1/2″ ports of the tee connectors and capped with stainless steel mesh and quartz wool. The oven was used to heat the feed stream. The reactor body assembly was wrapped in a 3 cm thick layer of quartz wool and covered with aluminum foil for thermal insulation. The gap between the furnace and the reactor was also filled with quartz wool and covered with aluminum foil to minimize heat losses. Four J-type 1/16″ thermocouples (**Tw_1, Tw_2, Tw_3 and Tw_4**) were installed on the reactor wall to monitor the temperature profile along the reactor.

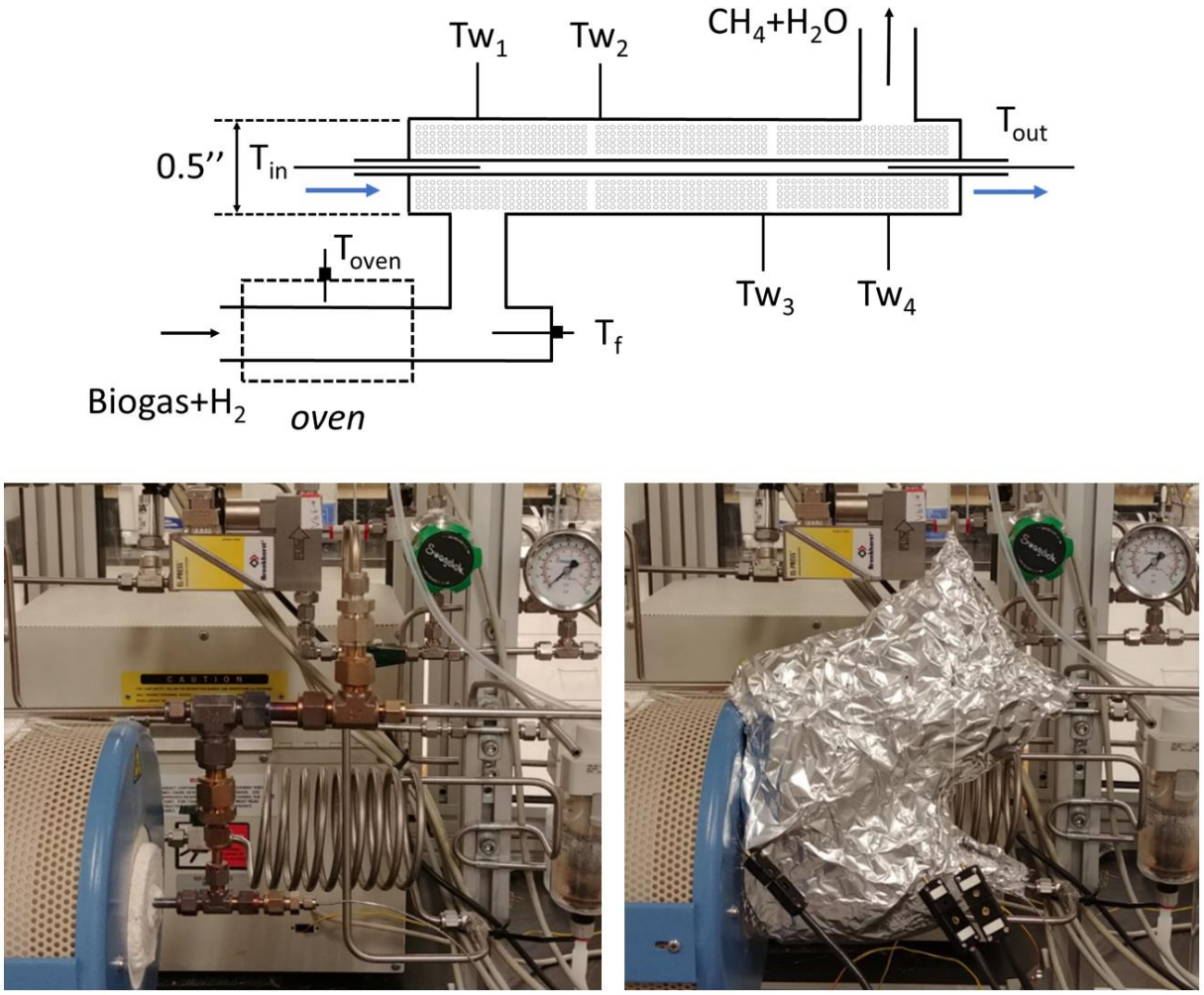

Fig. S8. Reactor 2 scheme and pictures (installed in the flow system, with and without insulation).

The outer diameter of Reactor 3 shell side was increased to 1″. The main reactor body was assembled from a piece of 1″ stainless steel tube and two reducing tees (Swagelok) as shown in Fig. S9. Commercial catalytic pellets (12 wt% Ni/Al_2O_3, BASF, supplied by Research Catalysts, Inc. USA) were crushed and sieved to 0.7-1 mm pellets. The catalyst (63 g) was filled into the reactor via the 1″ port on the reducing tee and stainless-steel mesh and quartz

wool were placed on top of the 1″ port, preventing the catalyst bed from moving. The length of the active bed was 9″. The cooling tube was a 1/4″ OD stainless steel placed inside the 1″ tube (tube-and-shell). N_2 was used as the coolant.

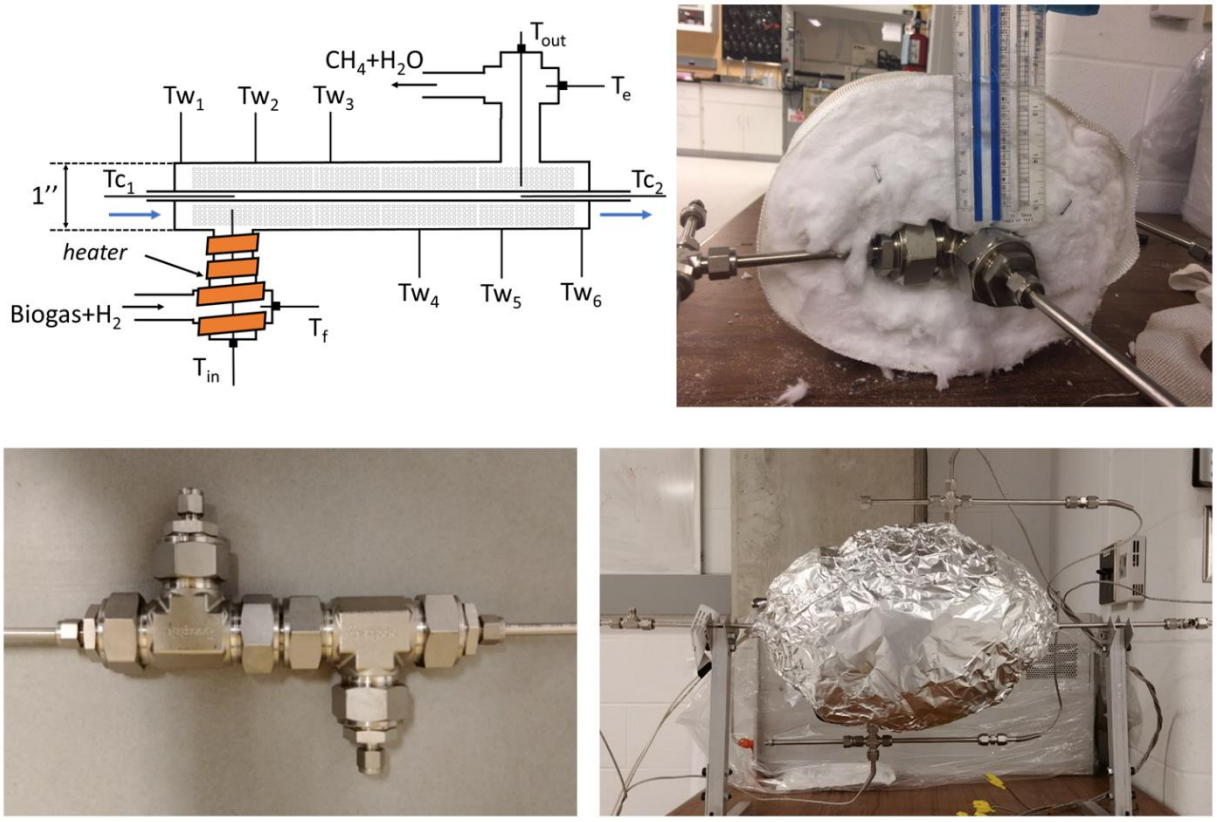

Fig. S9. Reactor 3 scheme and pictures (showing the main reactor body, the thickness of the insulation layer and complete reactor with installed thermocouples).

A heating tape (300 W, Omega Engineering) with a temperature controller (CN7200, Omega Engineering) was wrapped around the inlet for feed preheating. A thermocouple (K-type, 1/16″, Omega Engineering, Inc.) was placed in contact with the heating tape (Fig. S5). The reactor body assembly was wrapped with a layer of quartz wool and covered with

aluminum foil for thermal insulation. Thermocouples (K-type, 1/8″, Omega Engineering, Inc.) were placed inside the catalytic bed at the reactor inlet/outlet (T_{in}, T_{out}), at inlet/outlet ends of the cooling tube (T_{C1}, T_{C2}), and inside the feed/effluent lines (T_f, T_e). **Six additional thermocouples** (K-type, 1/16″, Omega Engineering, Inc.) were placed on the reactor wall (**Tw_1, Tw_2, Tw_3, Tw_4, Tw_5, Tw_6**).

Appendix D

Carbon balance derivation

Carbon balance, defined as the total rate of carbon fed to the reactor divided by the rate of carbon exiting the reactor, was computed using the following equation (y_{CO_2}, y_{CO} and y_{CH_4} are mole fractions measured by the IR analyzer):

$$CB = (y_{CO_2} + y_{CO} + y_{CH_4})(1 + \alpha - f_1 - 4f_2 + \gamma)(1 - \beta) \quad \text{(S1)}$$

In Eq. (S1), α, β, γ, f_1, and f_2 are the H_2:CO_2 ratio in the feed, CH_4 content in the feed, CH_4:CO_2 ratio in the feed, conversion to CO, and conversion to CH_4, respectively, as defined in Eqs (S2-S5) below ($F_{C,out}$ is the total outlet molar flow rate of all carbon-containing species). In the case of pure CO_2 feed, both β and γ equal to 0 and are removed from the calculations.

$$\alpha = \frac{F_{H_2,f}}{F_{CO_2,f}} \quad \text{(S2)}$$

$$\beta = \frac{F_{CH_4,f}}{F_{CH_4,f} + F_{CO_2,f}} \equiv \frac{F_{CH_4,f}}{F_{C,f}} \quad \text{(S3)}$$

$$\gamma = \frac{F_{CH_4,f}}{F_{CO_2,f}}$$

$$f_1 = \frac{y_{CO}}{(1-\beta)(y_{CO} + y_{CO_2} + y_{CH_4})} \equiv \frac{F_{CO,out}}{F_{CO_2,f}} \quad \text{(S4)}$$

$$f_2 = \frac{y_{CH_4} - \beta(y_{CO} + y_{CO_2} + y_{CH_4})}{(1-\beta)(y_{CO} + y_{CO_2} + y_{CH_4})} \equiv \frac{F_{CH_4,gen}}{F_{CO_2,f}} \quad \text{(S5)}$$

Eq. (S1) above is obtained from the carbon balance definition, Eq. (S6), using Eq. (S7) to define the total outlet molar flow rate ($F_{CO,out}$ and $F_{CH_4,out}$ correspond to H_2 consumption in RWGS and Sabatier reaction) and Eqs (S3-5):

$$CB = \frac{F_{C,out}}{F_{C,f}} = \frac{(y_{CO_2} + y_{CO} + y_{CH_4})F_{t,out}}{F_{CO_2,f}/(1-\beta)} \tag{S6}$$

$$F_{t,out} = F_{CO_2,f} + [F_{H_2,f} - F_{CO,out} - 4(F_{CH_4,out} - F_{CH_4,f})] + F_{CH_4,f} \tag{S7}$$

Appendix E

Additional experimental results in Chapter 3 (CO_2 methanation)

Additional experimental results in Chapter 3 (CO_2 methanation) are shown:

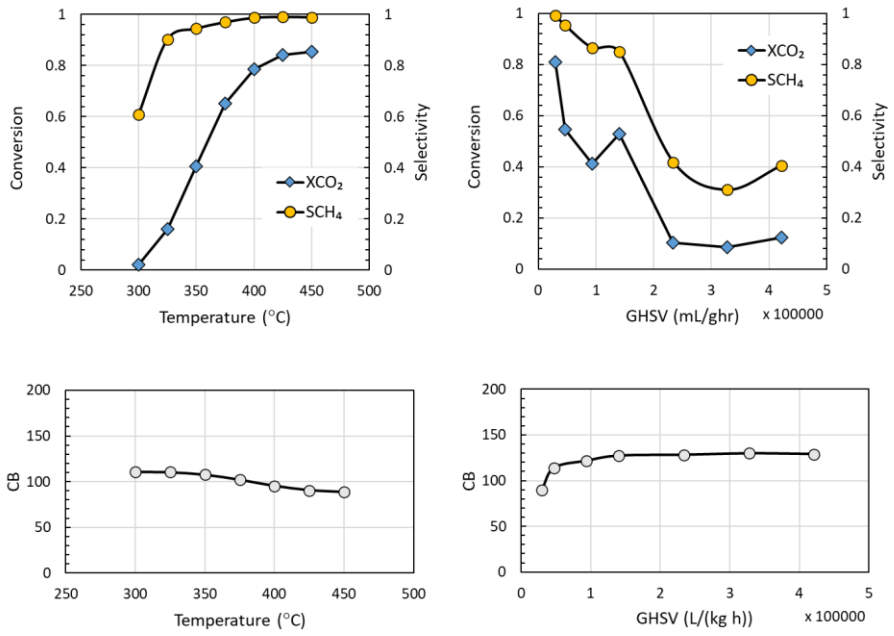

Fig. S10. CO_2 conversion and CH_4 selectivity as a function of temperature and GHSV showing corresponding carbon balance (kinetic reactor). *Parameters:* H_2:CO_2=4, P= 3 bar, GHSV=30,000 L/(kg h) (Temperature test), T=450°C (GHSV test), pure CO_2 feed.

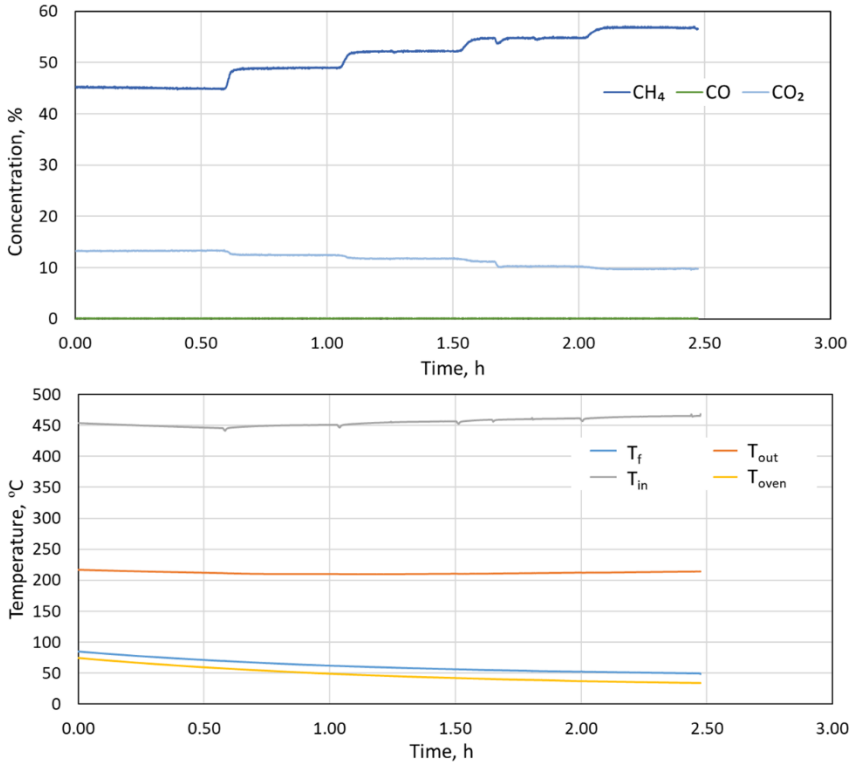

Fig. S11. The change of mole fraction and temperature with time (Reactor 2 performance as a function of pressure). *Parameters:* GHSV=16,000 L/(kg h), H_2:CO_2=4, Q_c=0.8 L/min (Countercurrent flow), T_f=20 °C, pure CO_2 feed.

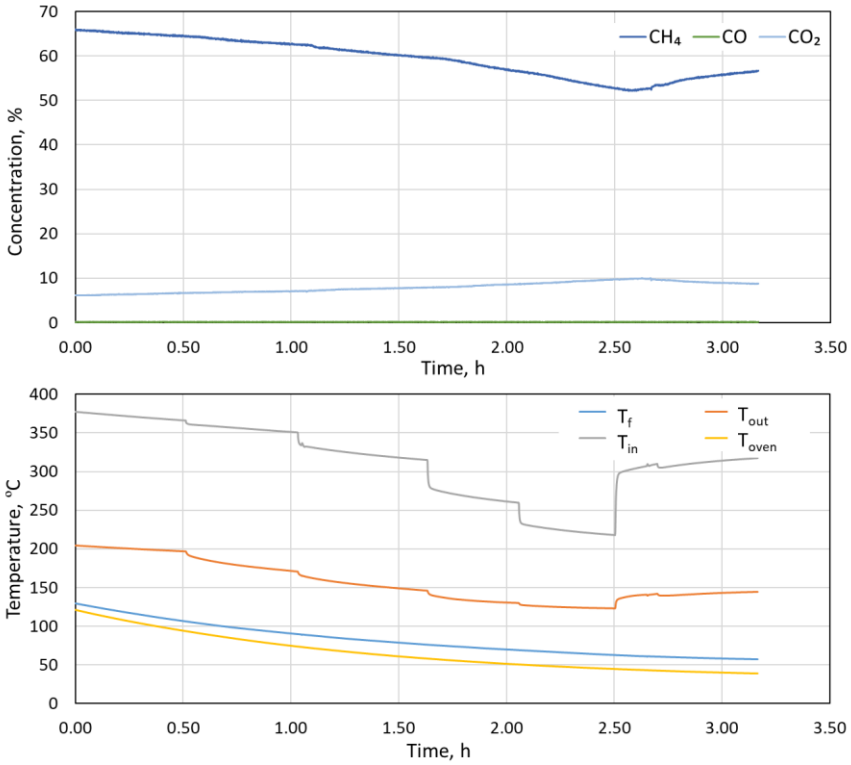

Fig. S12. The change of mole fraction and temperature with time (Reactor 2 performance as a function of coolant flow rate). *Parameters:* T_f = 20 °C, H_2:CO_2 = 4, P = 3 bar, GHSV = 8,000 L/(kg h), pure CO_2 feed.

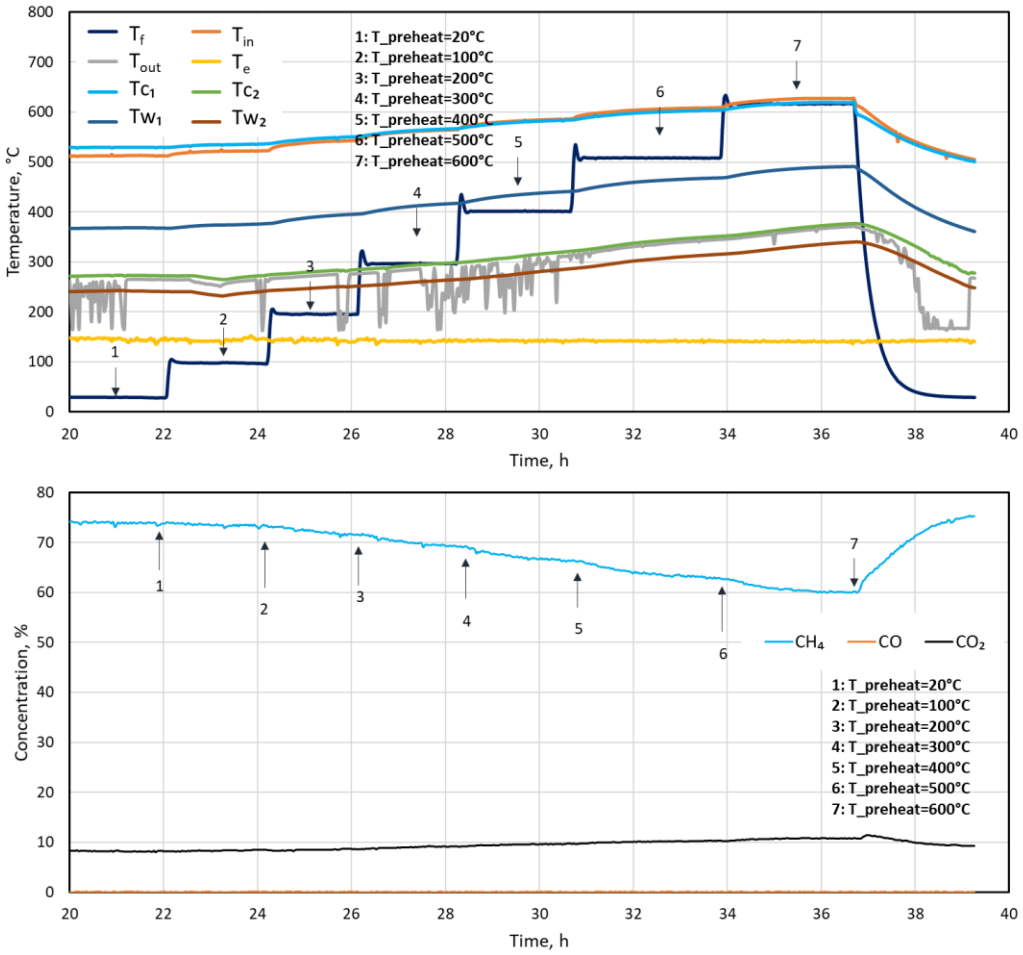

Fig. S13. The change of mole fraction and temperature with time (Reactor 3 performance as a function of feed temperature). *Parameters*: P = 11 bar, H_2:CO_2 = 4, Q_c = 0.8 L/min (cocurrent flow), GHSV = 2,000 L/(kg h), pure CO_2 feed.

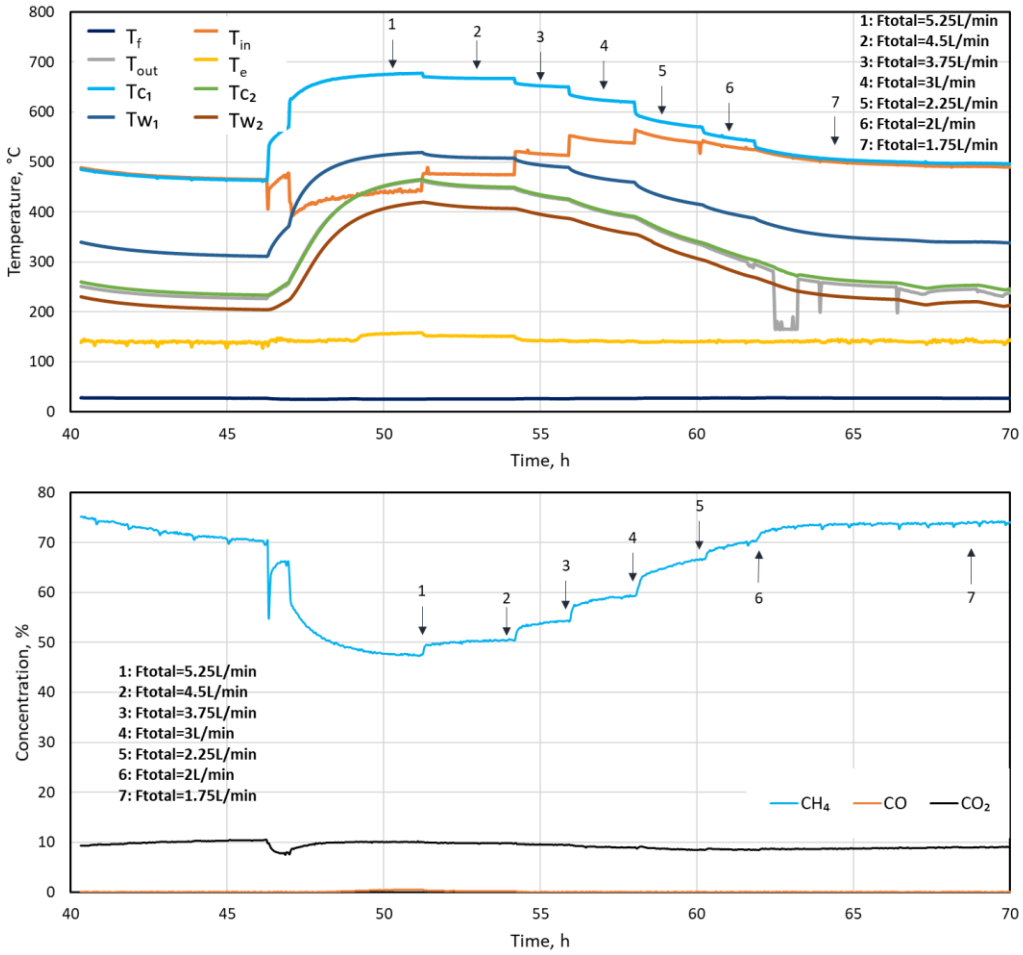

Fig. S14. The change of mole fraction and temperature with time (Reactor 3 performance as a function of GHSV). *Parameters*: P = 11 bar, H_2:CO_2 = 4, Q_c = 0.8 L/min (cocurrent flow), no feed preheating, pure CO_2 feed.

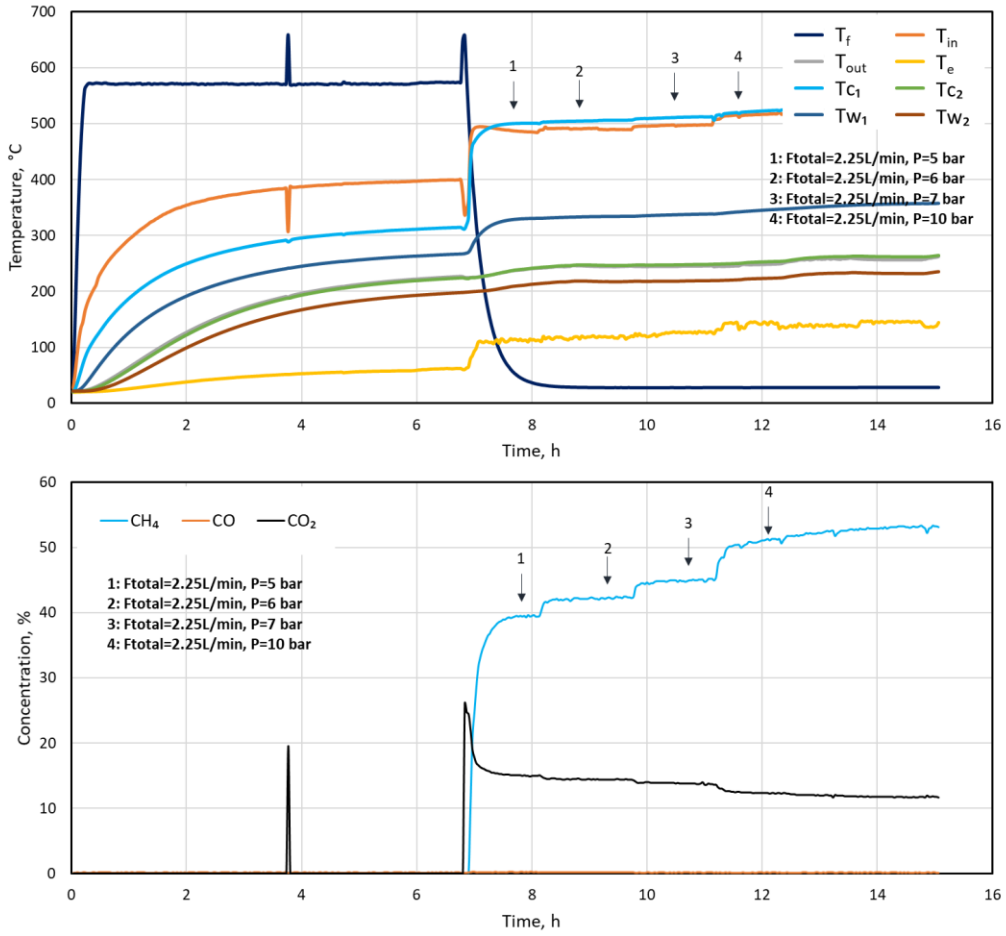

Fig. S15. The change of mole fraction and temperature with time (Reactor 3 performance as a function of P). *Parameters*: H_2:CO_2 = 4, Q_c = 0 L/min, no feed preheating, GHSV=2,100 L/(kg h) , pure CO_2 feed.

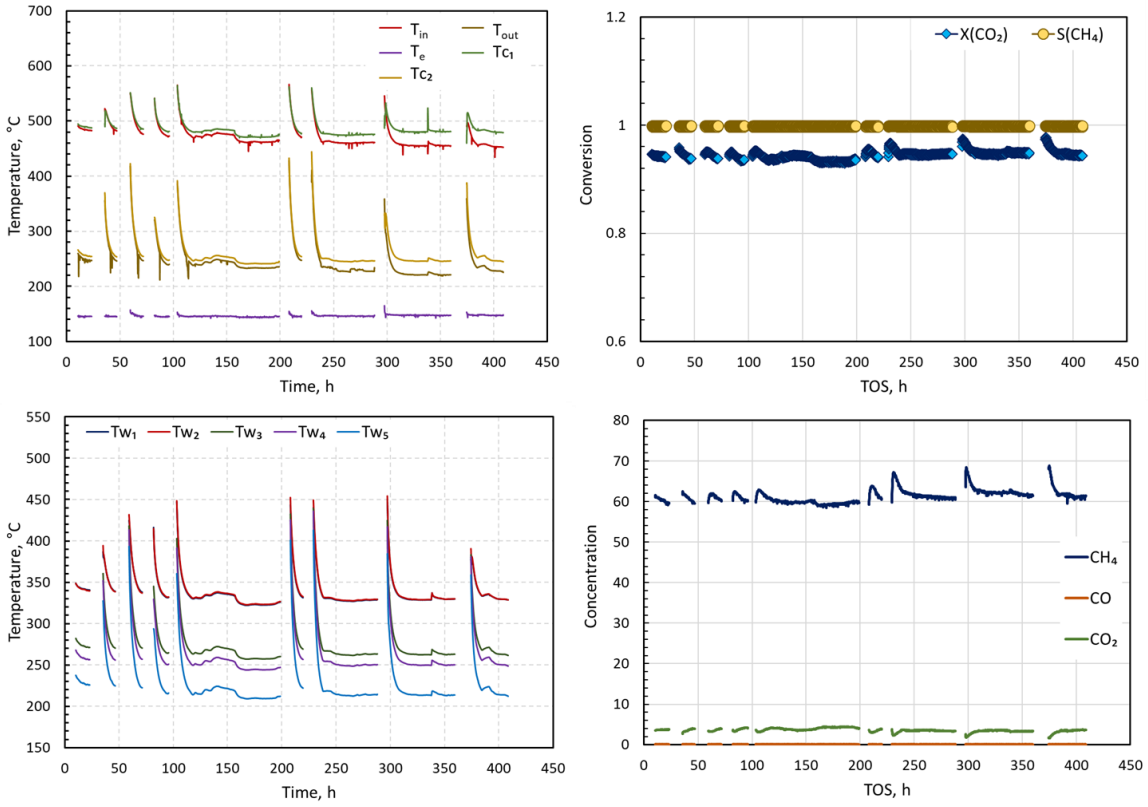

Fig. S16. Long-term stability of Reactor 3 at low GHSV (done overnights to keep reactor operating over multiple periods). *Parameters:* P=11 bars, GHSV= 1,600 L/(kg h), Coolant flow rate= 0 L/min, H_2:CO_2=4, no preheat, pure CO_2 feed.

Appendix F

Additional experimental results in Chapter 4 (direct biogas upgrade)

Additional experimental results in Chapter 4 (direct biogas upgrade) are shown here:

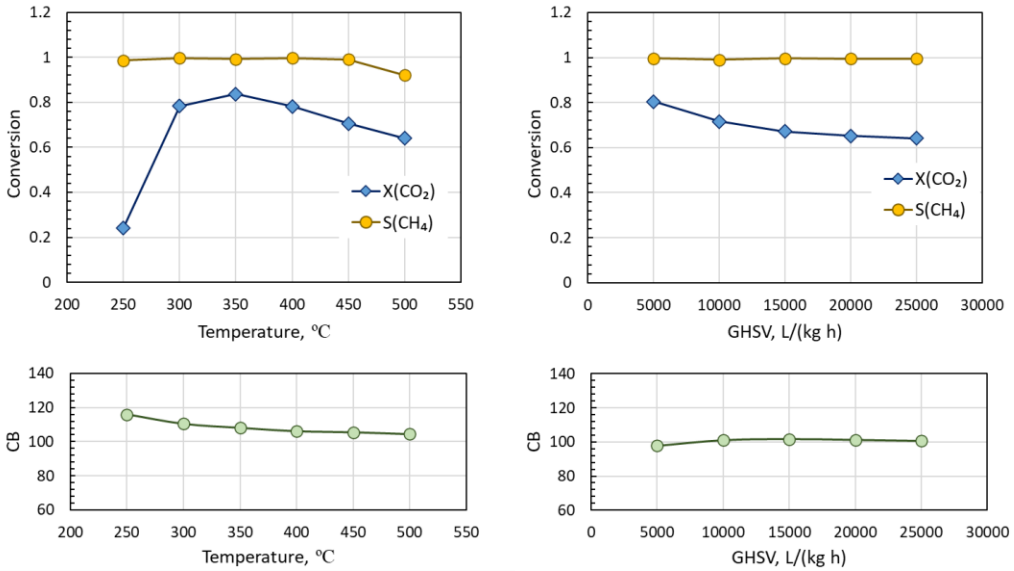

Fig. S17. CO_2 conversion and CH_4 selectivity as a function of temperature and GHSV showing corresponding carbon balance (raw biogas feed). *Parameters:* H_2:CO_2=4, P= 1 bar, GHSV=3,100 L/(kg h) (Temperature test), T=350°C (GHSV test).

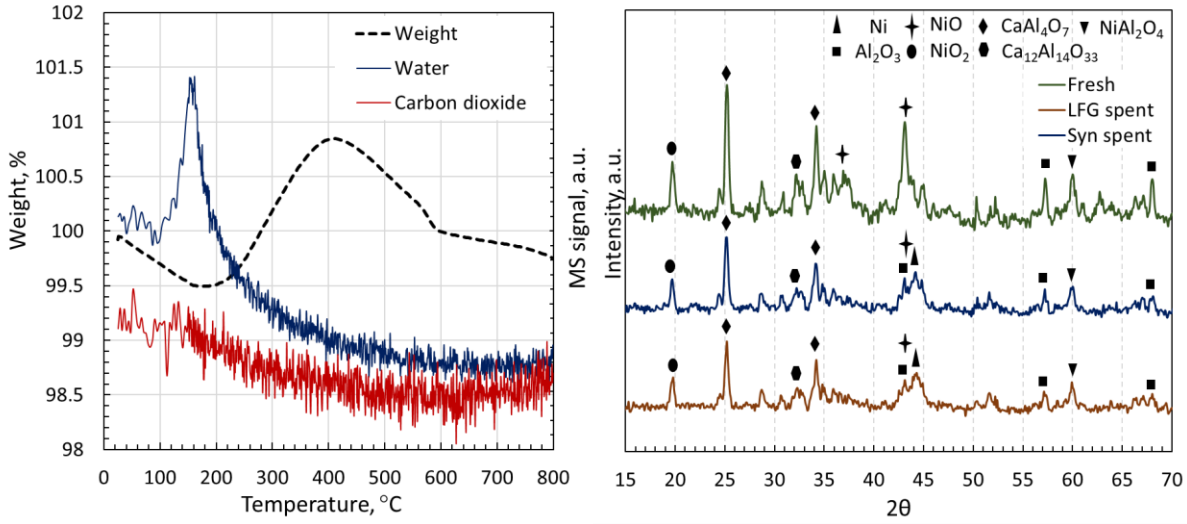

Fig. S18. TGA-MS and XRD results of spent commercial Ni/Al_2O_3 catalyst after ~30 h on stream.

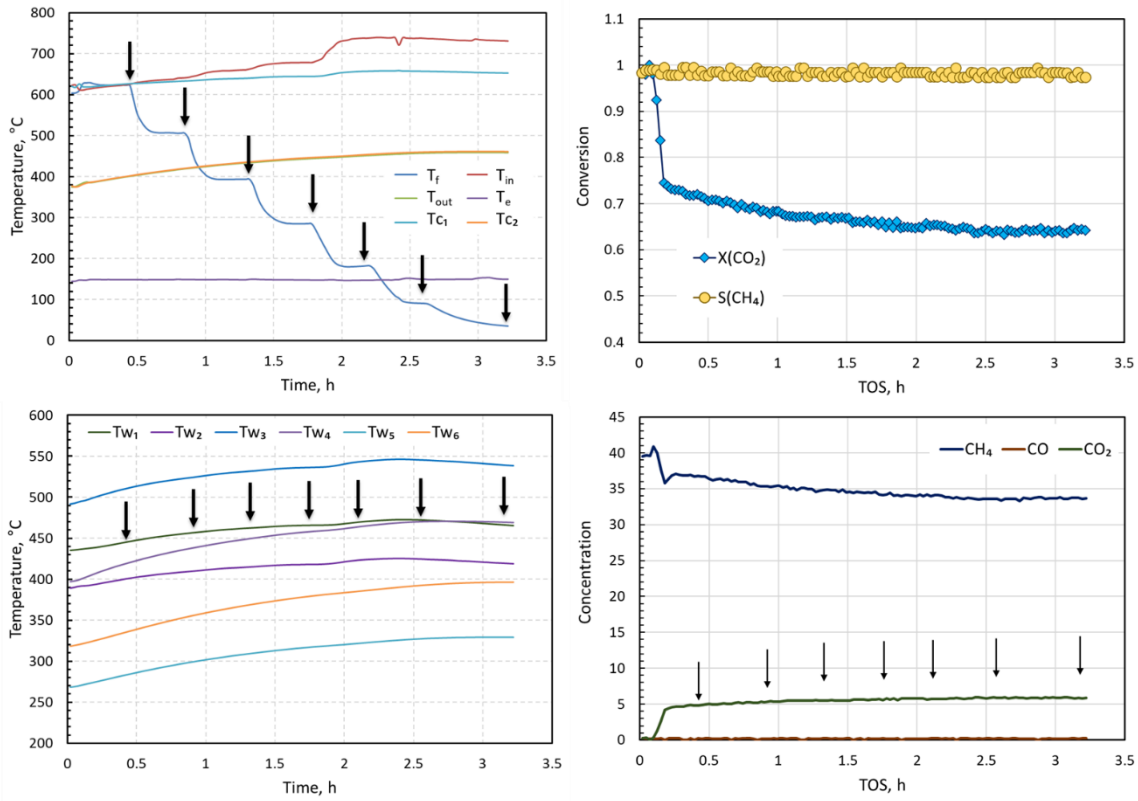

Fig. S19. The change of mole fraction and temperature with time (Reactor 3 performance as a function of feed temperature). *Parameters:* P=11 bars, GHSV= 3100 L/(kg h), Coolant flow rate= 0 L/min, H_2:CO_2=4, CH_4:CO_2=1.43, preheat temperature=20-600°C, air balance LFG feed.

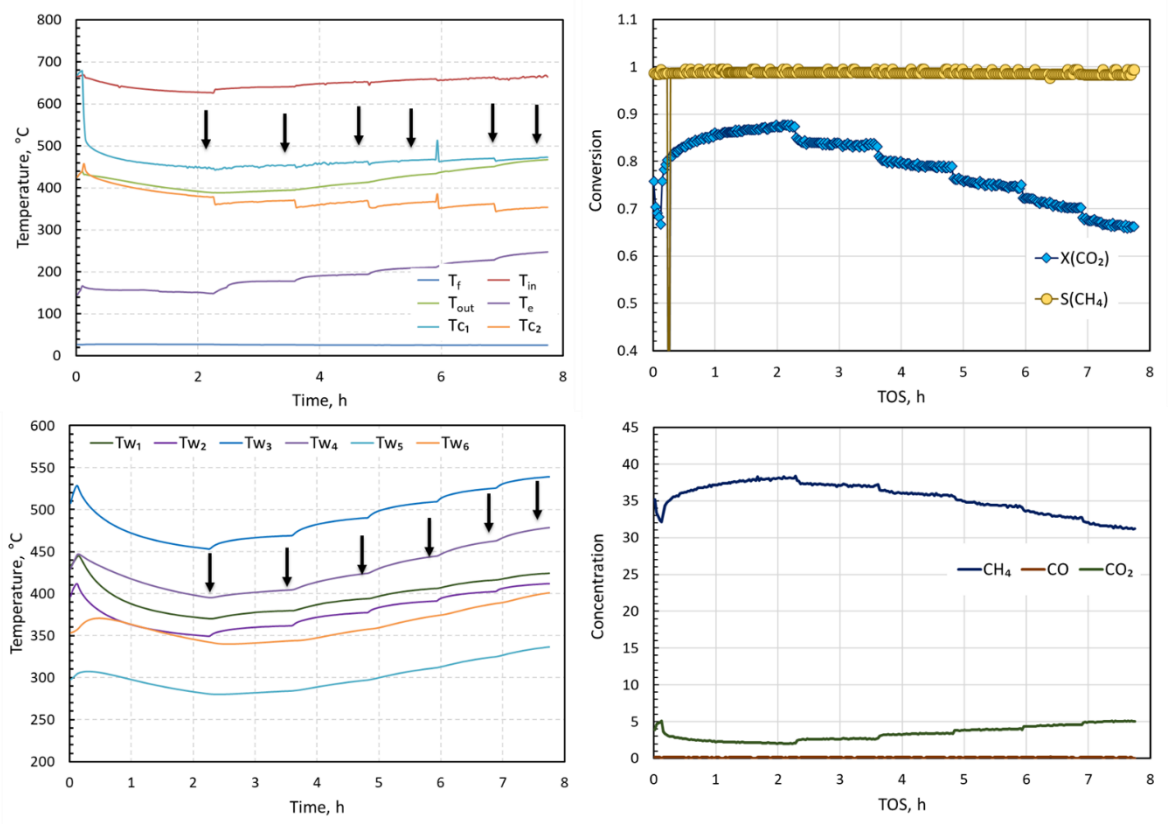

Fig. S20. The change of mole fraction and temperature with time (Reactor 3 performance as a function of GHSV). *Parameters:* P=7 bars, Coolant flow rate= 3-6 L/min (Cocurrent), H_2:CO_2=4.38, CH_4:CO_2=1.43, no preheat, air balance biogas feed.

Table. S1. MicroGC measurements of the above test (Reactor 3 performance as a function of GHSV, air balance biogas feed).

GHSV	H_2, %	O_2, %	N_2, %	CH_4, %	CO_2, %
3099	16.51	0.03	35.37	36.19	4.64
3763	17.68	0.03	35.02	34.97	5.58
4427	21.88	0.03	34.36	33.61	6.59
5091	26.43	0.03	33.62	32.16	7.54
5756	31.78	0.03	32.73	31.99	8.46
6420	36.70	0.03	32.09	31.86	9.08

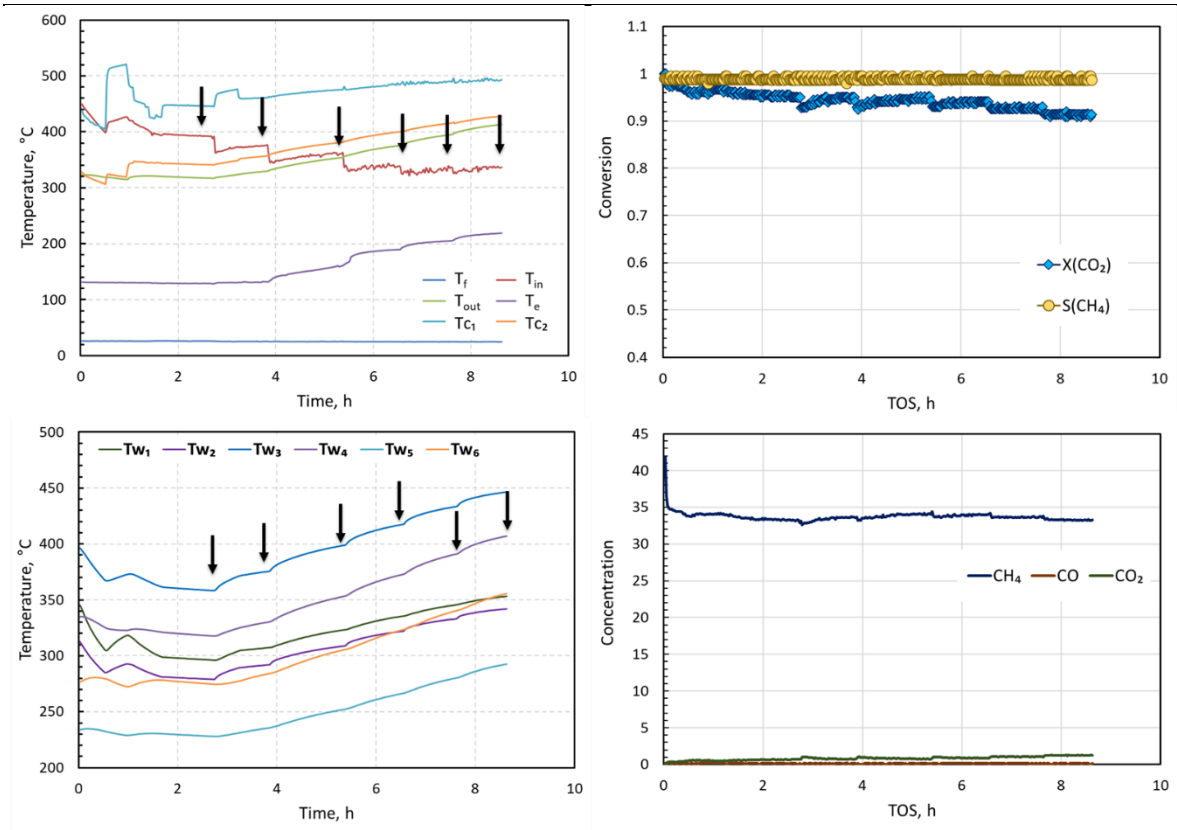

Fig. S21. The change of mole fraction and temperature with time (Reactor 3 performance as a function of coolant flow rate). *Parameters:* P=7 bars, Coolant flow rate= 1-3 L/min (Cocurrent), H_2:CO_2=4.38, CH_4:CO_2=1.43, no preheat, nitrogen balance biogas feed.

Table. S2. MicroGC measurements of the above test (Reactor 3 performance as a function of GHSV, nitrogen balance biogas feed).

GHSV	H_2, %	N_2, %	CH_4, %	CO_2, %
3099	29.06	37.28	32.16	2.25
3763	26.85	38.01	32.77	2.37
4427	23.67	38.52	33.31	2.41
5091	23.77	38.59	32.02	2.54
5756	24.24	38.42	31.71	2.91
6420	25.16	38.16	31.37	3.32

Appendix G

Mass and heat transfer criteria

The absence of interphase, Eq. (S8, S9), and intraparticle, Eq. (S10, S11), mass and heat transfer limitations were confirmed by calculating corresponding criteria [92, 93] (all symbols are listed in *Nomenclature*):

$$\frac{R'_{obs}\rho_b r_p}{k_c C_{CO_2,b}} \ll 0.15 \quad \text{(S8)}$$

$$\frac{\left|\Delta H_{SR}\right| R'_{obs}\rho_b r_p E_a}{hT^2 R_g} \ll 0.15 \quad \text{(S9)}$$

$$\frac{R'_{obs}\rho_g r_p^2}{D_m C_{CO_2,s}} \ll 1 \quad \text{(S10)}$$

$$\frac{\left|\Delta H_{SR}\right| R'_{obs}\rho_b r_p^2 E_a}{\lambda_s T^2 R_g} \ll 1 \quad \text{(S11)}$$

Interphase mass and heat transfer coefficients (k_c and h) were calculated using the following correlations [94]:

$$\mathrm{Sh} = \frac{k_c d_p}{D_m} = 2 + 0.6\,\mathrm{Re}_p^{0.5}\,\mathrm{Sc}^{\frac{1}{3}} \quad \text{(S12)}$$

$$\mathrm{Nu} = \frac{h d_p}{\lambda_g} = 2 + 0.6\,\mathrm{Re}_p^{0.5}\,\mathrm{Pr}^{\frac{1}{3}} \quad \text{(S13)}$$

Dimensionless numbers:

$$\mathrm{Re}_p = \frac{v_g \rho_g d_p}{\mu_g}, \mathrm{Sc} = \frac{\mu_g}{\rho_g D_m}, \mathrm{Pr} = \frac{\mu_g C_{pg}}{\lambda_g} \quad \text{(S14)}$$

Calculations were conducted for low and high conversions (16-86% range) in the 325-450 °C temperature range, 1-3 bar pressure range, 1000-60000 L/(kg h) space velocity range and 275-425 µm pellet size. Constant parameters and variables are listed in Tables S3 and S4.

Table. S3. Constant parameters [95].

Parameters	Unit	Value
ε		0.5
ΔH_{SR}	kJ/mol	164.9
ρ_b	kg/m^3	1925
ρ_g	kg/m^3	0.42
E_a	kJ/mol	74

Table. S4. List of variables.

Variable	Unit	Min	Max
X_{CO2}		0.16	0.86
T	°C	325	450
P	Bar	1	3
v_g	m/s	0.0021	0.14
λ_g	kJ/(m s k)	2.80E-4	3.32E-4
d_p	µm	275	425
λ_s	kJ/(m s k)	2.51	2.51
C_{pg}	kJ/(mol k)	3.33E-2	3.41E-2
μ_g	kg/(m s)	1.96E-5	2.26E-5

In all cases, all transport limitations were completely negligible, which is as expected for the small size of catalyst pellets (275-425 μm) used in the experiments. The calculated ranges are shown in Table S5.

Table. S5. Calculated minimum and maximum values for the transport limitation criteria.

Criterion type	Min	Max	Criterion
Mears criterion for interphase mass transfer	5.47E-6	8.14E-3	<< 0.15
Mears criterion for interphase heat transfer	2.88E-4	5.74E-2	<< 0.15
Weisz-Prater criterion for internal diffusion	1.12E-5	2.04E-2	<< 1
Isothermal pellet criterion	1.18E-7	1.87E-5	<< 1

Appendix H

Transport coefficients in COMSOL model

The effective axial and radial heat conductivity in the packed bed can be described by the following correlations [96]:

$$k_{ae} = \lambda_g (4 + \frac{\mathrm{Re}\,\mathrm{Pr}}{2}) \tag{S15}$$

$$k_{re} = \lambda_g (4 + \frac{\mathrm{Re}\,\mathrm{Pr}}{7[2-(1-2d_p / d_R)^2]}) \tag{S16}$$

The effective axial and the radial dispersion coefficients were calculated using a typical correlation adopted from literature [97]. Diffusion coefficient D_0 for H_2-CO_2 pair at standard temperature and pressure is 5.5E-4 [98].

$$D_e = \varepsilon \left(\frac{D_m}{\tau_{bed}} + m d_p v_g \right) \tag{S17}$$

$$D_m = D_0 \left(\frac{T}{T_0} \right)^{1.75} \frac{P_0}{P} \tag{S18}$$

For radial and axial dispersion m is set to 0.1 and 0.5 respectively. The correlation between the bed porosity and the bed tortuosity is

$$\tau_{bed} = \frac{1}{\sqrt{\varepsilon_{bed}}} \tag{S19}$$

Wall heat transfer coefficients for heat exchange between the Sabatier compartment and cooling compartment, Eq. (S20), and heat loss to the environment, Eq. (S21), were calculated by resistances in series. These parameters account for the contribution of the effective wall

heat transfer coefficient for each compartment (h_w), wall thermal conductivity (λ_w), insulation layer (λ_{ins}) and natural convection from the external reactor surface (h_{nc}).

$$U_{w,HE} = \left(\frac{1}{h_w^{SR}} + \frac{d_w^c}{\lambda_w^c} + \frac{1}{h_w^c} \right)^{-1} \quad \text{(S20)}$$

$$U_{w,HL} = \left(\frac{1}{h_w^{SR}} + \frac{d_w^{SR}}{\lambda_w^{SR}} + \frac{d_{ins}}{\lambda_{ins}} + \frac{1}{h_{nc}} \right)^{-1} \quad \text{(S21)}$$

The values for the insulation layer (quartz wool) conductivity (λ_{ins}) and natural convection (h_{nc}) were adopted from the literature [99, 100]. These contributions were dominant in Eq. (S21) and the wall heat loss coefficient was nearly constant in all simulations. The correlations for heat capacity and viscosity are listed below [101, 102].

Heat capacity, kJ/(mol K)

$$C_{p,CO_2} = -2\times10^{-8}T^2 - 5\times10^{-5}T + 0.0256$$
$$C_{p,H_2} = 3\times10^{-9}T^2 - 2\times10^{-6}T + 0.0297$$
$$C_{p,CO} = 10^{-8}T^2 - 7\times10^{-6}T + 0.0301$$
$$C_{p,H_2O} = 10^{-8}T^2 - 5\times10^{-6}T + 0.0356$$
$$C_{p,CH_4} = 0.03\ln(T) - 0.1394$$
$$C_{p,s} = -2.796\times10^{4}T^2 + 1.742\times10^{-4}T + 1.0446$$

Viscosity, Pa s

$$\mu_{CO_2} = 4\times10^{-8}T + 6\times10^{-6}$$
$$\mu_{H_2O} = 4\times10^{-8}T - 3\times10^{-6}$$
$$\mu_{H_2} = 2\times10^{-8}T + 5\times10^{-6}$$
$$\mu_{CH_4} = 3\times10^{-8}T + 4\times10^{-6}$$
$$\mu_{CO} = 4\times10^{-8}T + 7\times10^{-6}$$